FACULTY OF SCIENCE AND TECHNOLOGY

MASTER'S THESIS

Study programme / specialisation: Marine and Offshore Technology	The (spring) semester, (2023) Open
Author: Sindre Fjermedal	
Supervisor: Prof. Muk Chen Ong Co-supervisor: Chern Fong Lee	
Thesis title: Mooring designs for a combined wind and wave energy system in intermediate water depth	
Credits (ECTS): 30	
Keywords: Wind energy, Wave energy, Floating offshore wind, Mooring system, Synthetic fibre ropes, Intermediate water	Pages: 130 + appendix: 0 Stavanger, (15.06.2023)

Abstract

Over the past few decades, the renewable energy industry has expanded offshore in response to the growing demand for clean and sustainable energy. Larger structures with greater power output and less visual disturbance from shore are some of the reasons that motivate the development. Floating energy systems such as offshore wind turbines and wave energy converters (WECs) offer significant potential for producing clean, sustainable energy. The levelized cost of energy from wind and wave energy can potentially be reduced by developing combined wind and wave energy systems which allows for the co-sharing of infrastructure such as mooring systems, supporting platforms and power cables.

In the present study, different mooring systems of a combined wind and wave energy system – the semi-submersible torus flap combination (STFC) concept, deployed in intermediate water depths are developed. STFC consists of a torus WEC, three flap type WECs and a 5 MW NREL reference wind turbine. Fully coupled time-domain analysis of STFC under aligned wind and wave conditions has been performed using SIMA, a software for the analysis of marine operations. The tension-stretch relationship of polyester ropes is modelled using the Syrope model. Six environmental conditions at 50 m water depth representing operational conditions of STFC have been simulated.

The findings of this study have led to the production of two papers focusing on the mooring systems of STFC. The first paper compares catenary and taut mooring systems against a hybrid system consisting of chains, polyester ropes and a buoy. The results are presented in terms of system restoring forces, system natural periods, motion responses, mooring line tensions responses and the cost of mooring. Lastly, a design recommendation for the mooring system of STFC is given. The second paper focuses on a parametric study of the anchor radius of a polyester-based taut mooring system in order to reduce the mooring footprint and cost. The system restoring stiffness is kept constant while anchor spacing, mooring line length, cross-sectional area and minimum breaking load are proportionally reduced. Results are presented in terms of motion responses and mooring line tension responses.

In the first paper, the deployment of a hybrid mooring system is seen to decrease the non-linearity of tension responses, mooring stiffness, and the cost of mooring when compared to

catenary and taut mooring systems. No slack line, vertical load on the anchor or contact between the polyester ropes and seabed is observed. Hybrid mooring systems offer solutions with the lowest cost as the combination of polyester ropes and drag-embedment anchors significantly reduce cost. In the second paper, a reduction in anchor radius while maintaining similar surge and sway restoring stiffnesses is seen to reduce pre-tension. Consequently, the yaw stiffness reduces, and a longer yaw natural period is observed between the largest and smallest anchor radius. The maximum tension increases with decreasing anchor radius due to increased surge resonant response. No event of slack line is observed. The minimum tension decreases at an increasing rate as the anchor radius decreases, suggesting that a further proportional reduction of the anchor radius would result in a slack line.

Acknowledgements

I want to start by expressing my most gratitude to Professor Muk Chen Ong. He is obsessed with perfection and wants the best for his students. He has a mindset towards work which is worth adopting. I thank him for all his guidance and the opportunity to work with him.

My co-supervisor, Chern Fong Lee, is the person I have worked closely with for the last year. I appreciate his guidance and knowledge of topics related to my thesis. Working with him has been a pleasure.

I would also like to thank all my fellow Marine and Offshore technology students. An extra acknowledgement goes to students of C-189. Thanks for all memories we have shared. These will live on with me forever.

Finally, I would like to express love for my family and especially my wife. Words cannot describe her patience, support and guidance throughout my studies. I look forward to spending all my time with her and our daughter.

List of publications

This thesis is written as a set of two papers currently being reviewed. The papers are listed as follows:

1. Fjermedal, S., Lee, C.F., Ong, M.C, 2023, "Design and comparative analysis of mooring systems for a combined wind and wave energy system in intermediate water depth"
2. Lee, C.F., Fjermedal, S., Ong, M.C, 2023, "Design and analysis of taut mooring systems for a floating offshore wind and wave energy system"

Regarding the authorship and contributions in these papers, I am the first author of Paper 1 and responsible for performing the numerical simulations, providing the results and discussions, and writing the paper under the supervision of Prof. Muk Chen Ong and Chern Fong Lee. Chern Fong Lee is the second author and provided me with a model of STFC.

As for Paper 2, I am the second author, responsible for conceptualisation, numerical simulations, providing results and commenting on the paper. First author Chern Fong Lee initiated the study and wrote the paper.

Table of contents

List of Figures

List of Tables

Abbreviations

BEM	Blade element momentum
CoG	Centre of gravity
DOF	Degree of freedom
DEA	Drag-embedment anchor
EC	Environmental condition
FOWT	Floating offshore wind turbine
LCOE	Levelized cost of energy
LF	Low frequency
MSWL	Mean seawater level
MBL	Minimum breaking load
OWC	Oscillating water column
PI	Proportional integral
PTO	Power take-off
QTF	Quadratic transfer function
SA	Suction anchor
STFC	Semi-submersible torus flap combination
TDP	Touch-down point
TLP	Tension leg platform
WEC	Wave energy converter
WF	Wave frequency

Chapter 1 - Introduction

1.1 Background

The European Union (EU) has set an ambitious goal of at least 300 GW offshore wind and 40 GW ocean energy capacity by 2050. Ocean energy primarily concerns wave energy (EC-DG ENER, 2020a). The cumulative offshore wind capacity in the EU is 25.5 GW (Costanzo et al., 2023). Conversely, the cumulative wave energy capacity is a negligible 8 MW (EC-DG ENER, 2020b). Therefore, it is clear that in order to reach this goal, an enormous leap in offshore wind and wave installations is required.

Offshore wind has seen exponential growth when considering the first farm in 1991 had a capacity of 5 MW (Ørsted, 2019) and the upcoming Chaozhou farm in 2025 plans for 43.3 GW (IEEFA, 2022). In comparison, wave energy remains underdeveloped, although the power density of waves is 10 times higher than wind (Wimalaratna et al., 2022). While floating offshore wind turbines (FOWTs) have converged into designs with similar output, there is no apparent convergence of wave energy converter (WEC) designs. Considering that the first WEC was introduced in 1799, one would expect a convergence of design (Ross, 1995). However, that is not the case. There are numerous reasons, such as loss of energy in transmission, fatigue due to waves and corrosion and extreme wave loads.

Water depth is a deciding factor for whether offshore wind turbine structures are bottom-fixed or floating. Water depth can be described as shallow (0-30 m), intermediate (30-60 m) or deep (< 60 m) (Musial & Ram, 2010). The offshore wind industry has seen an industry moving from shallow to deep water and from bottom-fixed to floating structures. Shallow water sites and bottom-fixed structures are preferred over deep water and floating structures due to cost and accessibility. However, there are often conflicting interests at shallow than deep water sites, such as shipping lanes and fisheries. Additionally, some countries only have intermediate or deep water access, making FOWTs the only choice. The levelized cost of energy (LCOE) from bottom-fixed and floating wind turbines was in 2020 estimated to be 80 €/MWh and 135 €/MWh, respectively. However, the gap in LCOE is estimated to close by 2050 (DNV, 2021).

Common offshore wind structures at shallow (monopile), intermediate (jacket) and deep water (tension leg platform (TLP), semi-submersible and spar) are shown in Figure 1.1.

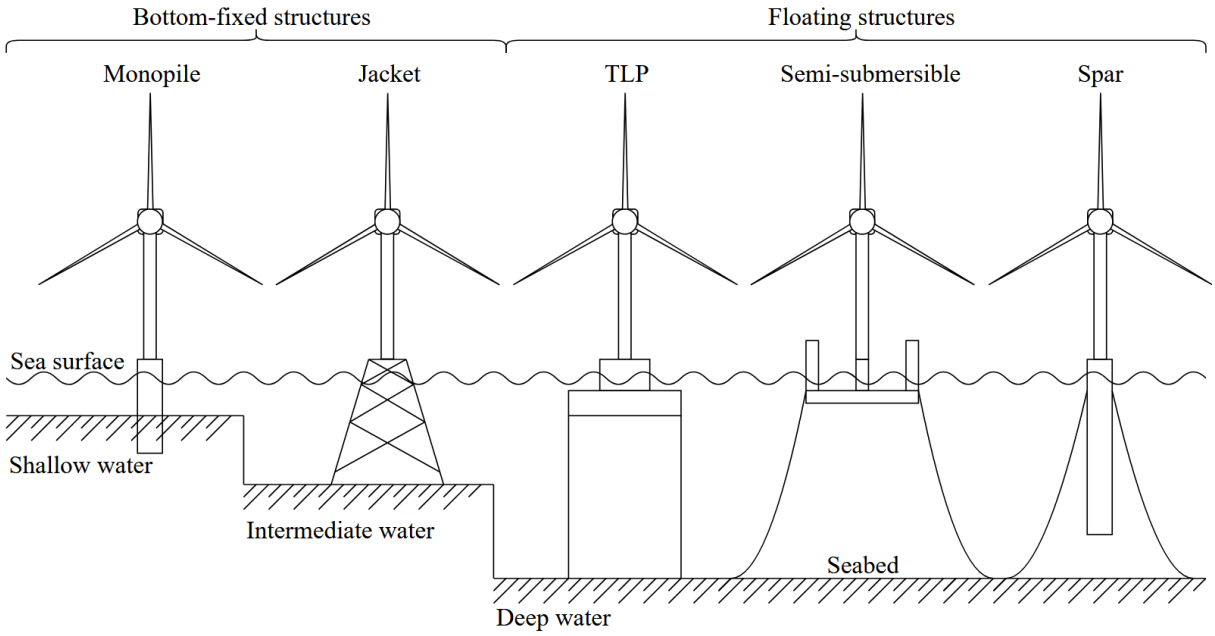

Figure 1.1: Common offshore wind turbine structures at different water depths

The most common WEC technologies are the oscillating water column (OWC), overtopping and wave absorber (Wang et al., 2018). Illustrations of an OWC and overtopping WEC are shown in Figure 1.2, and a wave absorber is shown in Figure 1.3. The OWC works by having a closed chamber in which waves can oscillate to compress air, which drives a turbine to generate power. Overtopping WEC works by having waves spill into a reservoir at a height h above the mean seawater level (MSWL). As a result, the water in the reservoir has potential energy and can be used to drive a hydro turbine to generate power. Wave absorbers generate power by converting kinetic energy from 1 to 6 degrees of freedom (DOF) motions of the wave absorber due to incoming waves. The dependence on motion can increase the output of wave absorbers by tuning the natural frequency to match the wave frequencies causing resonant responses. The tuning is easily done in regular waves as the wave profile can be predicted ahead of time. However, this tuning is increasingly difficult in the more common irregular seas where the wave profile is random (Drew et al., 2009).

The efficiencies of OWC, overtopping and wave absorber vary between 2 – 71 %, 3 – 27 % and 3 -79 %, respectively (Aderinto & Li, 2019). The variation in efficiencies is attributed to the power take-off (PTO). An efficient PTO is generally complex and sensible to the harsh environment. Hence, the design of a WEC is a balance between the efficiency and lifetime of the structure. The LCOE from WECs in 2020 was estimated to be 570 $/kWh, significantly higher than LCOE from other comparable renewable energy sources (Baca et al., 2022).

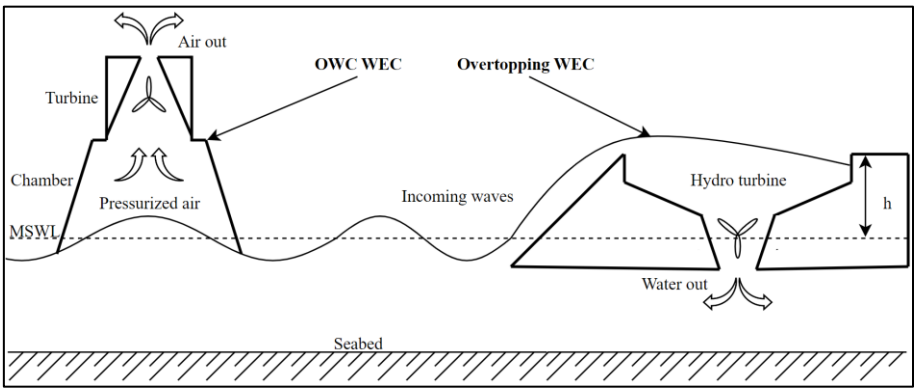

Figure 1.2: Illustration of an OWC and overtopping WEC

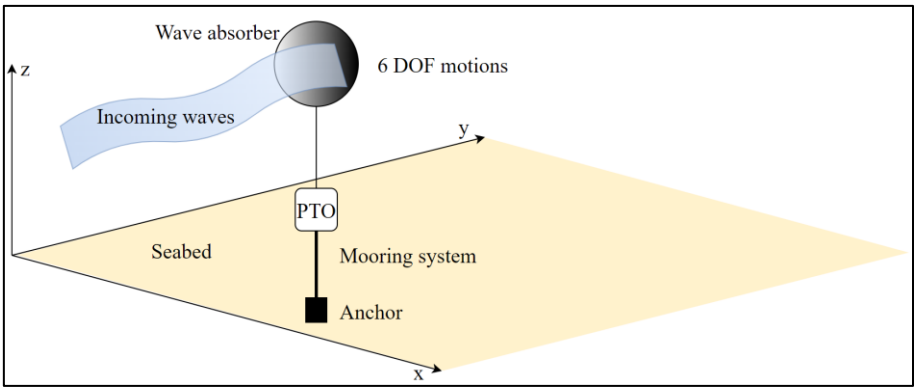

Figure 1.3: Illustration of a 6 DOF wave absorber WEC

Combined wind and wave energy systems are emerging as promising solutions to reduce the LCOE from FOWTs and WECs. There are several reasons why wind and wave combined systems are promising. First, FOWTs and WECs benefit from the spatial correlation of wind

and waves. Therefore, the same sites used for FOWTs can be used for WECs. Second, the co-sharing of infrastructure can potentially reduce LCOE (Exceedence Ltd, 2022). Third, less ocean space is required, which can be used for other activities or install more combined wind and wave energy systems.

There are several combined wind and wave energy systems in development. The most common method is large floaters, which can host multiple wind turbines and WECs. Wave absorbers WECs are commonly deployed in combined wind and wave energy systems due to their simplicity and require minimal space. The developing concept by FlexiFloat (2021) shown in Figure 1.4 is significantly larger than other combined wind and wave energy systems, covering an area of 420x240 m. With 9 wind turbines with a capacity of 42 MW and 48 WECs with a capacity of 30 MW, the total capacity of FlexiFloat is 72 MW. Additionally, FlexiFloat offers the option to install solar panels, further increasing the total capacity.

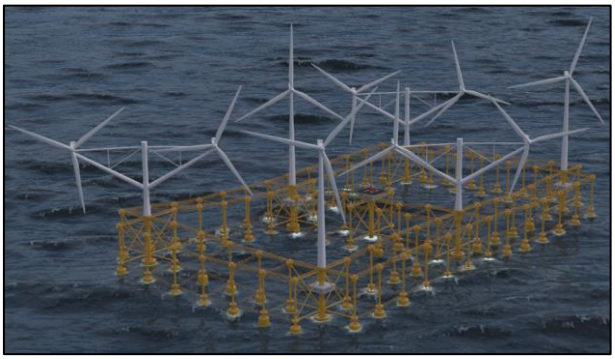

Figure 1.4: Illustration of FlexiFloat (FlexiFloat, 2021)

Smaller combined wind and wave energy systems are Poseidon 37, W2Power and FPP platform shown in Figure 1.5. Poseidon 37 is a 37 m wide barge which consists of three 11 kW wind turbines and 10 3 kW WECs, in total 63 kW capacity. The capacity is relatively low, but the concept has been proven and up-scaling to an 80 m barge with larger wind turbines and WECs is undergoing (McTiernan et al., 2020). W2Power consists of two 3.6 MW wind turbines and 2.8 MW from WECs (McTiernan et al., 2020). The FPP platform consists of one 2.3 – 8 MW wind turbine and 4 WECs with a 450 – 650 kW capacity (Heras, 2019). The FPP is unique as

development is ongoing to store clean energy within the hull as hydrogen. Hence, it acts as a battery and can provide continuous power without wind and waves (FPP, 2023). Another combined wind and wave energy system is the semi-submersible torus flap combination (STFC) concept by Lee et al. (2022), shown in Figure 1.6. The concept comprises a 5 MW wind turbine, one torus WEC and three flap type WEC. Research has shown that STFC can achieve as much as a 129 % increase in power production due to the inclusion of WECs compared to a standalone 5 MW FOWT.

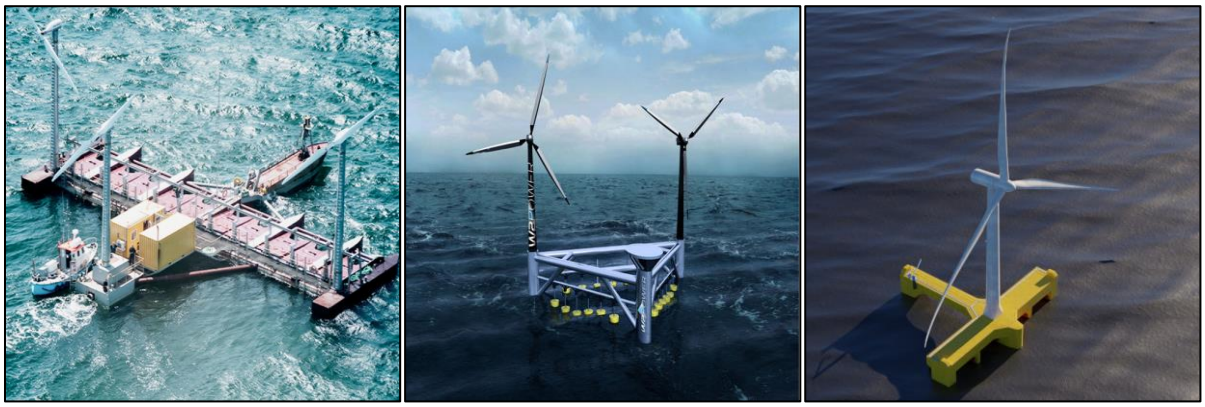

Figure 1.5: Poseidon 37 to the left, W2Power in the centre and FPP platform to the right (McTiernan et al., 2020; FPP, 2023)

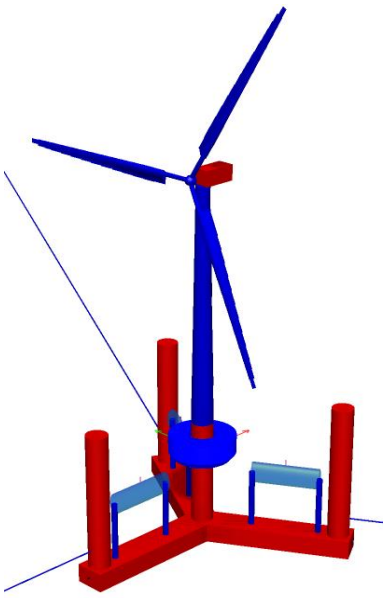

Figure 1.6: Visualisation of STFC

Station-keeping is a common requirement for all floating offshore renewable systems and may be achieved through dynamic position or mooring systems. However, floating offshore renewable systems are required to have a long lifetime and low maintenance, making passive mooring systems the best choice. Nevertheless, mooring systems contribute significantly to the overall cost. For example, the mooring system of a FOWT and WEC accounts for 40 % and 30 % of the overall cost, respectively (DNV, 2023; Martinelli et al., 2012).

Renewable floating energy structures have traditionally been installed in deep water using similar mooring systems as floating Oil and Gas structures. However, the requirements for the mooring system differ between the two industry sectors. Overly conservative and redundant designs are standard for Oil and Gas structures to protect humans and the environment should a mooring line break. Conversely, there is a lower risk to humans and the environment if a mooring line on a renewable floating energy structure break, as human interaction and chemical spills are limited. Hence, a less conservative and less redundant mooring system is more cost-effective.

The intermediate water is considered a "grey zone" whether to deploy bottom fixed or floating structures. The commonly used catenary mooring system relies heavily on water depth to achieve a sufficient catenary shape. The lack of catenary shape increases the non-linear tension responses and requires an overly conservative mooring system design. In response, mooring systems using lightweight materials such as polyester or nylon are being developed. While synthetic fibre ropes have been extensively used in the Oil and Gas industry since 1997 (Francois & Davies, 2000), it has not gained traction in the offshore renewable sector. Nevertheless, some existing projects use synthetic fibre ropes. The FOWT FloatGen demo has 6 nylon mooring lines (Choisnet et al., 2018). The CETO WEC has 3 synthetic fibre ropes as mooring lines (Weller et al., 2015).

Extensive research has been conducted to evaluate whether mooring systems for FOWTs using synthetic fibre ropes such as polyester or nylon can compete against catenary mooring systems. Synthetic fibre ropes offer excellent fatigue properties, are immune to corrosion, and reduce non-linear tension responses. The research has been conducted for shallow, intermediate and deep water. The concluding results regarding using polyester and nylon as mooring materials

for FOWTs are promising (Pham et al., 2019; Ramakrishnan, 2022; Stenlund, 2018; Sørum et al., 2023a; Sørum et al., 2023b; Tomren, 2022; Xu et al., 2021).

Several methods for modelling synthetic fibre ropes are in use today, such as the Syrope model (Falkenberg et al., 2017), the upper- and lower-bound model (API, 2014) and the bi-linear model (ABS, 2021). Due to different test and modelling procedures between the certification bodies, the results may vary (Falkenberg et al., 2018). Research has shown that the upper- and lower-bound model may yield conservative or non-conservative results, depending on which design parameter is considered (ABS, 2021). The bi-linear model may artificially reduce fatigue damage in the mooring line (Sørum et al., 2023a). The Syrope model is shown to accurately model the behavior of synthetic mooring lines (Sørum et al., 2023a; Sørum et al., 2023b).

1.2 Objectives and scope of work

In order to add to existing research, the objective of the present study is:

- Propose a mooring system based on synthetic fibre ropes for the combined wind and wave energy system STFC in intermediate water depth

The scope of work is defined as:

- Comprehensive literature review on the current state of the art for FOWT mooring system design, focusing on intermediate water depth deployment
- Define limit states of the floating wind and wave energy system and mooring system
- Outline time-domain analysis methods for catenary mooring system, taut mooring system and hybrid mooring system
- Perform time-domain analysis using SIMA
- Comparison of three concepts and discuss potential optimisation from the perspective of mooring system design
- Conclusions and recommendations for future work

1.3 Thesis outline

The thesis consists of two research papers originating from the objective. Both papers in full are included with sections regarding introduction, theory, numerical modelling, conclusions, and references. The thesis outline is as follows:

Chapter 1: An introduction section with the background and motivation for this research. The thesis objectives, scope of work and outline are given

Chapter 2: A brief description of mooring systems, configurations and components is given. Relevant theories, models and governing equations of mooring systems are established

Chapter 3: A brief description of environmental loads and structural responses on a moored STFC. Relevant theories, models and governing equations of environmental loads and structural responses are established

Chapter 4: A brief description of the numerical modelling procedures of STFC, environmental conditions and simulations.

Chapter 5: Presents the numerical simulation of mooring systems for STFC intermediate water depth. Several taut, catenary and hybrid mooring systems are modelled and evaluated in operational conditions under aligned wind and wave using two different pre-tensions. Results are presented regarding system restoring forces, system natural periods, motion responses, tension responses, and cost. Lastly, a design recommendation for the mooring system is given

Chapter 6: Presents the numerical simulation of a taut mooring system for a combined wind and wave energy system in intermediate water depth. Three taut mooring systems are modelled by keeping restoring stiffness constant in surge and sway by scaling anchor spacing, mooring line lengths, mooring line diameter and minimum breaking load proportionally. The taut mooring systems are evaluated in operational conditions under aligned wind and waves. Results regarding motion responses, tension responses, and cost are presented

Chapter 7: Conclusion and recommendations for future work

References

ABS. (2021) The Application of Fiber Rope for Offshore Mooring; ABS: Spring, TX, USA

API. (2014). API RP 2SM: Recommended Practice for Design, Manufacture, Installation, and Maintenance of Synthetic Fiber Ropes for Offshore Mooring. API, Washington, DC.

Aderinto, T., & Li, H. (2019). Review on power performance and efficiency of wave energy converters. Energies, 12(22), 4329.

Baca, E., Philip, R. T., Greene, D., & Battey, H. (2022). Expert Elicitation for Wave Energy LCOE Futures. National Renewable Energy Lab.(NREL), Golden, CO.

Choisnet, T., Rogier, E., Percher, Y., Courbois, A., Le Crom, I., & Mariani, R. (2018). Performance and mooring qualification in Floatgen: the first French offshore wind turbine project. 16ième Journées de l'Hydrodynamique, 1, 1-10.

Costanzo, G., Brindley, G., Cole, P., O'Sullivan, R., Miró, L. (2023). Wind energy in Europe 2022 Statistics and the outlook for 2023-2027. WindEurope. https://windeurope.org/intelligence-platform/product/wind-energy-in-europe-2022-statistics-and-the-outlook-for-2023-2027/#overview

DNV. (2021). Energy transition outlook 2021 – Technology progress report. https://www.dnv.com/Publications/technology-progress-report-211013

DNV. (2023). Floating wind: Turning ambition into action. https://www.dnv.com/focus-areas/floating-offshore-wind/floating-wind-turning-ambition-into-action.html

Drew, B., Plummer, A. R., & Sahinkaya, M. N. (2009). A review of wave energy converter technology. Proceedings of the Institution of Mechanical Engineers, Part A: Journal of Power and Energy. 2009;223(8):887-902.

EC-DG ENER (European Commission, Directorate-General for Energy). (2020a). An EU strategy to harness the potential of offshore renewable energy for a climate neutral future. Brussels, Belgium.

EC-DG ENER (European Commission, Directorate-General for Energy). (2020b). Clean Energy Transition – Technologies and Innovations. Brussels, Belgium.

Exceedence Ltd. (2022). LCOE Analysis for baseline project scenarios. European Scalable Offshore Renewable Energy Source (EU-Scores).

Falkenberg, E., Åhjem, V., & Yang, L. (2017). Best practice for analysis of Polyester rope mooring systems. Offshore Technology Conference, Houston, Texas, USA.

Falkenberg, E., Yang, L., & Åhjem, V. (2018). The Syrope Method for Stiffness Testing of Polyester Ropes. In Proceedings of the ASME 2018 37th International Conference on Ocean, Offshore and Arctic Engineering, Madrid, Spain, 17–22 June 2018 (Vol. 1, p. V001T01A067). New York, NY, USA: American Society of Mechanical Engineers.

FlexiFloat. (2021). Flexifloat – Flexible floating system. https://www.uis.no/nb/skaper-nye-losninger-havvind

FPP. (2023). Floating Power Plant: Poseidon and FPP Platform. https://www.floatingpowerplant.com/

Francois, M., & Davies, P. (2000). Fibre rope deep water mooring: a practical model for the analysis of polyester mooring systems. Rio Oil and Gas Expo and Conference, Rio de Janeiro, Brazil.

Heras, P. (2019). Control of Floating Power Plant: Model description. Floating Power Plant A/S & Aalborg University. September, 2019

IEEFA. (2022). Southern China city plans 43.3-gigawatt offshore wind project. https://ieefa.org/articles/southern-china-city-plans-433-gigawatt-offshore-wind-project

Lee, C. F., Tryfonidis, C., & Ong, M. C. (2022). Power performance and response analysis of a semi-submersible wind turbine combined with flap-type and torus wave energy converters. Journal of Offshore Mechanics and Arctic Engineering, 145(4), 042001.

Martinelli, L., Ruol, P., & Cortellazzo, G. (2012). On mooring design of wave energy converters: The Seabreath application. Coastal Engineering Proceedings, 1(33), structures.3.

McTiernan, K. L., & Sharman, K. T. (2020). Review of Hybrid Offshore Wind and Wave Energy Systems. In Journal of Physics: Conference Series (Vol. 1452, No. 1, p. 012016). IOP Publishing.

Musial, W., & Ram, B. (2010). Large-Scale Offshore Wind Power in the United States: Assessment of Opportunities and Barriers. National Renewable Energy Laboratory (NREL).

Pham, H. D., Cartraud, P., Schoefs, F., Soulard, T., & Berhault, C. (2019). Dynamic modeling of nylon mooring lines for a floating wind turbine. Applied Ocean Research, 87, 1-8.

Ramakrishnan, K. S. M. (2022). Numerical Analysis of Mooring Systems for Floating Wind Turbines (Master's thesis). Norwegian University of Science and Technology (NTNU).

Ross, D. (1995). Power from the Waves. Oxford University Press, USA. ISBN: 0-19-856511-9.

Stenlund, T. (2018). Mooring system design for a large floating wind turbine in shallow water (Master's thesis). Norwegian University of Science and Technology (NTNU).

Sørum, S. H., Fonseca, N., Kent, M., & Faria, R. P. (2023a). Modelling of Synthetic Fibre Rope Mooring for Floating Offshore Wind Turbines. Journal of Marine Science and Engineering, 11(1), 193.

Sørum, S. H., Fonseca, N., Kent, M., & Faria, R. P. (2023b). Assessment of nylon versus polyester ropes for mooring of floating wind turbines. Ocean Engineering, 278, 114339.

Tomren, M. (2022). Design and Numerical Analysis of Mooring Systems for Floating Wind Turbines – Comparison of Concepts for European Waters (Master's thesis). Norwegian University of Science and Technology (NTNU).

Wang, L., Isberg, J., & Tedeschi, E. (2018). Review of control strategies for wave energy conversion systems and their validation: the wave-to-wire approach. Renewable and Sustainable Energy Reviews, 81, 366-379.

Weller, S. D., Johanning, L., Davies, P., & Banfield, S. J. (2015). Synthetic mooring ropes for marine renewable energy applications. Renewable energy, 83, 1268-1278.

Wimalaratna, Y. P., Hassan, A., Afrouzi, H. N., Mehranzamir, K., Ahmed, J., Siddique, B. M., & Liew, S. C. (2022). Comprehensive review on the feasibility of developing wave energy as a renewable energy resource in Australia. Cleaner Energy Systems, 3, 100021.

Xu, K., Larsen, K., Shao, Y., Zhang, M., Gao, Z., & Moan, T. (2021). Design and comparative analysis of alternative mooring systems for floating wind turbines in shallow water with emphasis on ultimate limit state design. Ocean Engineering, 219, 108377.

Ørsted. (2019). Making green energy affordable: How the offshore wind energy industry matured – and what we can learn from it. https://orsted.com/en/insights/white-papers/making-green-energy-affordable/1991-to-2001-the-first-offshore-wind-farms

Chapter 2 - Station-keeping

The station-keeping system of a floating structure refers to the method used to keep the system within a pre-defined area. In this thesis, station keeping is limited to mooring systems. A mooring system is a combination of several components arranged in a specific configuration. The governing inputs of a mooring system design are floater characteristics (mass, dimensions, type), environmental conditions (water depth, wind, waves, current, soil) and operational requirements. Floater characteristics and operational requirements can be fixed for a project. The only varying input is ECs which may vary within an installation site spanning several square kilometres. There is no fit for all mooring systems, and the design procedure of a mooring system is an iterative process (Ma et al., 2019). An overview of relevant mooring system building blocks and a typical mooring design procedure are shown in Figure 2.1.

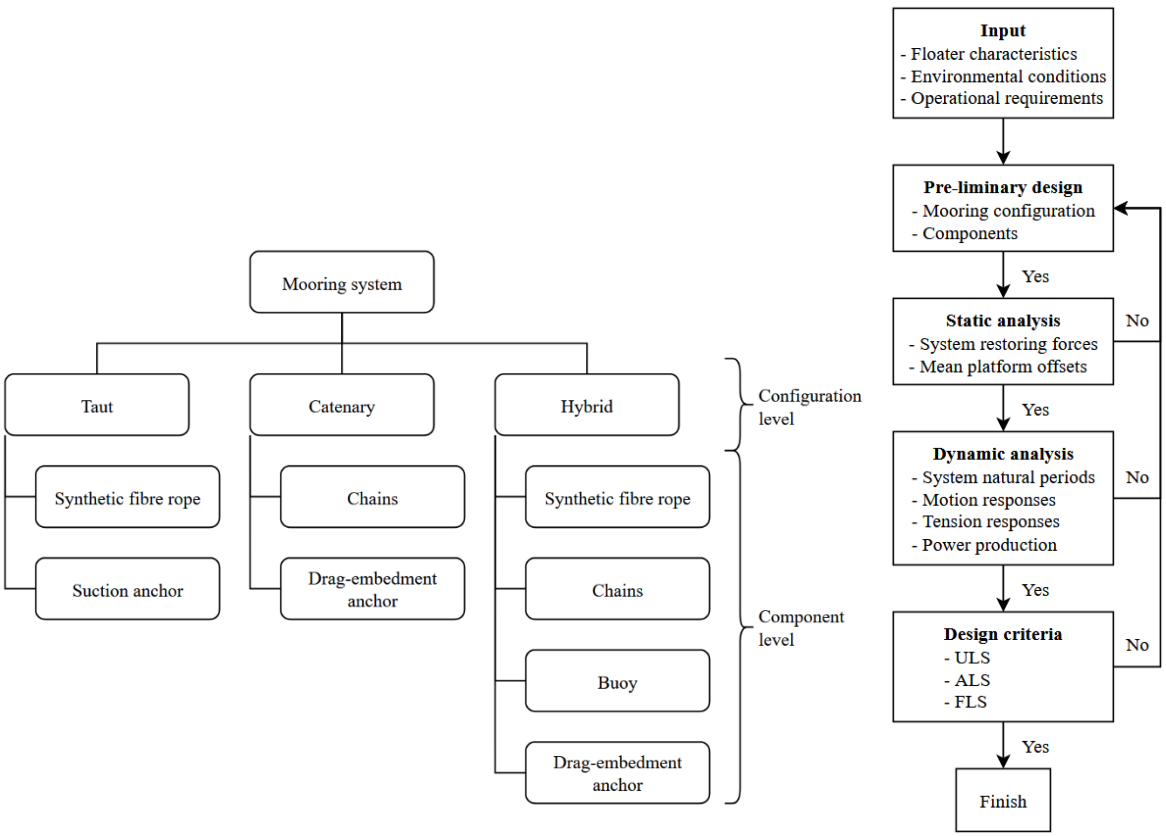

Figure 2.1: To the left, a mooring system shown at configuration and component level. To the right, a typical mooring design procedure

2.1 Mooring configurations

Mooring configuration refers to the geometric layout of the mooring systems, which influences how the restoring forces of the mooring system are generated. The most commonly employed mooring configurations are catenary, taut and hybrid, which will be described in the following sections.

2.1.1 Catenary mooring system

Catenary mooring systems are the most used mooring configuration for floating structures. The catenary mooring system generates a restoring force through the free-hanging weight of the mooring line. As the structure is displaced, the mooring line is lifted and the free-hanging weight increases. This effect, in combination with the decreased angle between the mooring line and the sea surface, generates a non-linear restoring force. These mooring systems are suitable for deep water sites. However, it is not suitable for shallow, intermediate and ultra-deepwater. In ultra-deepwater, the free-hanging weight is too high, causing high tension at the fairlead. In shallow and intermediate water, the issue is more complex. First, the reduction in water depth increases the system stiffness and the non-linearity of mooring line tension. Secondly, the catenary shape is reduced, and the anchor radius needs to be increased to compensate. Third, there is an increased risk of complete loss of catenary shape, which will induce vertical loadings on the anchor (Xu et al., 2021). The geometry of a catenary mooring line is shown in Figure 2.2. A catenary mooring line element is shown in Figure 2.3. The water depth is h, the length between the touch-down point (TDP) and fairlead is L, and s the mooring line length between fairlead and TDP. The vertical force component is V, the horizontal force component is H, and T is mooring line tension.

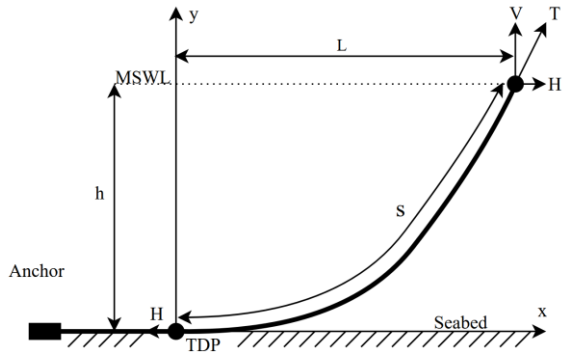

Figure 2.2: Catenary mooring system as seen in the x-y plane

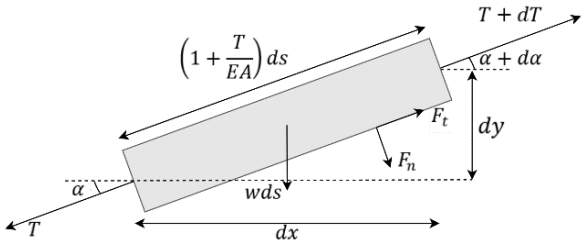

Figure 2.3: Forces on and dimensions of a catenary mooring line element. Reproduced according to Faltinsen (1993)

The hydrodynamic current forces in tangential and normal directions are F_t and F_n, respectively. The submerged weight per unit length is w, the cross-sectional area is A, and E is Young's modulus. The angle between the sea surface and the element is α. By analysing the element, the governing equations of a mooring line are

$$\begin{aligned} dT &= \left(wsin(\alpha) - F_t\left(1 + \frac{T}{EA}\right)\right) ds \\ Td\alpha &= \left(wcos(\alpha) + F_n\left(1 + \frac{T}{EA}\right)\right) ds \end{aligned} \tag{2.1}$$

There is no explicit solution to these equations. Nevertheless, a good approximation is to neglect the hydrodynamic current forces F_t and F_n. The elasticity EA can be neglected in operational conditions but should be accounted for in extreme conditions (Faltinsen, 1993). As a result, the governing equations simplify to

$$\begin{aligned} dT &= wsin(\alpha)ds \\ Td\alpha &= wcos(\alpha)ds \end{aligned} \tag{2.2}$$

Solving this set of equations in combination with appropriate boundary conditions yields the geometry of the catenary mooring line

$$\begin{aligned} y(x) &= \frac{H}{w}\left(cosh\left(\frac{w}{H}x\right) - 1\right) \\ s(x) &= \frac{H}{w}\frac{dy}{dx} = \frac{H}{w}sinh\left(\frac{w}{H}x\right) \end{aligned} \tag{2.3}$$

The force components are found to be

$$\begin{aligned} H &= \frac{w}{2h}(s^2 - h^2) \\ V &= ws \\ T &= \sqrt{H^2 + V^2} \end{aligned} \tag{2.4}$$

The horizontal distance between the fairlead and anchor, X, can be used to determine the horizontal force on the floater due to an offset x. The relationship between x-offset and horizontal force is

$$X = l - s + x = l - h\sqrt{1 + 2\frac{H}{wh}} + \frac{H}{w}\cosh^{-1}\left(1 + \frac{hw}{H}\right) \tag{2.5}$$

where l is the total mooring line length from fairlead to anchor.

The horizontal stiffness of a mooring line generally consists of two components, one geometric and one elastic component. The in-elastic horizontal geometric stiffness component is due to changes in mooring line geometry and can be found by solving Equation (2.5) for H and differentiating with respect to X

$$k_g = \frac{dH}{dX} = w\left[\frac{-2}{\left(1 + \frac{2H}{wh}\right)} + \cosh^{-1}\left(1 + \frac{wh}{H}\right)\right]^{-1} \tag{2.6}$$

The horizontal elastic stiffness component is due to the axial elongation of the mooring line and can be written as

$$k_e = \frac{EA}{l}\cos\alpha \tag{2.7}$$

A general mooring line interacts with top motion r and tension T and can be modelled as a spring-dashpot system with horizontal stiffness k_g, k_e and damping B due to hydrodynamic current forces, as shown in Figure 2.4.

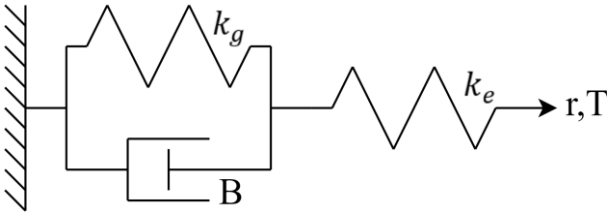

Figure 2.4: Spring-dashpot model of a general mooring line

An appropriate approximation is to neglect the hydrodynamic current forces (Faltinsen, 1993). Consequently, the total horizontal stiffness in a static condition can be modelled as two springs in series and thus be written as

$$\frac{1}{k_t} = \frac{1}{k_g} + \frac{1}{k_e} \tag{2.8}$$

2.1.2 Taut mooring system

Taut mooring systems are comprised of taut mooring lines from anchor to the seabed. No line is in contact with the seabed in static configuration. These lines are usually made of lightweight materials such as synthetic fibre ropes. A consequence of being taut is that the line stiffness is governed by the elastic stiffness (Ma et al., 2019). A taut mooring system on a floater, which is offset in the x-direction, is shown in Figure 2.5.

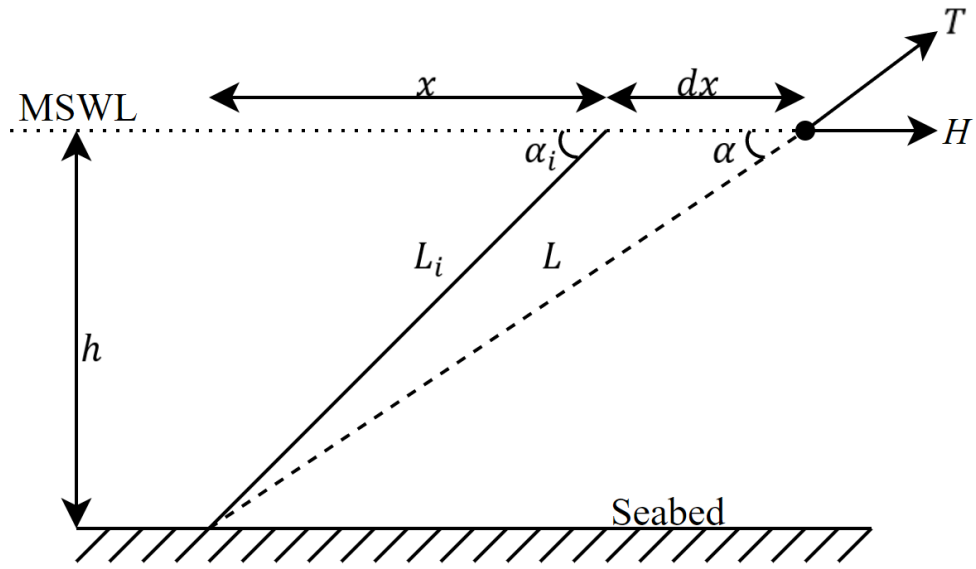

Figure 2.5: Forces in a taut mooring system

By assuming the hydrodynamic current forces are negligible (Faltinsen, 1993), the tension T can be written as

$$T = k_e dL = \frac{EA}{L_i} dL \tag{2.9}$$

where dL is the stretch of the mooring line and L_i is the initial mooring line length. The horizontal force component can be written as

$$H = T \cos \alpha \tag{2.10}$$

From geometry, it follows that the stretch of the mooring line can be given as

$$dL = dx \cos \alpha \tag{2.11}$$

where the angle α is

$$\alpha = \tan^{-1}\left(\frac{h}{x + dx}\right) \tag{2.12}$$

2.1.3 Hybrid mooring system

A hybrid mooring system consists of several components, either series or parallel connected. Hybrid mooring systems aim to enhance the pros and reduce the cons of conventional catenary and taut mooring systems. One method is to make the system more compliant by installing sections of synthetic fibre ropes in a catenary mooring system, which reduces non-linear tension responses. Another method is to replace the top and bottom segments of a synthetic fibre rope mooring line with mooring chains to increase resistance against abrasion. Other methods involve the use of clump weights or buoys. However, the complexity increases as more components are used in the system. A simplification can be used to get a first impression of the mooring stiffness if the system is restricted to series-connected components in shallow to intermediate water. The simplification allows the hybrid mooring system to be represented as a simple spring system where each component is represented by a geometric and an elastic stiffness component. Examples of hybrid mooring systems are shown in Figure 2.6.

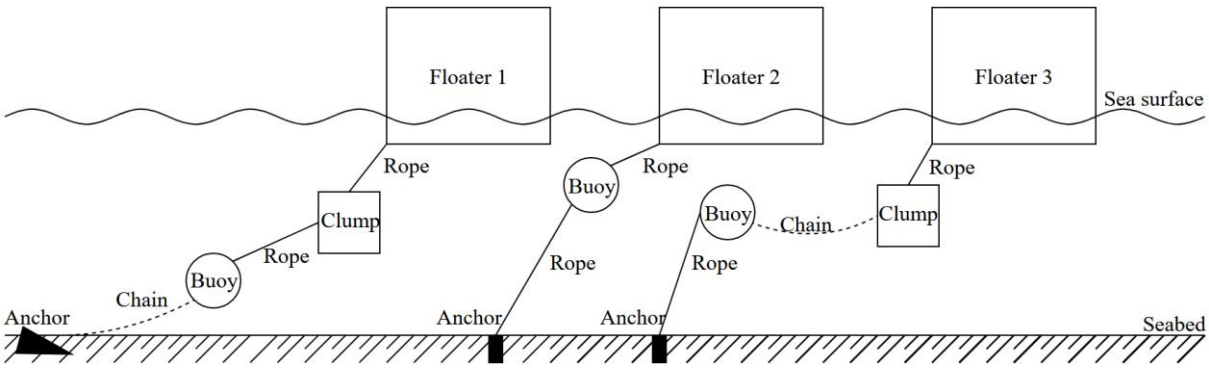

Figure 2.6: Examples of hybrid mooring systems

2.2 Mooring components

In the simplest form, a mooring system consists of a mooring line and an anchor. However, it is more common for a mooring system to be composed of several components connected with connector links or shackles.

2.2.1 Synthetic fibre rope

A synthetic fibre rope consists of multiple layers with different functions. The inner core of sub-ropes is protected from particles by a filter and abrasion by a cover. The sub-rope core is made of strands, which are made of yarn. The sub-rope core provides load-bearing capacity, whereas the filter and cover do not. Different rope characteristics are achievable by altering the configuration of the sub-ropes (Ma et al., 2019). A typical synthetic fibre rope structure is shown in Figure 2.7, where the sub-ropes are in a parallel configuration.

Synthetic fibre ropes of polyester or nylon material are commonly used in taut mooring systems. The compliant stiffness of synthetic fibre ropes reduces the non-linearity of tension responses. Other benefits are low mass, excellent fatigue properties and no corrosion. However, synthetic fibre ropes offer low resistance against abrasion and must be handled with care. Particularly wet-dry cycles for partially submerged sections should be avoided in order to prevent salt from accumulating in the fibres. Additional requirements that need attention are construction stretch, creep, and non-linear stiffness (Ma et al., 2019). Consequently, synthetic fibre ropes are complex structures requiring extensive testing and modelling for accurate representation in loading conditions.

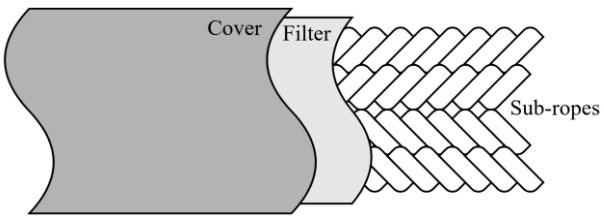

Figure 2.7: Typical synthetic fibre rope

2.2.2 Mooring chain

The most common component in a mooring system is steel chains. The widespread use of mooring chains is due to their high weight, high stiffness and good resistance against abrasion.

Additionally, mooring chains are relatively cheap and easily accessible as manufacturing is global. Hence, mooring lines entirely of chains are frequently deployed. A drawback is corrosion problems. Keeping the chain submerged in order to avoid oxygen exposure or using cathodic protection can reduce corrosion problems. Mooring chains are categorised as stud or studless chains, as shown in Figure 2.8. Studless chains are usually used for permanent mooring systems and have lower mass and longer fatigue life than stud chains. On the other hand, stud chains are easier to handle and thus used in non-permanent mooring systems. There is no difference in minimum breaking load (MBL) between the two even though studless chains are roughly 10 % lighter (Ma et al., 2019).

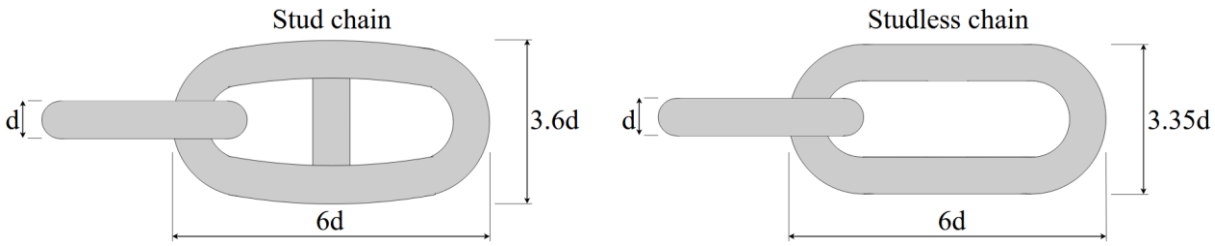

Figure 2.8: General dimensions of stud and studless chain

2.2.3 Mooring line buoy

Mooring line buoys exist in several configurations, as illustrated in Figure 2.9. All configurations are essentially a method of lowering the submerged weight of the mooring line. Buoys are usually made of synthetic foam or steel (Ma et al., 2019). Research shows that the attachment of buoys on mooring lines can reduce mooring line dynamics and reduce the non-linearity of geometric stiffness, reducing tension responses (Xu et al., 2021). Additionally, buoys can alleviate the risk of contact between the mooring line and other objects in the water column, such as a floater or the seabed. Nevertheless, introducing a mooring line buoy adds to the complexity of the line. Consequently, dynamic responses of the buoy and load-bearing capacity are important (Ma et al., 2019).

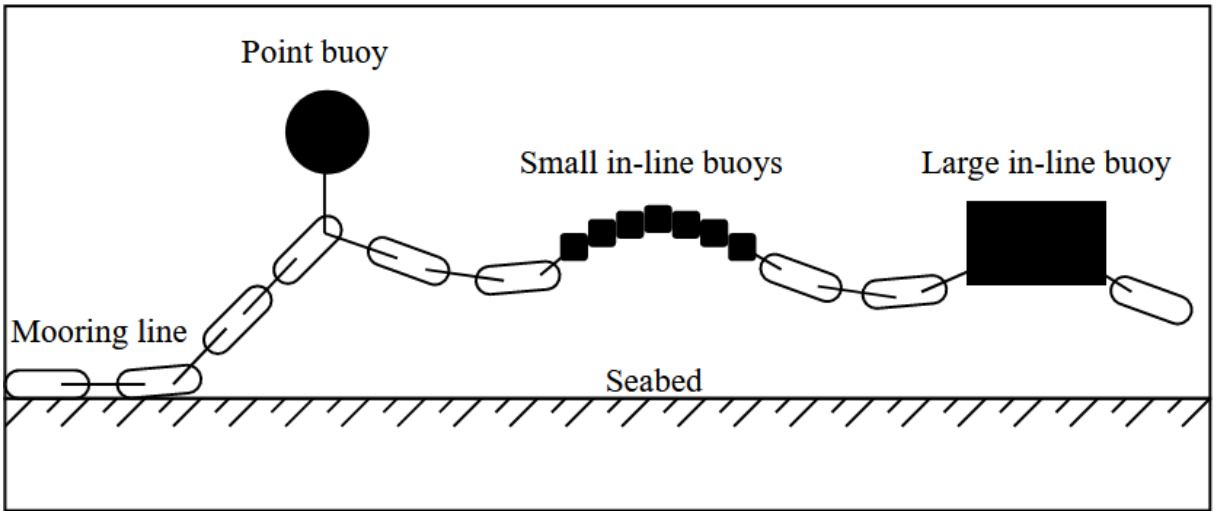

Figure 2.9: Different configurations used for mooring line buoys

2.2.4 Suction anchor

Suction anchors (SAs) are large cylinders with an open bottom. The installation procedure is to lower the anchor to the seabed, where it will self-penetrate due to its weight. Afterwards, suction is applied to the top valve to create negative pressure, which drives the anchor deeper and secures it. SAs generally have high precision and resist vertical and horizontal loading (Ma et al., 2019). Therefore, SAs are well suited for the highly dynamic loading experienced by FOWTs. However, the drawback is an increased cost due to increased installation complexity. An illustration of the installation and operating phases of a SA is shown in Figure 2.10.

2.2.5 Drag-embedment anchor

The use of drag-embedment anchors (DEAs) is widespread and usually the preferred method of anchoring. There are several reasons for its popularity, but mostly, it boils down to cost, ease of installation and removal. The standard installation procedure is to drag the anchor along the seabed until the anchor is secured, providing good resistance against horizontal loads. Nonetheless, DEA is strongly dependent on soil conditions. Vertical holding capacity is

determined by soil penetration which is hard to predict. Less soil penetration in sand and stiff clays is expected, providing close to zero vertical load capacity. Due to less soil penetration, the mooring line lies on the seabed. As a result, DEA is commonly used in chain catenary mooring systems, which can lie on the seabed and account for vertical loads. Soft clay, on the other hand, may allow for deep soil penetration and the use of a taut mooring system (Ma et al., 2019). An illustration of the installation and operating phases of a DEA is shown in Figure 2.11.

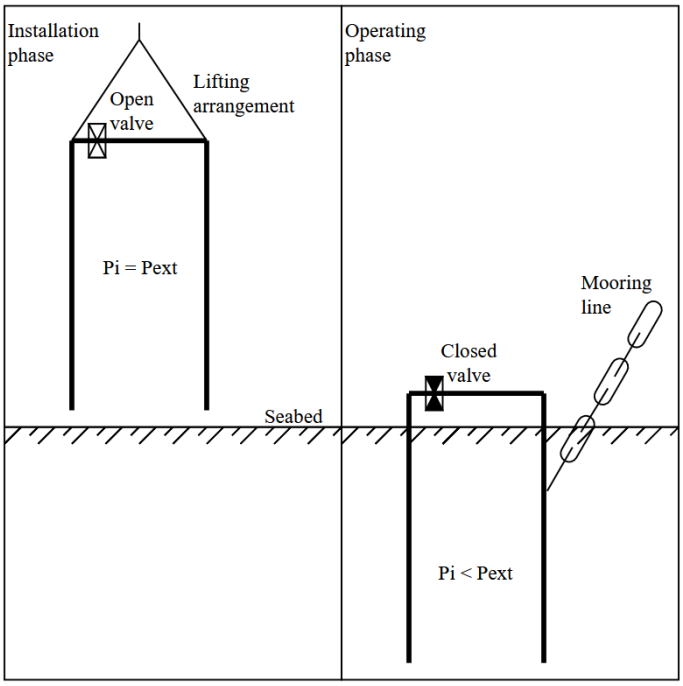

Figure 2.10: Suction anchor in installation and operating phases

.

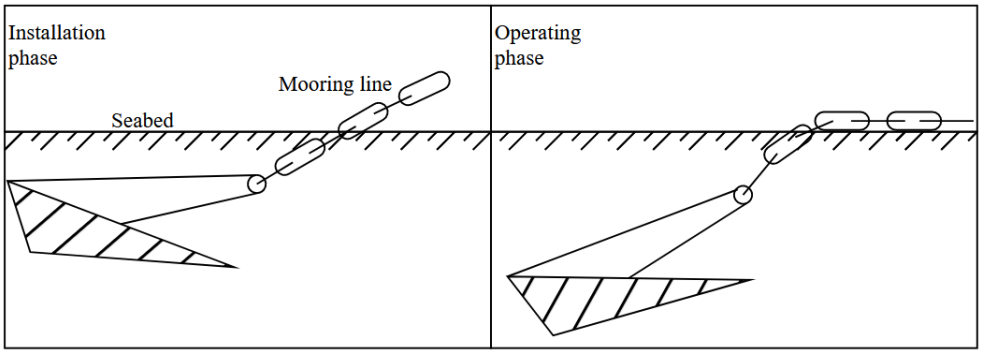

Figure 2.11: DEA in installation and operating phases

References

Faltinsen, O. (1993). Sea loads on ships and offshore structures (Vol. 1). Cambridge university press.

Ma, K.-T., Luo, Y., Thomas Kwan, C.-T., & Wu, Y. (2019). Mooring System Engineering for Offshore Structures. Elsevier.

Xu, K., Larsen, K., Shao, Y., Zhang, M., Gao, Z., & Moan, T. (2021). Design and comparative analysis of alternative mooring systems for floating wind turbines in shallow water with emphasis on ultimate limit state design. Ocean Engineering, 219, 108377.

Chapter 3 - Environmental loads and structural responses

Floating offshore wind turbines are subject to environmental loads from wind, waves and currents. The wind turbine is also subject to high aerodynamic forces, resulting in high mean loads. The motion of the structure is caused by the combined loading of these four contributors and will govern the tension response in the mooring line. Unique for STFC is the additional wave load contributions on the WECs. The loading can be categorised based on their excitation regimes:

- Mean loads are constant. For STFC, mean wind, mean wave drift force, current and aerodynamic thrust are considered mean loads. The mean loads govern the offset of the floater
- Wave frequency (WF) is cyclic loading with 5 – 30 s periods. It adds to maximum tension and accumulates fatigue damage
- Low frequency (LF) is cyclic loading with 60 – 200 s periods. Second-order wave drift forces and wind gusts are typically in this range

An illustration of STFC subject to wind and wave loads is shown in Figure 3.1. Ocean current and marine growth is not considered for STFC.

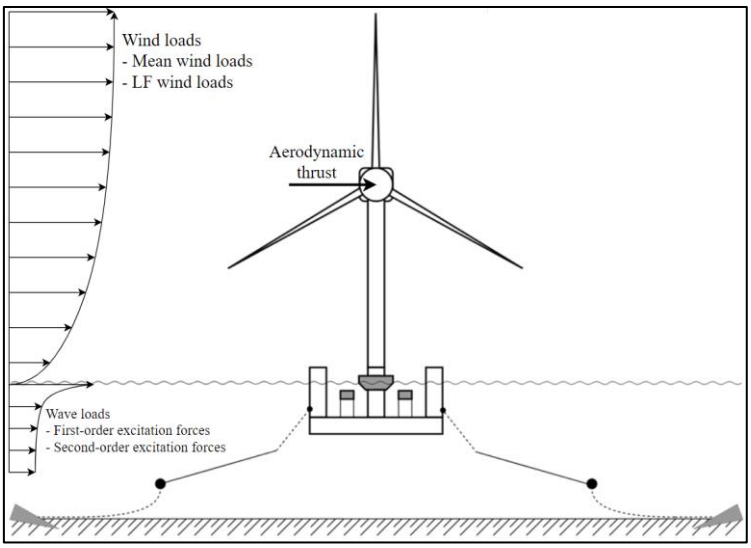

Figure 3.1: STFC subject to wind and wave loads

3.1 Hydrodynamic loads

Hydrodynamic loads considered in this thesis are first- and second-order wave excitation loads, which are most important for a mooring system.

3.1.1 First-order wave excitation loads

First-order wave loads arise when only the linear wave amplitude terms are kept in the boundary value problem when solving for the velocity potential φ. First-order loads can be split into two components. Diffraction forces consider the disturbance of the wave pressure field due to the structure, whereas the undisturbed wave pressure field is known as the Froude-Krylov force. The wave excitation force is then the pressure field integrated over the wetted surface for each DOF. Using potential theory to describe the pressure field, then the wave excitation force can be written as (Faltinsen, 1993)

$$q_{wa}^{(1)} = \int_{S_o} p_d n_j dS = \rho \int_{S_o} \frac{\partial \varphi_0}{\partial t} n_j dS + \rho \int_{S_o} \frac{\partial \varphi_v}{\partial t} n_j dS \tag{3.1}$$

where p_d is linear dynamic pressure, n_j is a normal vector with respect to the DOF, ρ is the fluid density, φ_0 is wave velocity potential, φ_v is diffraction velocity potential, t is time, and S is the wetted surface.

Slender structures with a diameter of less than 5 times the wavelength can have their wave and current forces estimated by the Morison equation (Morison et al., 1950)

$$dF = dF_I + dF_D = C_m \rho V \frac{du}{dt} + \frac{1}{2} C_D \rho A u|u| \tag{3.2}$$

where F_I and F_D are inertia and drag force contributions, respectively. C_m is the inertia coefficient, often represented as $C_m = 1 + C_a$, where C_a is added mass coefficient. C_D is drag coefficient, V is body volume, A is cross-sectional area normal to the flow and u is flow velocity. Added mass and drag coefficient for common cross-sections can be found in standards or determined through testing. If the slender element has velocity v, then the Morison equation

is general by considering relative velocities between flow and elements and can be written as (Morison et al., 1950)

$$dF = \rho V \frac{du}{dt} + C_a \rho V \left(\frac{du}{dt} - \frac{dv}{dt}\right) + \frac{1}{2} C_D \rho A (u - v)|u - v| \tag{3.3}$$

3.1.2 Second-order wave excitation loads

Second-order excitation wave loads arise when all linear and square terms of wave amplitude in the boundary value problem are used. This results in mean and oscillation forces with difference- or sum-frequency in addition to the linear solution (Faltinsen, 1993). Difference-frequency loads, the mean wave drift load, and slowly varying wave loads are important for moored systems. These loads cause structure offset, contributing to the tension responses in the mooring line. Additionally, these loads vary with periods close to those of FOWTs surge, sway and yaw natural periods, which may cause resonance. However, second-order excitation wave loads are typically small in amplitude when not close to resonance. Second-order excitation loads are calculated using full quadratic transfer functions (QTFs) or Newman's approximation (Newman, 1974). However, full QTFs are preferred in shallow and intermediate water as the performance of Newman's approximation is poor (Faltinsen, 1993).

Following the procedure by Orcina (2023) to calculate second-order excitation loads, full QTF is applied to all pairs of wave components up to the n-th regular wave component present in all considered wave trains. The wave drift $q_d^{(2)}$ and sum-frequency $q_s^{(2)}$ second-order excitation loads are given as

$$\begin{aligned} q_d^{(2)} &= \sum_{i=1}^{n}\sum_{j=1}^{n} Re\left\{Q_d(\beta_i, \beta_j, \tau_i, \tau_j)\zeta_i\zeta_j \exp\left(i(\omega_i - \omega_j)t - (\phi_i - \phi_j)\right)\right\} \\ q_s^{(2)} &= \sum_{i=1}^{n}\sum_{j=1}^{n} Re\left\{Q_s(\beta_i, \beta_j, \tau_i, \tau_j)\zeta_i\zeta_j \exp\left(i(\omega_i + \omega_j)t - (\phi_i + \phi_j)\right)\right\} \end{aligned} \tag{3.4}$$

where the properties of the i-th wave component are

$$\begin{aligned}\beta_i &= relative\ direction\ to\ the\ vessel\ heading\\ \zeta_i &= amplitude\\ \phi_i &= phase\ lag\\ \tau_i &= period\\ \omega_i &= 2\pi/\tau_i\end{aligned} \tag{3.5}$$

The full wave drift QTF is a complex-valued function of the properties β_i, β_j, τ_i and τ_j of wave component *i* and *j* and is given by

$$Q_d(\beta_i, \beta_j, \tau_i, \tau_j) = \zeta_d(\beta_i, \beta_j, \tau_i, \tau_j) \exp\left(-i\phi_d(\beta_i, \beta_j, \tau_i, \tau_j)\right) \tag{3.6}$$

Similarly, the full sum-frequency QTF is

$$Q_s(\beta_i, \beta_j, \tau_i, \tau_j) = \zeta_s(\beta_i, \beta_j, \tau_i, \tau_j) \exp\left(-i\phi_s(\beta_i, \beta_j, \tau_i, \tau_j)\right) \tag{3.7}$$

As a result, the second-order excitation load can be written as the sum of wave drift and sum-frequency loads

$$q_{wa}^{(2)} = q_d^{(2)} + q_s^{(2)} \tag{3.8}$$

3.1.3 Irregular sea state

The sea surface of an irregular sea state can be described using linear theory as the sum of different wave components

$$\zeta(t) = \sum_{i=1}^{n} \zeta_{ai} \cos(\omega_i + \phi_i) \tag{3.9}$$

where ζ_{ai} is the wave amplitude, assumed to be a stationary ergodic process and follow a zero mean Gaussian distribution. The wave frequency is ω_i. The random phase angle is ϕ_i which is uniformly distributed between $[0, 2\pi]$. The energy for one wave component can be written as

$$E_{wi} = \frac{1}{2}\rho g \zeta_{ai}^2 \tag{3.10}$$

where ρ is the fluid density, g is the gravitational acceleration. For a given sea state, the total energy is the sum of the energy components up to the n-th component

$$E_w = \rho g \sum_{i=1}^{n} \frac{1}{2} \zeta_{ai}^2 \tag{3.11}$$

The same energy is the area beneath a wave spectrum curve. Therefore, the wave amplitude of a wave component with frequency ω_i can be found using a wave spectrum, $S(\omega_i)$ and a small frequency interval $\Delta\omega$, through the following relation

$$\frac{1}{2} \zeta_{ai}^2 = S(\omega_i)\Delta\omega \tag{3.12}$$

Therefore, the wave spectrum has the necessary information to describe an irregular sea state. The Jonswap spectrum is commonly used in the North Sea to describe sea states (Hasselmann et al., 1973). It is a Pierson-Moskowitz spectrum adjusted to fit wave data collected in the North Sea and describes a growing wind sea. The Jonswap spectrum can be defined as (DNV RP-C205 , 2021)

$$S(\omega) = A_\gamma \frac{5}{16} h_s^2 \omega_p^4 \omega^{-5} \exp\left(-\frac{5}{4}\left(\frac{\omega}{\omega_p}\right)^{-4}\right) \gamma^{\exp\left(-0.5\left(\frac{\omega-\omega_p}{\sigma\omega_p}\right)^2\right)} \tag{3.13}$$

where h_s is the significant wave height, ω_p is the peak frequency found as $\omega_p = 2\pi/t_p$ where t_p is the peak period. γ is the peak shape parameter and is assumed to be 3.3. The normalisation factor is $A_\gamma = 1 - 0.287 \ln(\gamma)$. The spectral width parameter is

$$\sigma = \begin{cases} 0.07 \; for \; \omega \leq \omega_p \\ 0.09 \; for \; \omega > \omega_p \end{cases} \tag{3.14}$$

As seen, the Jonswap spectrum can be described by two parameters, H_s and T_p, which in turn can describe an irregular sea state.

3.2 Wind loads

Winds can be split into two components. One mean component which is dependent on height z above the ground, $\overline{U}(z)$, and one fluctuating part, $u(z,t)$, that is also dependent on time, t

$$U(z,t) = \overline{U}(z) + u(z,t) \tag{3.15}$$

Turbulence intensity is used to measure the turbulence of the wind condition. It is the ratio between the standard deviation of the wind and the mean wind speed

$$I(z) = \frac{\sigma_u}{\overline{U}(z)} \tag{3.16}$$

The mean wind profile can be described as a power law function (Jonkman and Kilcher, 2012)

$$\overline{U}(z) = \overline{U}(z_{ref})\left(\frac{z}{z_{ref}}\right)^{\kappa} \tag{3.17}$$

where z_{ref} is a reference height, $\overline{U}(z_{ref})$ is the mean wind speed at reference height, and κ is the surface roughness factor. The reference height is usually 10 m, and the mean wind speed is the 10-minute mean. The standard deviation can be defined as

$$\sigma_u = \frac{\overline{U}(z_{ref})}{\ln\left(\frac{z_{ref}}{z_0}\right)} + 1.8432\, I(z) \tag{3.18}$$

3.2.1 Turbulence spectra and coherence model

A wind spectrum can describe short-term stationary wind conditions, including turbulence. In this case, represented by the Kaimal wind spectrum expression (IEC, 2019)

$$S_k(f) = \frac{4\sigma_k^2 \frac{L_k}{\overline{U}_{ref}}}{\left(1 + 6f\frac{L_k}{\overline{U}_{ref}}\right)^{\frac{5}{3}}} \tag{3.19}$$

where f is frequency, L_k is an integral length scale parameter, $k = u, v, w$ denotes direction in x, y, z, respectively. The standard deviation in v and w can be found by the following relations

$$\begin{aligned} \sigma_v &= 0.8\sigma_u \\ \sigma_w &= 0.5\sigma_u \end{aligned} \tag{3.20}$$

The integral length scale parameter is defined as

$$L_k \begin{cases} 8.10\Lambda_U \; for \; k = u \\ 2.70\Lambda_U \; for \; k = v \\ 0.66\Lambda_U \; for \; k = w \end{cases} \tag{3.21}$$

and the longitudinal scale parameter is

$$\Lambda_U = \begin{cases} 0.7z & for \; z < 60 \; m \\ 42 & for \; z \geq 60 \; m \end{cases} \tag{3.22}$$

The coherence model to be used is shown in the following expression

$$Coh(r, f) = exp\left(-\alpha\sqrt{\left(\frac{fr}{\overline{U}_{ref}}\right) + \left(0.12\frac{r}{L_c}\right)^2}\right) \tag{3.23}$$

where r is the length of the projection of the separation vector between two points on a plane perpendicular to the wind direction. The coherence decrement is $\alpha = 12$, and the coherence scale parameter is $L_c = 5.67 \min(60, z_{hub})$.

3.2.2 Aerodynamic loads

Following the description by SINTEF Ocean, 2022a, the aerodynamic load acting in direction $i = x, y, z$ on elements which are not considered an airfoil can be calculated using the following equation

$$q_{wi} = C_{wi}(\alpha) v_r^2 \tag{3.24}$$

where C_{wi} is the instantaneous relative direction aerodynamic load coefficient, v_r is the relative speed between the body and the wind, α is the relative velocity direction in a local coordinate system. The non-dimensional aerodynamic load coefficient for an axisymmetric cross-section can be written as

$$C_{wi} = \frac{1}{2} \rho_{air} C_d D_i \tag{3.25}$$

where ρ_{air} is the density of air, D_i is a representative diameter and C_d is a drag coefficient, which can be found in standards or determined through testing. For a circular cross-section with a diameter D

$$\begin{aligned} D_x &= \pi D \\ D_y &= D_z = D \end{aligned} \tag{3.26}$$

The aerodynamic loads acting on the airfoils of the wind turbine are modelled based on the blade element momentum (BEM) theory which combines momentum theory and blade element theory. The principle of BEM is that local forces generated at the airfoil, using empirical lift and drag coefficients, are balanced with the momentum change of air due to the flow through the rotor disk. In order to account for the simplifications used to derive the BEM theory, several correction factors are available. Prandtl, Glauert, dynamic wake, dynamic stall, skewed inflow, upwind tower influence, and downwind tower influence are commonly used correction factors.

3.3 Hydrodynamic equation of motion

The equation of motion describes the motions of a body with respect to time, frequency or both. For a 6 DOF body in sinusoidal motion, the equation of motion can be written as (SINTEF Ocean, 2022b)

$$\big(\mathbf{M} + \mathbf{A}(\omega)\big)\ddot{\mathbf{x}} + \mathbf{C}(\omega)\dot{\mathbf{x}} + \mathbf{D_l}\dot{\mathbf{x}} + \mathbf{D_q}\dot{\mathbf{x}}|\dot{\mathbf{x}}| + \mathbf{K}(x)\mathbf{x} = \mathbf{Q}(t, \mathbf{x}, \dot{\mathbf{x}}) \tag{3.27}$$

where $\mathbf{M}$ is the mass matrix, $\mathbf{A}$ is the added mass frequency-dependent matrix, $\mathbf{x}$ is the displacement vector, $\mathbf{C}$ is the potential damping frequency-dependent matrix, $\mathbf{K}$ is the stiffness matrix, $\mathbf{D_l}$ and $\mathbf{D_q}$ are linear and quadratic damping matrices, respectively. The excitation force vector is $\mathbf{Q}$ which can be written as

$$\mathbf{Q}(t, \mathbf{x}, \dot{\mathbf{x}}) = q_{wi} + q_{wa}^{(1)} + q_{wa}^{(2)} + q_{ext} \tag{3.28}$$

The equation of motion is frequency- and time-dependent, which is challenging to solve. One method commonly used to solve the equation of motion is solution by convolution integral (SINTEF Ocean, 2022b). The idea is to transform frequency-dependent terms into time-dependent terms. First, the equation of motion is written as

$$\big(\mathbf{M} + \mathbf{A}(\omega)\big)\ddot{\mathbf{x}} + \mathbf{C}(\omega)\dot{\mathbf{x}} + \mathbf{K}(x)\mathbf{x} = \mathbf{f}'(t) = \mathbf{Q}(t, \mathbf{x}, \dot{\mathbf{x}}) - \mathbf{D_l}\dot{\mathbf{x}} - \mathbf{D_q}\dot{\mathbf{x}}|\dot{\mathbf{x}}| \tag{3.29}$$

The frequency-dependent parameters are isolated on the left side of the equation

$$\mathbf{A}(\omega)\ddot{\mathbf{x}} + \mathbf{C}(\omega)\dot{\mathbf{x}} = \mathbf{f}(t) = \mathbf{f}'(t) - \mathbf{K}(x)\mathbf{x} - \mathbf{M}\ddot{\mathbf{x}} \tag{3.30}$$

By assuming that the force is sinusoidal at one frequency, ω, the previous equation in the frequency-domain can be written as

$$\big(\boldsymbol{i}\omega\mathbf{A}(\omega) + \mathbf{C}(\omega)\big)\boldsymbol{i}\omega\mathbf{X}(\omega) = \mathbf{F}(\omega) \tag{3.31}$$

The added mass and damping matrices $\mathbf{A}$ and $\mathbf{C}$ can be rewritten using the following relationship

$$\begin{cases} \mathbf{A}(\omega) = \mathbf{A}_\infty + \mathbf{a}(\omega) & where\ \mathbf{A}_\infty = \mathbf{A}(\omega = \infty) \\ \mathbf{C}(\omega) = \mathbf{C}_\infty + \mathbf{c}(\omega) & where\ \mathbf{C}_\infty = \mathbf{0} \end{cases} \tag{3.32}$$

which yields the following equation

$$-\omega^2 \mathbf{A}_\infty \mathbf{X}(\omega) + \left(\boldsymbol{i}\omega \mathbf{a}(\omega) + \mathbf{c}(\omega)\right)\boldsymbol{i}\omega \mathbf{X}(\omega) = \mathbf{F}(\omega) \tag{3.33}$$

Inverse Fourier transform is used while the retardation function $\mathbf{h}(t-\tau) = 0$ for $t < 0$, which yields the following equation

$$\mathbf{A}_\infty \ddot{\mathbf{x}}(\boldsymbol{t}) + \int_0^t \mathbf{h}(t-\tau)\dot{\mathbf{x}}(\tau)d\tau = \mathbf{f}(t) \tag{3.34}$$

Substituting $\mathbf{f}(t)$ and $\mathbf{f}'(t)$ yields the equation of motion in the time-domain

$$(\mathbf{M} + \mathbf{A}_\infty)\ddot{\mathbf{x}} + \mathbf{D_l}\dot{\mathbf{x}} + \mathbf{D_q}\dot{\mathbf{x}}|\dot{\mathbf{x}}| + \mathbf{K}(x)\mathbf{x} + \int_0^t \mathbf{h}(t-\tau)\dot{\mathbf{x}}(\tau)d\tau = \mathbf{Q}(\boldsymbol{t}, \mathbf{x}, \dot{\mathbf{x}}) \tag{3.35}$$

The retardation function $\mathbf{h}(\tau)$ for $\tau > 0$ is found by Fourier transforming the frequency-dependent added mass and damping terms

$$\mathbf{h}(\tau) = \frac{2}{\pi}\int_0^\infty \mathbf{c}(\omega)\cos(\omega\tau)\,d\omega = -\frac{2}{\pi}\int_0^\infty \mathbf{a}(\omega)\sin(\omega\tau)\,d\omega \tag{3.36}$$

Hence it is possible to calculate the frequency-dependent added mass and damping if the retardation function is known. One method is to estimate the retardation function using the potential damping found from test data or appropriate software.

3.4 Dynamic equilibrium

The dynamic equilibrium of a spatially discretized finite element system model is highly non-linear and can be represented by the following expression (SINTEF Ocean, 2022a)

$$\boldsymbol{R}^I(\boldsymbol{r},\ddot{\boldsymbol{r}},t)+\boldsymbol{R}^D(\boldsymbol{r},\dot{\boldsymbol{r}},t)+\boldsymbol{R}^S(\boldsymbol{r},t)=\boldsymbol{R}^E(\boldsymbol{r},\dot{\boldsymbol{r}},t) \tag{3.37}$$

where $\boldsymbol{R}^I$, $\boldsymbol{R}^D$, $\boldsymbol{R}^S$, $\boldsymbol{R}^E$ are inertia, damping, internal structural reaction and external force vectors, respectively. $\boldsymbol{r},\dot{\boldsymbol{r}},\ddot{\boldsymbol{r}}$ are structural displacement, velocity and acceleration vectors, respectively. The non-linearity stems from several relationships. First, displacement-dependent inertia and damping forces. Second, coupling between external load and structural displacement and velocity. Third, a non-linear relation between internal forces and displacements.

The internal structural reaction force vector $\boldsymbol{R}^S$ is determined through static finite element analysis. The external force vector represents weight, buoyancy, forced displacements, point forces, drag and wave-particle acceleration terms in the Morison equation. The inertia force vector can be expressed as

$$\boldsymbol{R}^I(\boldsymbol{r},\dot{\boldsymbol{r}},t)=\left(\boldsymbol{M}^S+\boldsymbol{M}^F(\boldsymbol{r})+\boldsymbol{M}^H(\boldsymbol{r})\right)\ddot{\boldsymbol{r}} \tag{3.38}$$

where $\boldsymbol{M}^S$, $\boldsymbol{M}^F$, $\boldsymbol{M}^H$ are structural, internal fluid and displacement-dependent hydrodynamic mass matrices, respectively. An extra inertia force vector representing a local Coriolis centripetal load is included for beam cross-sections. The damping force vector can be expressed as

$$\boldsymbol{R}^D(\boldsymbol{r},\dot{\boldsymbol{r}})=\left(\boldsymbol{C}^S(\boldsymbol{r})+\boldsymbol{C}^H(\boldsymbol{r})+\boldsymbol{C}^D(\boldsymbol{r},\dot{\boldsymbol{r}})\right),\dot{\boldsymbol{r}} \tag{3.39}$$

where $\boldsymbol{C}^S$, $\boldsymbol{C}^H$ are internal structural and hydrodynamic damping matrices, respectively. $\boldsymbol{C}^D$ is a matrix representing specified discrete dashpot dampers.

Due to the highly non-linear nature of the dynamic equilibrium equation, a step-by-step numerical integration technique is required in order to solve the equation. Either a full non-linear time domain analysis or a linearized time domain analysis can be used.

References

DNV. (2021). DNV-RP-C205: Environmental conditions and environmental loads.

Faltinsen, O. (1993). Sea loads on ships and offshore structures (Vol. 1). Cambridge University Press.

Hasselmann, K., Barnett, T. P., Bouws, E., Carlson, H., Cartwright, D. E., Enke, K., Ewing, J. A., Gienapp, A., Hasselmann, D. E., & Kruseman, P. (1973). Measurements of wind-wave growth and swell decay during the Joint North Sea Wave Project (JONSWAP). Ergaenzungsheft zur Deutschen Hydrographischen Zeitschrift. Reihe A. Nr. 122

IEC-61400-1. (2019). Wind energy generation systems - Part 1: Design requirements.

Jonkman, B. J., & Kilcher, L. (2012). TurbSim user's guide: version 1.06.00. National Renewable Energy Laboratory, Golden, CO, USA.

Morison, J. R., Johnson, J. W., & Schaaf, S. A. (1950). The force exerted by surface waves on piles. Journal of Petroleum Technology, 2(05), 149-154.

Newman, J. N. (1974). Second-order slowly varying forces on vessels in irregular waves. In Proceedings of the international symposium on dynamics of marine vehicles and structures in waves. London, UK, 1974.

Orcina. (2023). Orcina :: OrcaFlex documentation. https://www.orcina.com/webhelp/OrcaFlex/Content/

SINTEF Ocean. (2022a). RIFLEX :: SIMA documentation. https://sima.sintef.no/doc/4.4.0/riflex/index.html

SINTEF Ocean. (2022b). SIMO :: SIMA documentation. https://sima.sintef.no/doc/4.4.0/simo/index.html

Chapter 4 - Numerical modelling

4.1 Description of STFC

The combined wind and wave energy system STFC consist of 4 main components:

1. Supporting structure
2. Wind turbine
3. Torus WEC
4. Three flap type WECs

An illustration of STFC without the wind turbine is shown in Figure 4.1. Additional details and illustrations of STFC can be found in Chapter 5, Chapter 6, research by Lee et al. (2022) and the master thesis of Tryfonidis (2022).

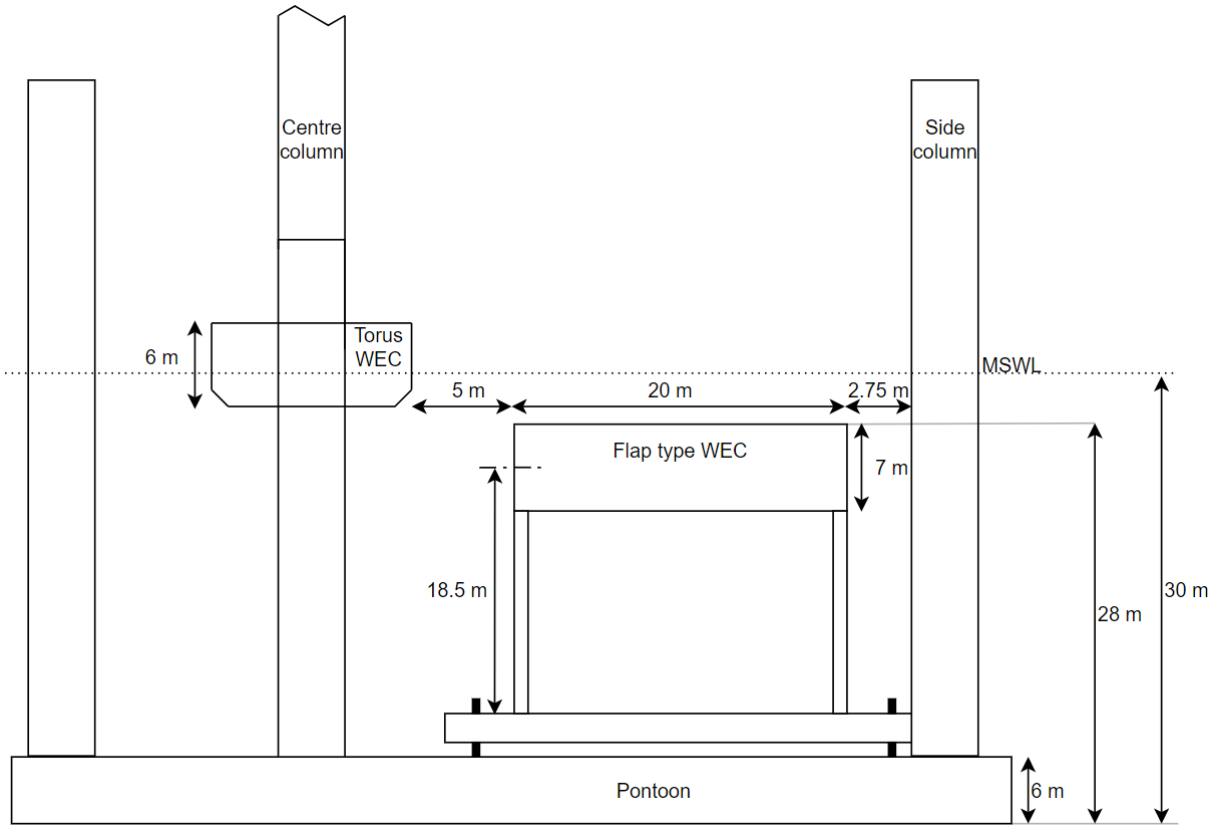

Figure 4.1: Dimensions of STFC

4.1.1 Wind turbine

STFC use a 5 MW NREL reference wind turbine by Jonkman et al. (2009) to capture wind energy. The wind turbine uses a variable speed and variable pitch control strategy. The wind turbine has a cut-in speed of 3 m/s, a rated speed of 11,4 m/s and a cut-out speed of 25 m/s. Between cut-in and rated speed, the objective of the wind turbine is to maximise power output. Conversely, between rated speed and cut-out, the objective of the wind turbine is to prevent overloading and maintain a constant generator speed. Therefore, the blades start pitching to control the generator speed. The maximum thrust is approximately 800 kN at the rated speed. The wind turbine consists of three main components: the blades, the tower, the nacelle, and the hub. The wind turbine blades are modelled as distributed mass flexible beam elements. The beam elements have cross-sections with two symmetric planes, which capture blade characteristics in flap- and edge-wise directions. The tower and generator shaft are modelled as beam elements with an axisymmetric cross-section. Additionally, the generator shaft comprises a rotating and a non-rotating component separated by a flexible joint. The generator torque is applied at the flexible joint to employ the control strategy. A proportional integral (PI) controller with proportional gain $k_p = 0.60873$ and integral gain $k_i = 0.086962$ is used. The wind turbine hub and nacelle are modelled as integrated mass rigid bodies.

4.1.2 Torus WEC

The torus WEC is a torus-shaped buoy installed through the centre column of CSC. It is constrained to move with the CSC hull in surge, sway, roll and pitch. Relative yaw motion between the CSC hull and torus WEC is restricted to +/- 50 degrees, and relative heave motion is restricted to +/- 3 m. Three contact bearings ensure frictionless contact between the torus WEC and column. Energy from waves is extracted utilising the relative heave motion between the torus WEC and semi-submersible hull. The torus WEC is modelled as a rigid body, while the PTO is modelled as a linear spring-damping system. The spring stiffness is 10 kN/m, and the damping coefficient is 8000 kNs/m. The torus WEC is illustrated in Figure 4.2, and its mass

properties are given in Table 4.1, where centre of gravity (CoG) is measured relative to the origin at MSWL.

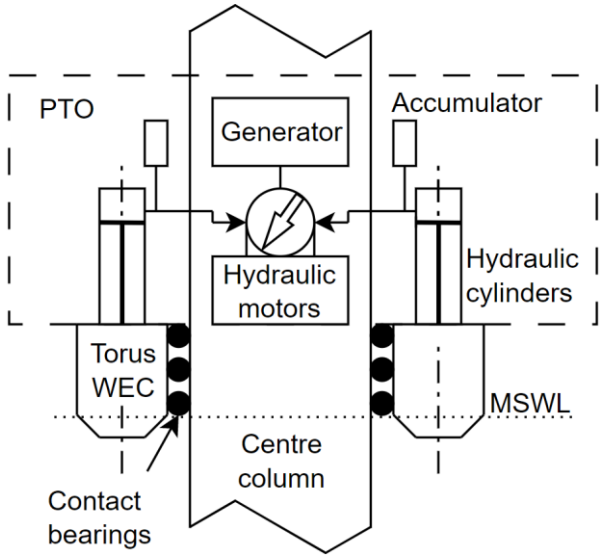

Figure 4.2: Torus WEC configuration.
Reproduced according to Lee et al. (2022)

Table 4.1: Mass properties of a torus WEC. Reproduced according to Tryfonidis (2022)

Mass	(kg)	4.2378E5
I_{xx}	(kgm^2)	1.0765E7
I_{yy}	(kgm^2)	1.0765E7
I_{zz}	(kgm^2)	2.0587E7
CoG	(m)	-0.9

The power production of a torus WEC is calculated as follows

$$P_t = c_{t_{PTO}} v_r^2 \tag{4.1}$$

where $c_{t_{PTO}}$ is the damping coefficient of the torus WEC PTO and v_r is the relative heave velocity between the torus WEC and CSC hull.

4.1.3 Flap type WEC

The flap type WEC consists of an elliptic cylindrical buoy connected to the PTO through two rigid supporting arms mounted on the pontoons. The flaps are rigid bodies where the buoyancy is represented by an upward point load of 2884 kN. The flap type WEC is fully submerged to a depth of 2 m in its upright position. The hydrodynamic properties are generated when the flap is upright. The flap type WECs extract energy from the rotational motion of incoming waves.

The flap can rotate freely, and this rotational motion drives a shaft which produces power through a generator. The flap type WEC is illustrated in Figure 4.3, and the mass properties of one flap type WEC are given in Table 4.2, where CoG is measured relative to the origin at MSWL.

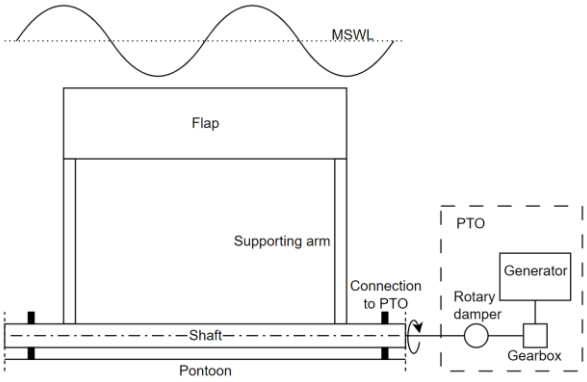

Figure 4.3: Flap type WEC configuration. Reproduced according to Lee et al. (2022)

Table 4.2: Mass properties of one flap type WEC. Reproduced according to Tryfonidis (2022)

Mass	(kg)	1E5
I_{xx}	(kgm^2)	3.68E6
I_{yy}	(kgm^2)	7.53E6
I_{zz}	(kgm^2)	4.17E6
CoG	(m)	-5.5

The power production of one flap type WEC can be calculated as follows

$$P_f = 2 * c_{flex\ joint}\omega^2_{flex\ joint} \tag{4.2}$$

where $c_{flex\ joint}$ is the damping coefficient for each flex joint and $\omega_{flex\ joint}$ is the angular velocity of the flex joint. The angular velocity, $\omega_{flex\ joint}$, can be estimated from the rotational velocity of the flap because the supporting arms with length are r_{arm} are considered rigid

$$\omega_{flex\ joint} = \frac{v_{flap}}{r_{arm}} \tag{4.3}$$

4.1.4 CSC semi-submersible

The semi-submersible CSC hull proposed by Luan et al. (2014) supports the 5 MW NREL reference wind turbine and WECs. CSC consists of 4 columns, one centre column and three side columns spaced 120 degrees apart. The side columns are connected to the centre column

by three pontoons. The side columns can be ballasted to adjust the draft. Therefore, the additional mass and buoyancy due to WECs are accounted for by ballasting the side columns. Steiner's theorem is used to calculate the new moments of inertia due WECs. The side column generates the restoring forces of the floater. CSC has a brace-less configuration, which provides the necessary space to install WECs. CSC operates with a draft of 30 m while the centre column freeboard is 10 m, and the side column freeboard is 20 m. CSC is modelled as an integrated mass rigid body with 6 DOF. The mass properties of CSC with ballast and a 5 MW NREL reference wind turbine are shown in Table 4.3.

Table 4.3: Mass properties of a ballasted CSC semi-submersible with a 5 MW NREL reference wind turbine (Luan et al., 2014)

Mass	(kg)	1.0502E7
I_{xx}	(kgm^2)	1.0447E10
I_{yy}	(kgm^2)	1.0447E10
I_{zz}	(kgm^2)	8.1985E9
CoG	(m)	-18.45

4.2 Mooring system

The mooring system is modelled in RIFLEX as slender bar elements, as shown in Figure 4.4. Super-nodes are defined at the fairlead and anchor. The bar elements can only move in the three translational DOFs. Each segment is homogeneous in terms of cross-sectional properties. The segment is discretized into smaller elements. Buoys are specified as nodal components at the start or end of a segment with mass, volume and hydrodynamical coefficients as inputs. The seabed is modelled as flat without friction.

Slender mooring lines are subject to non-linear effects that must be considered. The most important ones are (SINTEF Ocean, 2022a)

- Geometric stiffness
- Non-linear material properties
- Hydrodynamic loading according to the general Morison equation (Morison et al., 1950)
- Integration of loading to actual surface elevation
- Contract problems

These are accounted for by the dynamic equilibrium equation solved by non-linear time analysis.

Steel chains are modelled as equivalent slender bar elements with stiffness EA_{chain}. Synthetic fibre ropes are modelled as slender bar elements. However, EA_{fibre} is dependent on a tension-strain relationship. Several models exist for modelling the stiffness. In this study, the Syrope model is used.

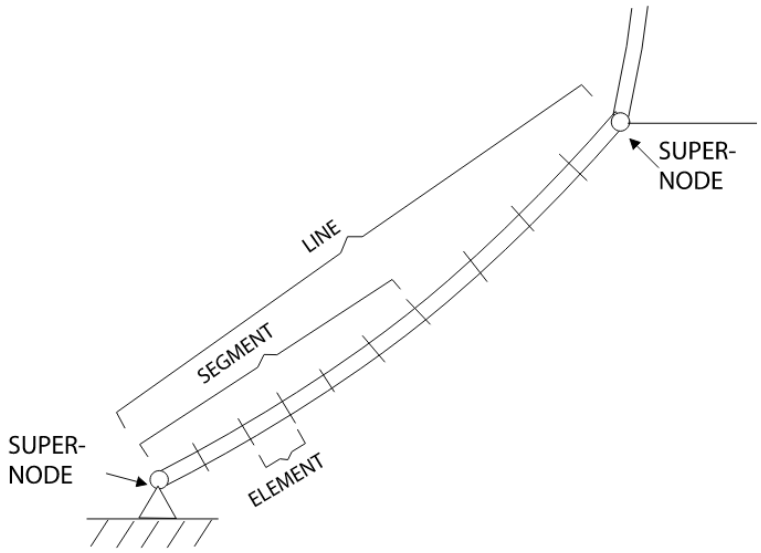

Figure 4.4: System definition terms, discretization of a mooring line in RIFLEX (SINTEF Ocean, 2022a)

4.2.1 The Syrope model

The Syrope model was proposed by Falkenberg et al. (2017) and is recommended by DNV RP-E305 (2021a). Stiffness EA_{fibre} of a synthetic fibre rope is represented by a tension-strain relationship depending on load rate and history. Four curves, as shown in Figure 4.5, are used in the Syrope model to describe the tension-strain relationship of a synthetic fibre rope. The slope of each curve represents a changing stiffness and is seen to be non-linear

$$EA_{fibre} = \frac{dT}{d\epsilon} \tag{4.4}$$

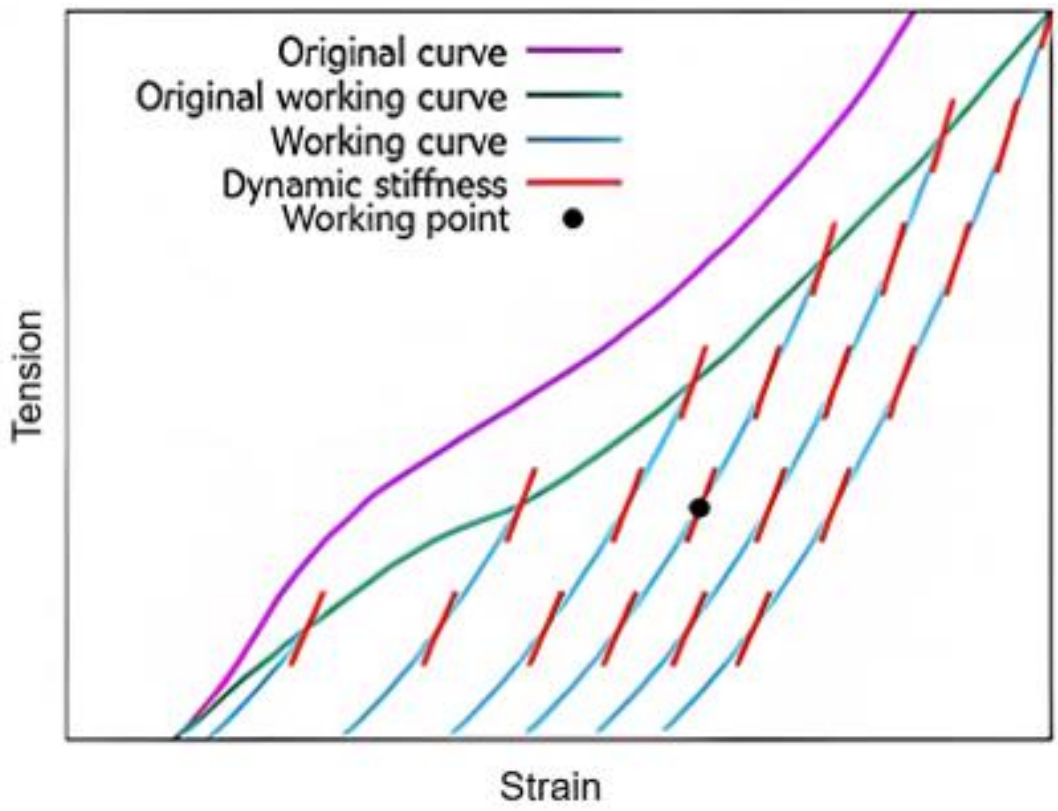

Figure 4.5: The Syrope model. Reproduced according to Falkenberg et al. (2017)

Original curve: generated for the test of a new rope subject to rapid loading in the initial bedding-in process. Not relevant for these studies.

Original working curve: generated for slowly applied tension above the historically maximum mean tension and adds more permanent strain in the rope

Working curve: generated for slowly applied tension below the maximum mean tension. The curve is defined by the maximum mean tension. Can be considered as quasi-static stiffness due to the slowly applied loading

Dynamic stiffness: the dynamic stiffness of the rope is defined at a working point at which LF and WF responses happens. The working point is defined for a mean tension along a working curve which is dependent on the maximum mean tension.

The Syrope model is based on results from sub-rope testing of synthetic fibre ropes. Software such as SIMA can implement Syrope directly if test data representing

- original working curve,
- working curve,
- constants for linear dynamic stiffness,
- maximum mean tension,

for the specific rope are known. If test data is unavailable, a linearized Syrope model, as described in Chapters 5.3.2 and 6.4.2, can be used to estimate the working curves.

4.3 Environmental conditions

The turbulent wind fields are generated as a time series by TurbSim software using the wind spectrum and coherence model presented in Chapter 3.2.1 (Jonkman and Kilcher, 2012). Three-component wind speed vectors represent the generated wind time series at points in a two-dimensional vertical grid. The irregular wave conditions are described using the Jonswap spectrum (Hasselmann et al., 1973). The combinations of significant wave height and peak period used to describe the sea states are derived from the joint distribution model of waves and wind proposed by Johanessen et al. (2002)

$$f_{U_{10}h_s t_p}(\overline{U}_{10}, h_s, t_p) = f_{U_{10}}(\overline{U}_{10}) f_{h_s|U_{10}}(h_s|\overline{U}_{10}) f_{t_p|h_s,U_{10}}(t_p|h_s, \overline{U}_{10}) \tag{4.5}$$

where $\overline{U}_{10}$ is the 1-hour mean wind speed at 10 m height, h_s is the significant wave height and t_p is the peak period. The following equation determines the expected h_s

$$E(h_S) = \beta\Gamma\left(\frac{1}{\alpha} + 1\right) \tag{4.6}$$

where the shape parameter α and scale parameter β are given by

$$\begin{aligned} \alpha &= 2 + 0.135\overline{U}_{10} \\ \beta &= 1.8 + 0.1\overline{U}_{10}^{\,1.322} \end{aligned} \tag{4.7}$$

The expected peak period can be found using the following equation

$$E(t_p) = \left(4.883 + 2.68{h_s}^{0.529}\right)\left[1 - 0.19\frac{\overline{U}_{10} - \left(1.764 + 3.426{h_s}^{0.78}\right)}{1.764 + 3.426{h_s}^{0.78}}\right] \quad (4.8)$$

4.4 Simulations

The coupled SIMO-RIFLEX software used in the SIMA workbench performs fully coupled time-domain simulations of STFC in operational conditions (SINTEF Ocean, 2022a and SINTEF Ocean, 2022b). The software solves the structural dynamic equilibrium in the time domain. It is assumed that 1-hour simulations can represent a fraction of a 3-6 hour simulation of an EC as specified by DNV OS-E301 and ST-0119 (2021b; 2021c). Coefficients for added mass, potential damping, first-order wave excitation loads, and mean drift loads are found through hydrodynamic analysis in the frequency domain using WADAM software (DNV, 2016). Conservation of fluid momentum in surge, sway and yaw is used to calculate mean drift loads. Slow-varying wave drift loads are considered for the supporting structure through full QTF. Viscous loads on the columns, pontoons, torus WEC and flap type WECs are calculated using Morison's equation and drag coefficients. The hydrodynamic coupling effects between CSC, torus WEC and flap type WECs are considered by including the coupled terms in the added mass and potential damping matrices. The added mass coefficient for five rigid bodies with 6 DOF can be written as (Lee et al., 2022)

$$\mathbf{A}(\omega) = \begin{bmatrix} \boldsymbol{a}^{1,1} & \dots & \boldsymbol{a}^{1,5} \\ \dots & \dots & \dots \\ \boldsymbol{a}^{5,1} & \dots & \boldsymbol{a}^{5,5} \end{bmatrix} \quad (4.9)$$

where $\boldsymbol{a}^{i,j}$ are 6 by 6 matrices, and the coupling terms $\boldsymbol{a}^{i,j}(i \neq j)$ represent the added mass on body i due to body j. The potential damping coefficient $\mathbf{B}(\omega)$ of five rigid bodies with 6 DOF can be represented similarly. A summary of mass, structural and external load models used for each component are given in Table 4.4.

Table 4.4: Numerical modelling methods for different components of STFC. Reproduced according to Lee et al. (2022)

Component	Mass model	Structural model	External load model
CSC semi-submersible	Integrated	Rigid body	- Gravity/buoyancy - First- and second-order wave excitation loads - Viscous forces
Wind turbine blade	Distributed	Beam element	- Gravity - Aerodynamic loads
Wind turbine tower	Distributed	Beam element	- Gravity - Aerodynamic loads
Wind turbine nacelle and hub	Integrated	Rigid body	- Gravity
Torus WEC	Integrated	Rigid body	- Gravity/buoyancy - First-order wave excitation loads - Mean drift forces - Viscous forces
Flap type WEC	Integrated	Rigid body	- Gravity/buoyancy - First-order wave excitation loads - Mean drift forces
Supporting arm	Distributed	Beam element	- Gravity/buoyancy - Morison wave loads
Mooring line	Distributed	Bar element	- Gravity/buoyancy - Morison wave loads

References

DNV. (2016). HydroD :: Sesam module HydroD.

DNV. (2021a). DNV-RP-E305: Design, testing and analysis of offshore fibre ropes.

DNV. (2021b). DNV-OS-E301: Position mooring.

DNV. (2021c). DNV-ST-0119: Floating wind turbine structures.

Falkenberg, E., Åhjem, V., & Yang, L. (2017). Best practice for analysis of Polyester rope mooring systems. Offshore Technology Conference, Houston, Texas, USA.

Hasselmann, K., Barnett, T. P., Bouws, E., Carlson, H., Cartwright, D. E., Enke, K., Ewing, J. A., Gienapp, A., Hasselmann, D. E., & Kruseman, P. (1973). Measurements of wind-wave growth and swell decay during the Joint North Sea Wave Project (JONSWAP). Ergaenzungsheft zur Deutschen Hydrographischen Zeitschrift. Reihe A. Nr. 122

Johannessen, K., Meling, T. S., & Haver, S. (2002). Joint distribution for wind and waves in the northern North Sea. International Journal of Offshore and Polar Engineering, 12(2).

Jonkman, B. J., & Kilcher, L. (2012). TurbSim user's guide: version 1.06.00. National Renewable Energy Laboratory, Golden, CO, USA.

Jonkman, J., Butterfield, S., Musial, W., & Scott, G. (2009). Definition of a 5-MW reference wind turbine for offshore system development (No. NREL/TP-500-38060). National Renewable Energy Lab (NREL), Golden, CO, USA.

Lee, C. F., Tryfonidis, C., & Ong, M. C. (2022). Power performance and response analysis of a semi-submersible wind turbine combined with flap-type and torus wave energy converters. Journal of Offshore Mechanics and Arctic Engineering, 145(4), 042001.

Morison, J. R., Johnson, J. W., & Schaaf, S. A. (1950). The force exerted by surface waves on piles. Journal of Petroleum Technology, 2(05), 149-154.

SINTEF Ocean. (2022a). RIFLEX :: SIMA documentation. https://sima.sintef.no/doc/4.4.0/riflex/index.html

SINTEF Ocean. (2022b). SIMO :: SIMA documentation. https://sima.sintef.no/doc/4.4.0/simo/index.html

Tryfonidis, C. (2022). Power Performance and Response Analysis of a Semi-Submersible Wind Turbine Combined with Wave Energy Converters in Intermediate and Deep Water (Master's thesis). University of Stavanger (UiS).

Chapter 5 -

Design and comparative analysis of mooring systems for a combined wind and wave energy system in intermediate water depth

Sindre Fjermedal[a], Chern Fong Lee[a*], Muk Chen Ong[a]

[a] Department of Mechanical and Structural Engineering and Materials Science, University of Stavanger, Kjell Arholms gate 41, 4021 Stavanger, Norway

The content of this chapter is under review in Marine Structures.

Abstract

For intermediate water depths (typically ranging from 50 m to 80 m), the design of steel catenary mooring systems can be challenging due to the low suspended catenary weight. In comparison, the use of synthetic fibre rope offers the possibility to prevent large floater movements while reducing peak mooring line tensions. In the present study, hybrid mooring systems targeted at a water depth of 50 m are proposed, featuring the use of polyester rope in combination with steel chains. Each hybrid mooring line consists of a top chain segment, an intermediate polyester rope segment, a buoy, and a bottom chain segment which connects to a drag-embedment anchor (DEA). The semi-submersible flap torus combination (STFC) concept, which integrates a torus wave energy converter (WEC), three flap type WECs, and a 5 MW NREL reference wind turbine, is chosen as the candidate floater for the study. Fully coupled time-domain simulations are carried out under aligned wind and wave loadings. A simplified "Syrope" model is used to describe the non-linear tension-dependent stiffness characteristics of the polyester rope. The performances of the hybrid mooring systems are assessed in terms of the motion response characteristics of the moored floater and mooring line tensions. These performance parameters are compared against that of a pure chain-catenary mooring system and a pure-polyester taut mooring system deployed at the same water depth. Finally, a preliminary cost analysis is performed, and some design recommendations for mooring system designs in intermediate water depths are given.

Keywords: combined wind and wave energy system, floating offshore wind turbine, mooring system, intermediate waters, synthetic fibre rope, polyester rope, drag-embedment anchor

5.1 Introduction

Renewable energy sources are on track to become the world's primary source of electricity by 2025, overtaking coal as the primary source of electricity. The growth is partly driven by a forecasted doubling of wind energy capacity by 2027, with offshore wind capacity accounting for 20 % of this growth (IEA, 2022). Furthermore, a significant portion of the offshore wind capacity will be floating offshore wind turbines (FOWTs), which by 2050 is set to account for

15 % of the offshore wind capacity (DNV, 2023). Although less significant than offshore wind, wave energy is set to play a part in the global shift towards renewable energy sources. However, wave energy has several challenges ahead, primarily a high levelized cost of energy (LCOE) compared to other renewable energy sources (Aderinto & Li, 2018).

FOWTs have been installed at deep water sites building on the learnings from the Oil and Gas industry on moored structures. However, for a FOWT, installing at intermediate water depth sites may be beneficial. Easy customer access, reduced power cable length and better access to the service industry are benefits worth pursuing by installing at intermediate water depths. Nevertheless, a different mooring system is required at intermediate water depths due to the reduction in water depth, which affects the mooring system stiffness. As Xu et al. (2018) showed, a decrease in water depth increases the non-linear mooring line tension due to an increased mooring system stiffness. Catenary mooring systems are subject to this effect, hence an unfavourable mooring system in intermediate water (Xu et al., 2021). Compared to a catenary mooring system, the non-linear mooring line tension can be reduced using a taut synthetic fibre rope mooring system. Synthetic fibre ropes have been used as a cheap and reliable mooring material in the Oil and Gas industry since Petrobras introduced it in 1997 (Francois & Davies, 2000). However, it has yet to see widespread use in the offshore renewable sector. Weller et al. (2015) summarised offshore renewable systems where synthetic fibre ropes might be applicable. They concluded that FOWTs and WECs would likely use polyester or nylon ropes as mooring material. However, the complex behaviour of synthetic fibre ropes under the influence of wind turbine dynamics still needs to be fully understood before being used as a mooring material. Nevertheless, the Floatgen demo (2018) is the world's first FOWT using nylon as mooring material. Recent advances by Xu et al. (2021), Sørum et al. (2023a) and Sørum et al. (2023b) show promising results for both polyester and nylon ropes as mooring materials for FOWTs.

FOWTs and WECs have been installed as individual systems. However, the spatial correlation between wind and waves is beneficial for integrating a FOWT and WEC into a combined system to capture energy. The benefits of combined devices are the co-sharing of supporting structures, power cables, mooring systems, and seabed area, which is expected to reduce the

LCOE from offshore renewable systems (Exceedence Ltd, 2022). For example, in both FOWT and WEC, the mooring system significantly contributes to cost, accounting for 40 % and 30 % of the cost, respectively (DNV, 2023; Martinelli et al., 2012). Therefore, a significant cost reduction is expected if the mooring system is co-shared. Although not commercial, several combined wind and wave energy systems are in development, such as FlexiFloat, Poseidon Wave & Wind, W2Power and STFC (FlexiFloat, 2021; McTiernan et al., 2020; Legaz et al., 2022; Lee et al., 2022). Nevertheless, combined wind and wave energy systems still face challenges such as complex dynamic behaviour and low power output from the WECs than the wind turbine (McTiernan et al., 2020).

This study proposes the mooring system for STFC deployed at a water depth of 50 m. Each mooring line consists of a top chain segment, an intermediate synthetic fibre rope segment, and a bottom chain segment connected to a DEA. In addition, the proposed mooring system includes a buoy at the connection between the bottom chain segment and the synthetic fibre rope. The mooring system is analysed with bottom chain segment lengths of 200 m, 300 m, and 400 m at 1633 kN and 1000 kN pre-tension in STFC operational wind and wave environment using fully coupled time-domain simulations.

5.2 Description

5.2.1 STFC

The combined wind and wave energy system, STFC (Lee et al., 2022) integrates a 5 MW NREL reference wind turbine (Jonkman et al., 2009), a torus WEC and three flap type WECs supported by a CSC braceless semi-submersible hull (Luan et al., 2016). STFC is designed for 200 m water depth using a three-point wire cable catenary mooring system with a pre-tension of 1633 kN. The wind turbine is installed on the centre column of the semi-submersible hull. Three side columns are connected to the centre column via pontoons, providing the restoring forces of the semi-submersible hull. The braceless design of the semi-submersible hull provides the necessary space to install flap type WECs. Energy is extracted by utilising the oscillating motion of waves to drive a generator. The torus WEC is a buoy which is installed through the

centre column. Energy is extracted by utilising the relative heave motion between the semi-submersible hull and torus WEC to drive a generator. STFC is visualised in Figure 5.1, and its properties are summarised in Table 5.1.

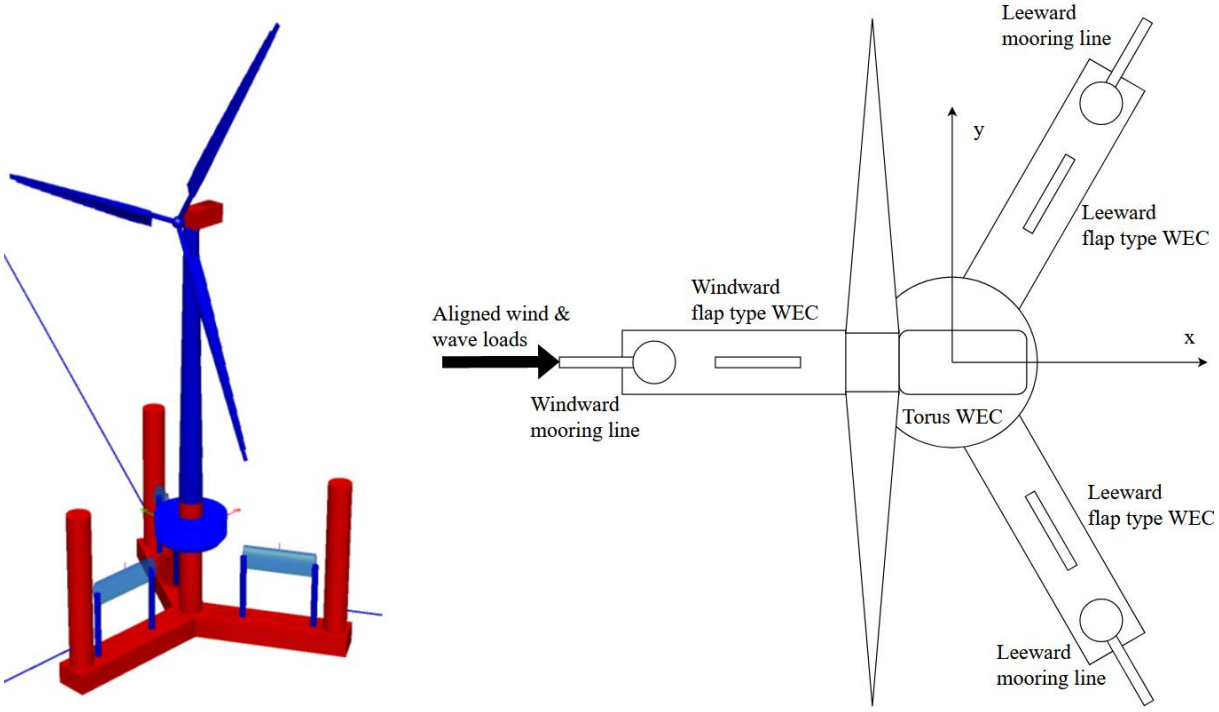

Figure 5.1: Visualisation of STFC, 3D and top view

Table 5.1: Main properties of STFC

Property	Unit	Value
CSC semi-submersible		
Draft	m	30
Displacement	tonnes	10 500
Operational water depth	m	200
Single mooring line		
Mass per unit length	kg/m	115
Unstretched mooring line length	m	1073
Clump weight in water	tonnes	15
Distance of clump weight from the fairlead	m	240
Flap type WEC		
Dimension of an elliptic cylinder (length*width*height)	m	20*7*3.5
Displacement	tonnes	394
Mass	kg	100
Length of one supporting arm	m	18.5
Mass of one supporting arm	kg	33.08
Displacement of one support arm	tonnes	33.5
Torus WEC		
Outer diameter of torus	m	20
Inner diameter of torus	m	8
Draft	m	2
Displacement	tonnes	423.7

5.2.2 Design of mooring systems in intermediate water depth

Mooring systems are used to limit the motions of a floating platform in the horizontal plane by creating a restoring force when the platform is displaced. The governing equation for restoring force F in a mooring system can, in its simplest form, be described as

$$F = kx \tag{5.1}$$

where k is mooring line stiffness and x is platform displacement. The horizontal stiffness consists of two series-connected stiffness components

$$\frac{1}{k} = \frac{1}{k_g} + \frac{1}{k_e} \tag{5.2}$$

Horizontal, geometric, in-elastic stiffness, k_g, caused by the change of mooring line geometry due to floater motions and elastic stiffness, k_e, from the axial elongation of the mooring line due to in-line tension (Faltinsen, 1993)

$$k_g = \frac{dT_H}{dx} = w\left[\frac{-2}{\left(1+\frac{2T_H}{wh}\right)} + \cosh^{-1}\left(1+\frac{wh}{T_H}\right)\right]^{-1}$$
$$k_e = \frac{EA}{l}cos\alpha \tag{5.3}$$

where T_H is the horizontal mooring line tension, w is the unit weight of the mooring line, and h is the vertical height between the touch-down point and fairlead. E is Young's modulus, A is the cross-sectional area, l is the mooring line length and α is the angle between the mooring line and the horizontal plane. Given that T_H is constant, the geometric stiffness increase as h decrease and consequently, the mooring system is subject to higher tension responses, posing a challenge for geometric stiffness dominated catenary mooring systems in intermediate water. In order to reduce the geometric stiffness, either a long mooring line or heavier material can be used. However, both the length and mass of the mooring line directly increase the cost.

Another method to reduce the geometric stiffness in a catenary system is to introduce lighter material segments, such as synthetic fibre ropes with w close to zero. Given that T_H, h and material properties remain constant, the stiffness of a chain k_c is geometric stiffness and stiffness of a synthetic fibre rope k_s is elastic stiffness dominated. Therefore, the stiffness of a chain and synthetic fibre rope segment connected in series can be written as

$$\frac{1}{k} = \frac{1}{k_c} + \frac{1}{k_s} = \frac{1}{k_{gc}} + \frac{1}{k_{ec}} + \frac{1}{k_{gs}} + \frac{1}{k_{es}} \approx \frac{1}{k_{gc}} + \frac{1}{k_{es}} \tag{5.4}$$

The stiffness is then governed by whichever is the lowest of k_{gc} and k_{es}. The results indicate that a catenary shape close to the seabed with low h results in a high k_{gc} compared to k_{es}. As a consequence, the mooring system stiffness is governed by the elastic stiffness of the synthetic fibre rope.

5.2.3 Mooring configurationl

The standard for offshore moored structures by DNV OS-E301 (2021a) requires ultimate, fatigue and accidental limit state studies of the mooring system effect on the moored structure. In this study, the performance of STFC mooring systems is only evaluated in operational conditions for the wind turbine corresponding to a wind speed range of 0-25 m/s. The mooring designs are based on the following criteria:

- Tension in the mooring lines shall not exceed the MBL of mooring components
- Slack shall not occur in the mooring lines (T<0) as this condition may lead to large snap tension loads
- Synthetic fibre ropes shall not be in contact with the seabed and floater to avoid abrasion of the synthetic fibres (DNV RP-E305, 2021b)
- Mooring chains shall remain on the seabed between the synthetic fibre rope and the anchor to avoid complete chain lift-off from the seabed and vertical loads in the DEA

The present proposed hybrid mooring system is illustrated in Figure 5.2. It consists of a top chain segment, an intermediate synthetic fibre segment, a bottom chain segment and a DEA. A buoy is attached to the connecting point between the synthetic fibre rope and the bottom chain segment to reduce the risk of contact between the synthetic fibre rope and the seabed. A 50 m length top chain segment is used to keep the top of the polyester rope clear of the STFC hull. Three different lengths of the bottom chain segment are investigated.

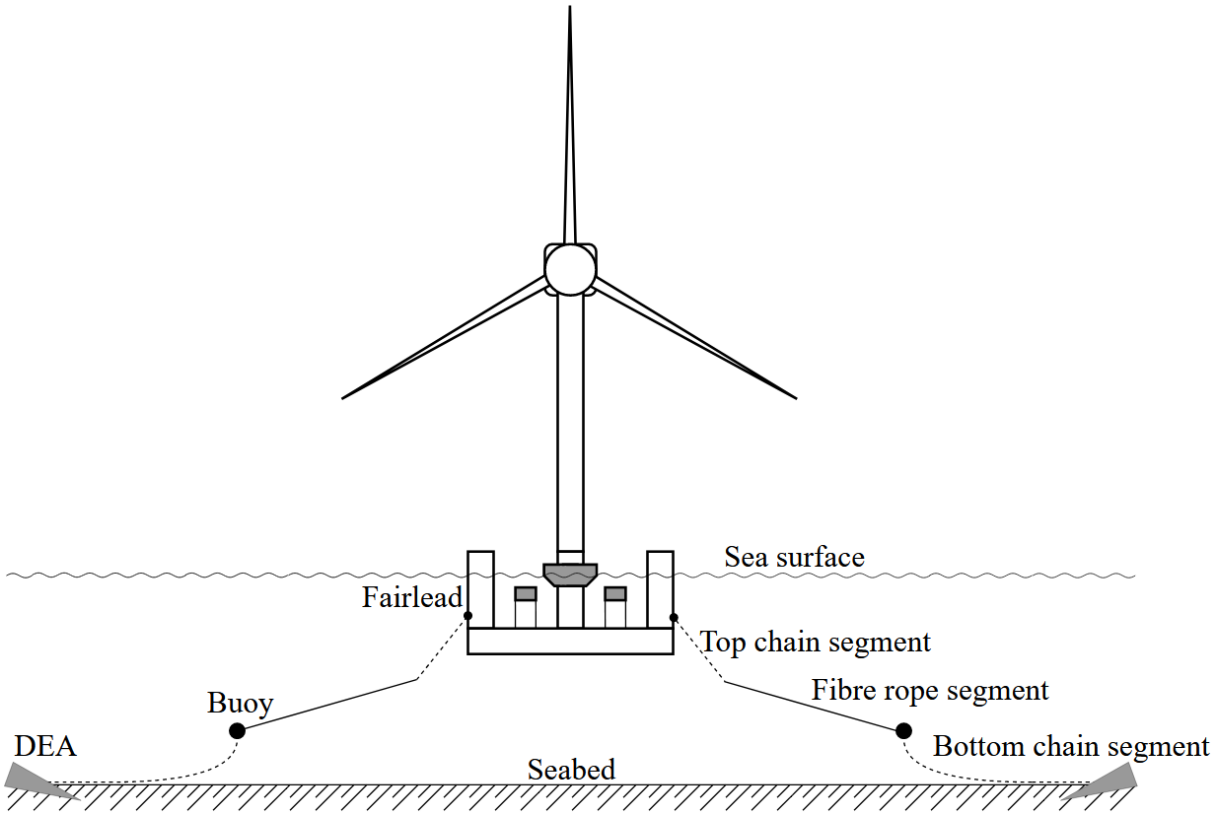

Figure 5.2: Proposed hybrid mooring system

In this study, two mooring line pre-tension values at a water depth of 50 m, one as STFC at a water depth of 200 m and another of 1000 kN, are investigated. In order to determine the anchor radius at 50 m water depth corresponding to a pre-tension equal to STFC at 200 m water depth, a taut mooring system with $L_i = 1000\,m$ is used. All mooring systems at 50 m water depth have the same anchor radius. The length of synthetic fibre rope in the hybrid mooring is determined by keeping the top and bottom chain segments constant, while the length of the synthetic fibre rope segment, L_i is updated iteratively until the desired pre-tension is achieved. The same principle of updating the mooring line length to achieve the desired pre-tension is used for the catenary system. Lastly, a second set of mooring systems at a pre-tension equal to 1000 kN is designed using the same process achieved by elongating the mooring lines due to the constant anchor radius and top and bottom chain segments. A design flowchart illustrating how the mooring systems are designed is shown in Figure 5.3.

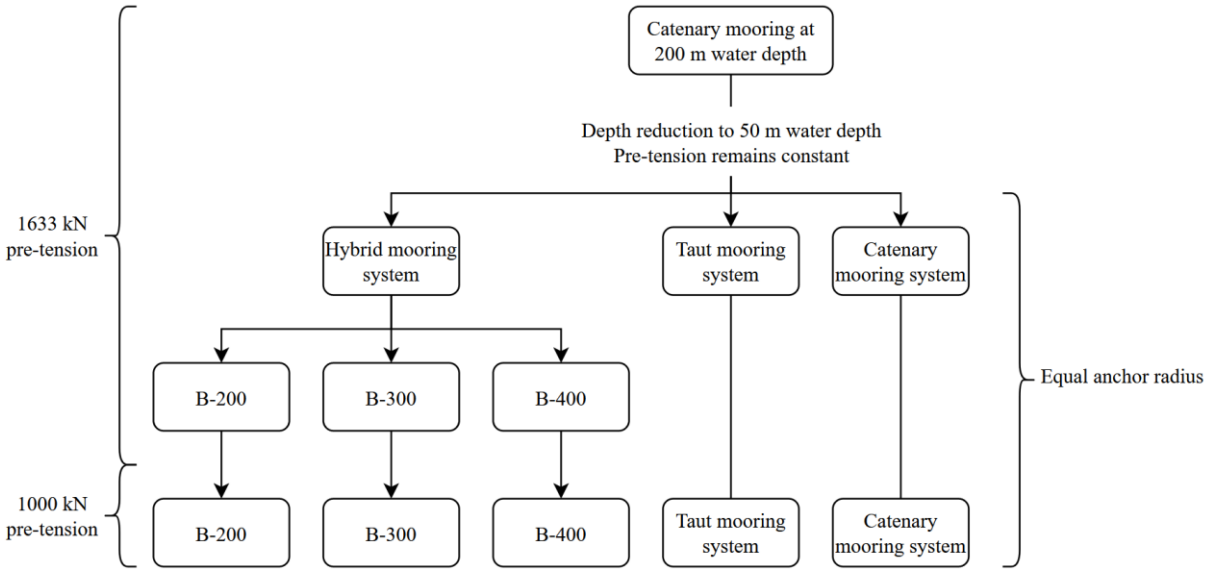

Figure 5.3: Mooring design flowchart

In this study, the synthetic fibre rope is a MoorLine polyester rope with reference to the catalogue of BRIDON-BEKAERT (2013). A buoy with net buoyancy of approximately 184 kN is required to keep the polyester rope 5 m above the seabed. A heavy chain is needed to prevent vertical loads in the anchor. The weakest link principle is applied, and the chain should have a similar minimum breaking load (MBL) as the polyester rope. Therefore, the chain used for both the top and bottom segments is an ORQ-grade stud chain with reference to the catalogue of Ramsäs (2012). The catenary mooring system uses the same chain as the hybrid mooring systems. The equivalent outer bar diameter and axial stiffness of the chain are estimated using the equations provided by Orcina (2023)

$$OD = 1.89d$$
$$EA = 1.01 * 10^8 d^2 \quad (5.5)$$

where d is the nominal diameter of the chain. The cross-sectional area is mass per meter divided by the density of steel (7850 kg/m^3). The hydrodynamic coefficients of polyester rope and chains are taken from DNV OS-E301 (2021a). The properties of the polyester rope and chain are given in Table 5.2.

Table 5.2: Properties of selected polyester rope and chain

	D (m)	m_{air} (kg/m)	m_{water} (kg/m)	A (m^2)	EA (MN)	MBL (kN)	C_{AL} (-)	C_{AN} (-)	C_{DL} (-)	C_{DN} (-)
Polyester rope	0.203	26.5	6.8	0.0192	Syrope	11772	-	1.0	-	1.6
Chain	0.130	370	180.8	0.047	1707	11932	0.5	1.0	1.15	2.4

* Subscript A is added mass, D is drag, L is longitudinal direction and N is normal direction of the mooring line

The angle between the sea surface and mooring line, α, is determined at pre-tension without environmental loads for all mooring systems. All mooring systems considered in this study are summarised in Table 5.3, displaying the properties of one single line. The O-STFC, catenary, and taut are conventional mooring systems, while the hybrid mooring systems are the B-X where B is a buoy, and X is the bottom chain segment length.

Table 5.3: Summary of all analysed mooring systems

System name	Pre-tension (kN)	Water depth (m)	Anchor radius (m)	Top segment length (m)	Clump (t)	Intermediate segment length (m)	Polyester rope length (m)	Buoy net buoyancy (kN)	Bottom segment length (m)	Total line length (m)	α (deg)
O-STFC	1633	200	1084.4	240	15	-	-	-	833	1073	30.1
Catenary	1633	50	1054.9	-	-	1013.5	1013.5	-	-	1013.5	20.0
Taut	1633	50	1054.9	-	-	-	1000.0	-	-	1000.0	3.0
B-200	1633	50	1054.9	50	-	-	752.8	184	200	1002.8	8.0
B-300	1633	50	1054.9	50	-	-	653.9	184	300	1003.9	8.1
B-400	1633	50	1054.9	50	-	-	555.0	184	400	1005.0	8.2
Catenary	1000	50	1054.9	-	-	1015.0	-	-	-	1015	24.9
Taut	1000	50	1054.9	-	-	-	1002.5	-	-	1002.5	3.7
B-200	1000	50	1054.9	50	-	-	755.1	184	200	1005.1	11.8
B-300	1000	50	1054.9	50	-	-	655.9	184	300	1005.9	11.5
B-400	1000	50	1054.9	50	-	-	556.8	184	400	1006.8	11.6

5.3 Numerical modelling

5.3.1 STFC

The nacelle, hub, semi-submersible hull, torus WEC and flap type WECs are modelled as 6 degrees of freedom (DOF) integrated mass rigid bodies. Hydrodynamic coefficients, first-order wave excitation loads, mean drift loads and hydrodynamic coupling effect between the wave-interacting rigid bodies is determined using frequency domain hydrodynamic analysis in WADAM (DNV, 2016). Slowly varying drift loads are only considered for the semi-submersible hull through the implementation of full quadratic transfer function (QTF). Viscous loads on submerged rigid bodies are accounted for as Morison drag forces.

The wind turbine blades, tower and supporting arms for the flap type WECs are modelled as distributed mass beam elements. The mooring lines are modelled as distributed mass bar elements. The buoys are modelled as nodal bodies with mass and volume. Morison's equation determines wave loads on supporting arms for flap type WEC and the mooring lines (Morison et al., 1950). The generator shaft of the wind turbine is composed of a flexible joint that separates a non-rotating and a rotating component. In order to comply with the control strategy described by Jonkman et al. (2009), generator torque is applied at the flexible joint. Linear rotational dampers model the power take off (PTO) damping of flap type WECs at the hinge joints. Conversely, the PTO damping of the torus WEC is modelled as a linear spring-dashpot.

In this study, six 1-hour simulations of an environmental conditions represent a simulation duration of 6 hours as specified by DNV OS-E301 and ST-0119 (2021a; 2021c), providing sufficient statistics to use in an initial assessment of the mooring system. Fully coupled time-domain simulations are performed using the coupled SIMO-RIFLEX software in SIMA workbench, which solves the structural dynamic equilibrium in the time domain (SINTEF Ocean, 2022a; SINTEF Ocean, 2022b)

$$\boldsymbol{R}^I(\boldsymbol{r},\ddot{\boldsymbol{r}},t) + \boldsymbol{R}^D(\boldsymbol{r},\dot{\boldsymbol{r}},t) + \boldsymbol{R}^S(\boldsymbol{r},t) = \boldsymbol{R}^E(\boldsymbol{r},\dot{\boldsymbol{r}},t) \tag{5.6}$$

where t is time, $\boldsymbol{R}^I$ is the inertia force vector, $\boldsymbol{R}^D$ is the damping force vector, $\boldsymbol{R}^S$ is the internal structural reaction force vector and $\boldsymbol{R}^E$ is the external force vector. $\boldsymbol{r}, \dot{\boldsymbol{r}}, \ddot{\boldsymbol{r}}$ are structural displacement, velocity, and acceleration vectors, respectively.

5.3.2 The Syrope model

The Syrope model proposed by Falkenberg et al. (2017) is used in this study to model the stiffness characteristics of synthetic fibre ropes. The model assumes that a synthetic fibre rope can be represented as an elastic and permanent stretch component using the spring-dashpot model shown in Figure 5.4 by Flory et al. (2007). The spring-dashpot model can be simplified by installing the synthetic fibre rope at a pre-tension equal to the expected maximum tension during its lifetime. The installation procedure prevents any further permanent stretching of the synthetic fibre rope after installation (Rowley & Leite, 2011). Visco-elastic stretch is a slow process representing change-in-length over time. Therefore, if a mechanism to adjust the length is introduced, this component can be neglected. Hence, a synthetic fibre rope in operation can be represented as a spring with stiffness derived from a tension-strain relationship.

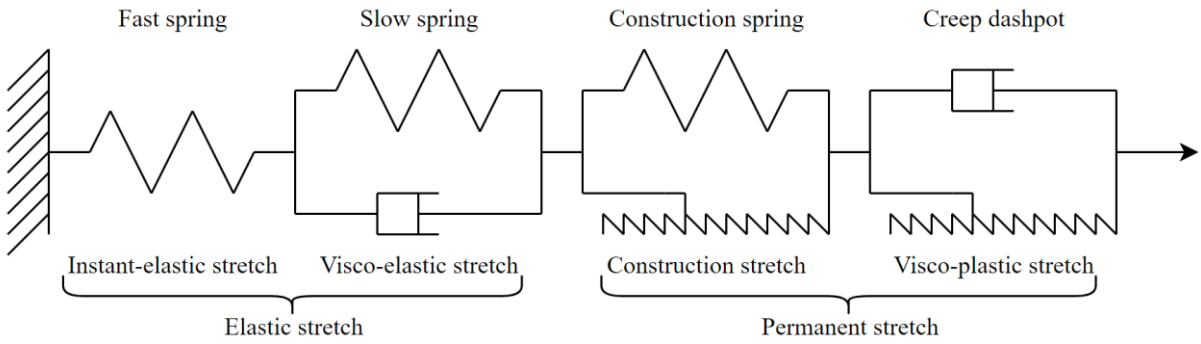

Figure 5.4: Spring-dashpot model of a synthetic fibre rope. Reproduced according to Falkenberg et al. (2017)

The Syrope model can be described using four curves: original curve, original working curve, working curve and dynamic stiffness. The original curve represents a new synthetic fibre rope

subject to rapid loading in the initial bedding-in process. The original working curve is generated when the synthetic fibre rope is subjected to slow loading above the historically maximum mean tension, $\overline{T}_{max}$, and more permanent stretch, ϵ_p, is added. For any tension value below $\overline{T}_{max}$ the load path follows a working curve. As the load is applied slowly, the stiffness of the rope along the working curves can be considered quasi-static stiffness. The dynamic stiffness curve is assumed linear as a function of mean tension at the working point. The Syrope model is presented in Figure 5.5, where stiffness is the tangent of the curves.

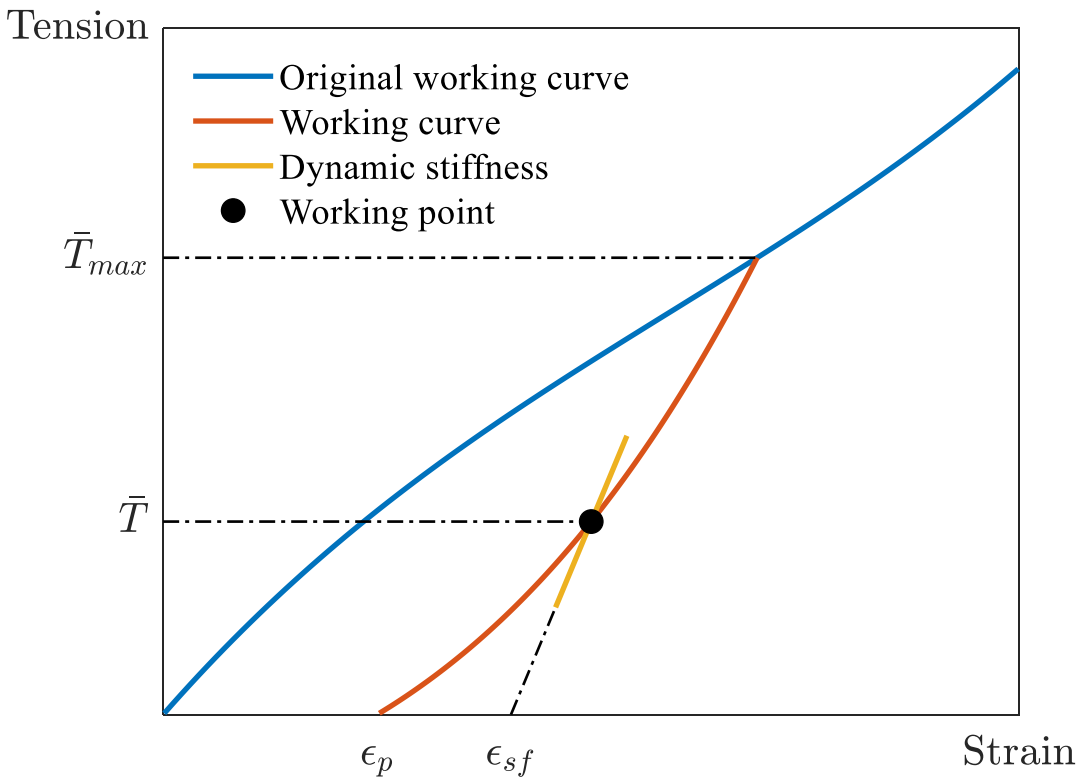

Figure 5.5: The Syrope model. Reproduced according to Falkenberg et al. (2017)

In practice, Syrope is implemented using tension-strain test data from sub-rope testing. In the present study, the Syrope model is employed in a simplified form due to the absence of test data. The simplified model assumes that tension in the mooring lines during operation is lower than the installation tension. Therefore, no further permanent and visco-elastic stretch of the synthetic fibre rope is expected. Thus, the working curves are fixed at a constant working point.

The slope of the working curve is the static stiffness and is seen to be non-linear. However, in this study, a linearised static stiffness dependent on $\bar{T}$ only is assumed (Stenlund, 2018; Tomren, 2022). The following expression represents the linearised static stiffness

$$\frac{d\bar{T}}{d\epsilon} = EA_s = (a\bar{T} + bMBL) \tag{5.7}$$

where ϵ is the rope strain, a and b are constants determined by sub-rope testing, and MBL is the minimum breaking load of the synthetic fibre rope. As shown by Sørum et al. (2023a), the dynamic stiffness can be assumed to be a linear function dependent on $\bar{T}$ only. Therefore, the following expression represents the dynamic stiffness

$$EA_D = c\bar{T} + dMBL \tag{5.8}$$

where c and d are constants determined by sub-rope testing.

Applying dynamic stiffness requires updating the mooring line mass and length to a stress-free state. At a stress-free state, there is no tension in the rope, and the following equation can represent the stress-free strain

$$\epsilon_{sf} = \epsilon_p - \frac{\bar{T}}{EA_d} \tag{5.9}$$

The permanent strain ϵ_p is found by calculating the strain in each line. The stress-free length is

$$L_{sf} = L_i + \epsilon_{sf} L_i \tag{5.10}$$

and the new mass per unit length is

$$m_{sf} = m_i \frac{L_i}{L_{sf}} \tag{5.11}$$

where L_i and m_i are the initial unstretched length and mass, respectively.

The procedure for implementing the simplified Syrope model is shown in Figure 5.6. Additional details regarding the procedure steps are as follows:

1. Determine sub-rope constants, the initial length of synthetic fibre rope and pre-tension. Anchor positions are determined by moving the anchor positions in a no-load condition until the previous $\bar{T}$ matches pre-tension
2. The applied mean environmental loads in operational conditions are assumed to be constant wind and irregular wave conditions. The windward and leeward mooring line stiffness is iteratively updated until the previous $\bar{T}$ matches the new $\bar{T}$
3. Strains in windward and leeward mooring lines are calculated and used to update the length and mass of the mooring lines before the application of dynamic stiffness
4. To validate the dynamic simulations, $\bar{T}$, using EA_s, L_i and m_i under mean environmental loads should equal $\bar{T}$ using EA_D with the updated L_{sf} and m_{sf} under dynamic loading

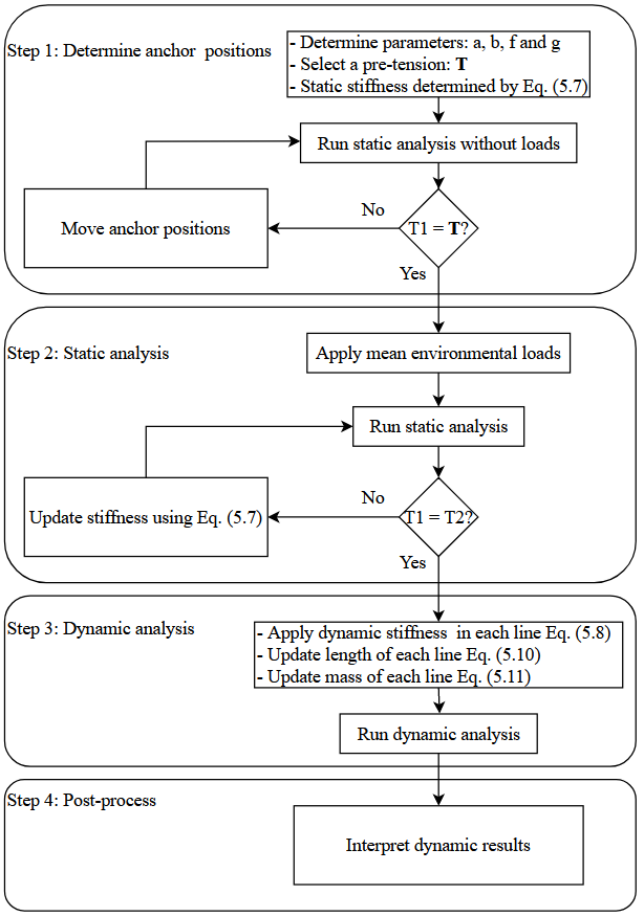

Figure 5.6: Procedure for implementing the Syrope model

5.3.3 Environmental conditions

Irregular wave conditions are described by significant wave height, h_s, and peak period, t_p, combinations using the Jonswap spectrum (Hasselmann et al., 1973). Turbulent wind conditions are generated using the software Turbsim (Jonkman et al., 2012), specified by mean wind speed at hub height, $\overline{U}$, and turbulence intensity, I. Wind and wave loads are assumed to be aligned along the positive x-axis, as illustrated in Figure 1. No current or marine growth is present. For each environmental condition (EC), the mean environmental loading condition is characterised by the corresponding constant wind and mean wave drift conditions. The ECs are according to the wave-wind correlation model by Johannesen et al. (2002). In the present study, 6 ECs spanning across the operational domain of STFC are investigated. The ECs are shown in Table 5.4.

Table 5.4: Environmental conditions

Condition	$\overline{U}$ (m/s)	I (-)	h_s (m)	t_p (s)	Seeds (-)	Duration (h)
EC1	5	0.224	2.10	9.74	6	1
EC2	10	0.157	2.88	9.98	6	1
EC3	14	0.138	3.62	10.29	6	1
EC4	18	0.127	4.44	10.66	6	1
EC5	22	0.121	5.32	11.06	6	1
EC6	25	0.117	6.02	11.38	6	1

5.4 Results and discussion

This section compares STFC in terms of mooring system restoring forces, system natural periods, motion responses and mooring line tensions. Finally, a preliminary cost analysis and design recommendations for the mooring systems in intermediate water depths are given.

5.4.1 System restoring force

The system restoring force describes the force-offset relation in surge and sway of STFC in operational conditions. Results from the system restoring force tests are shown in Figure 5.7 and Figure 5.8 for mooring systems at 1633 kN and 1000 kN pre-tension, respectively. STFC at a water depth of 200 m is the least stiff mooring system with a 6.8 m surge offset at 800 kN. At 50 m water depth, the catenary mooring systems are the stiffest, while the taut mooring systems being the least stiff at 50 m water depth. A more significant reduction in stiffness is seen by reducing the pre-tension for the taut mooring system than the catenary mooring system. With a decreased pre-tension, the taut mooring systems are approaching the lower stiffness of the O-STFC. However, the leeward polyester ropes are in contact with the seabed at 1633 kN pre-tension. If the pre-tension is reduced, this issue is amplified. The hybrid mooring systems perform like the taut mooring systems, while the contact issue between the polyester rope and seabed is avoided. A slight trend in reduced stiffness is seen for the hybrid mooring systems as chains are replaced by polyester rope.

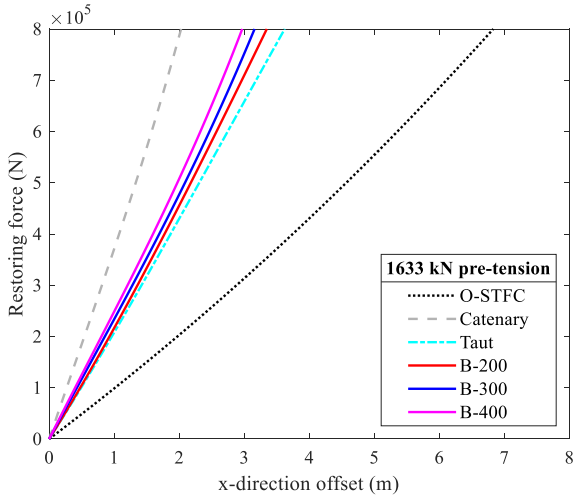

Figure 5.7: System restoring force of mooring systems at 1633 kN pre-tension

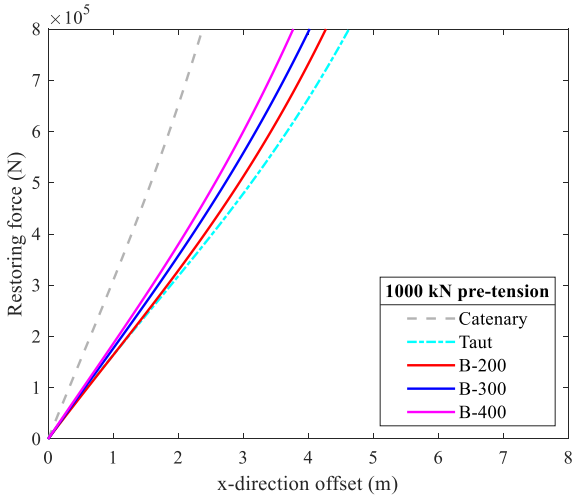

Figure 5.8: System restoring force of mooring systems at 1000 kN pre-tension

5.4.2 System natural periods

The system natural periods are determined through free decay tests in calm weather conditions. The mooring system will influence the horizontal plane motions of STFC and affect natural periods in surge, sway, and yaw. The remaining motions, heave, roll, and pitch, should have their natural periods relatively unaffected by the mooring system. The decay test is performed while the wind turbine is parked and the WECs are operational. Effects on natural periods due to the addition of WECs are measured using this configuration.

The results from the decay tests are shown in Figure 5.9. As expected, heave, roll and pitch natural periods remain largely unaffected by changes in the mooring system. The results show a significant decrease in surge and sway natural periods from 200 m to 50 m water depth due to increased mooring system stiffness with reduced water depth. For both pre-tensions, the catenary mooring system has the shortest surge and sway natural periods, whereas the taut mooring system has the longest. The hybrid mooring systems have natural periods between the catenary and the taut mooring systems. Shorter surge and sway natural periods are observed for the hybrid mooring systems if more chains are used or the pre-tension is increased. Yaw natural periods are relatively unaffected by water depth and mooring system. The yaw natural period seems only affected by the pre-tension, as a decrease in pre-tension increases the yaw natural period for all mooring systems.

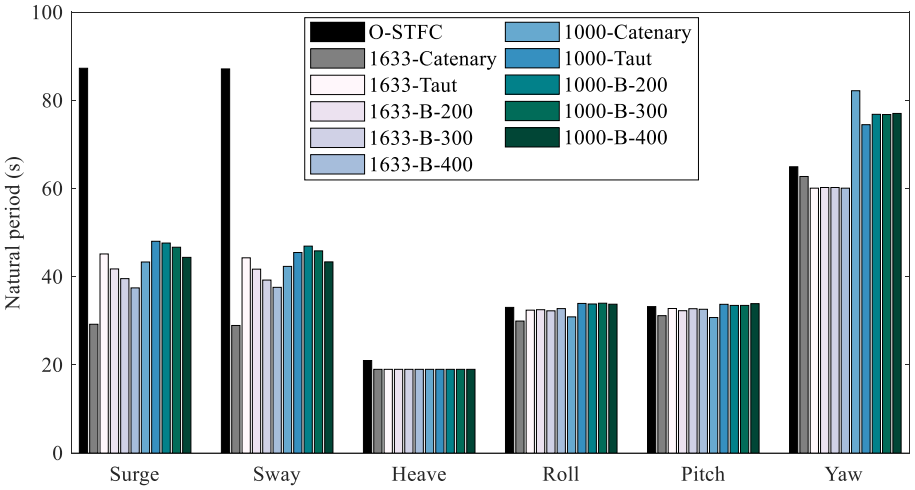

Figure 5.9: System natural periods

5.4.3 Motion responses

Motion responses are presented as the mean, standard deviation and maximum of surge, pitch, and yaw motions in irregular wave and turbulent wind conditions. The motion mean, standard deviation and maximum of an EC is averaged across 6 simulations.

The statistics of surge, pitch, and yaw motion at 1633 kN and 1000 kN pre-tension are shown in Figures 5.10 to 5.15. At 200 m water depth, a larger surge motion is seen compared to 50 m water depth due to the lower system restoring stiffness. The pitch motion is relatively unaffected by changes in water depth, whereas a slight decrease in yaw motion is seen with reduced water depth. At 50 m water depth, the mean, standard deviation, and maximum surge motion for catenary mooring systems are lower than the other mooring systems. The taut mooring system has the largest mean and maximum surge motion. The standard deviation of pitch and surge motion is seen to peak in EC3. Hybrid mooring systems are observed to behave similarly as compared to the taut mooring systems. However, a slight trend in decreased mean and maximum surge motion is seen as more chain is used in the hybrid mooring system.

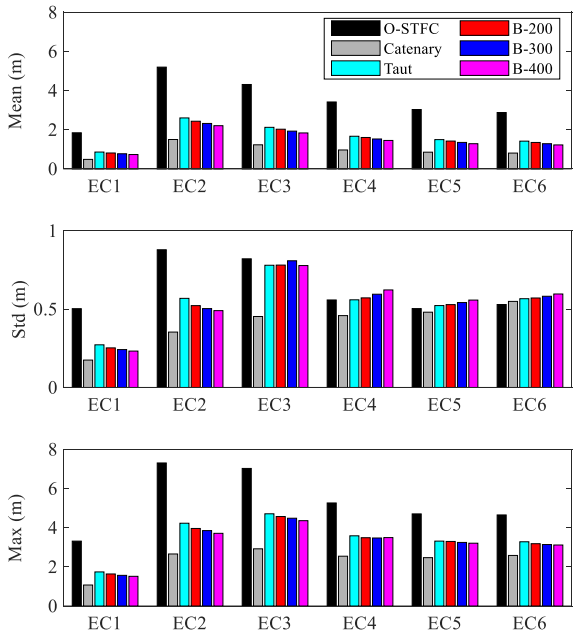

Figure 5.10: Surge motion responses at 1633 kN pre-tension

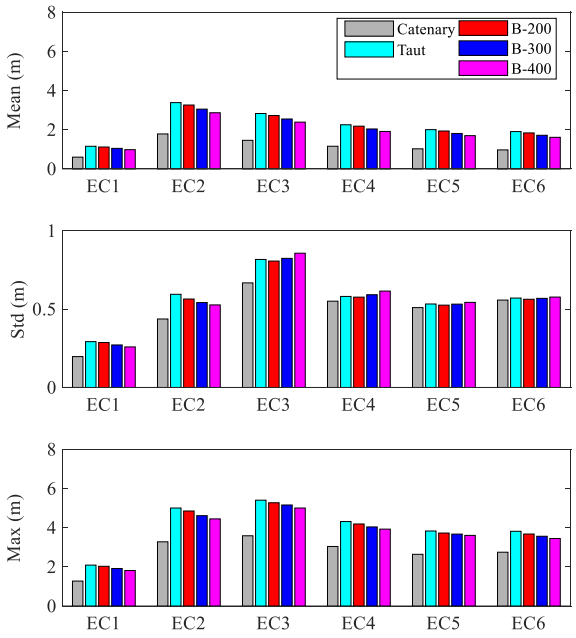

Figure 5.11: Surge motion responses at 1000 kN pre-tension

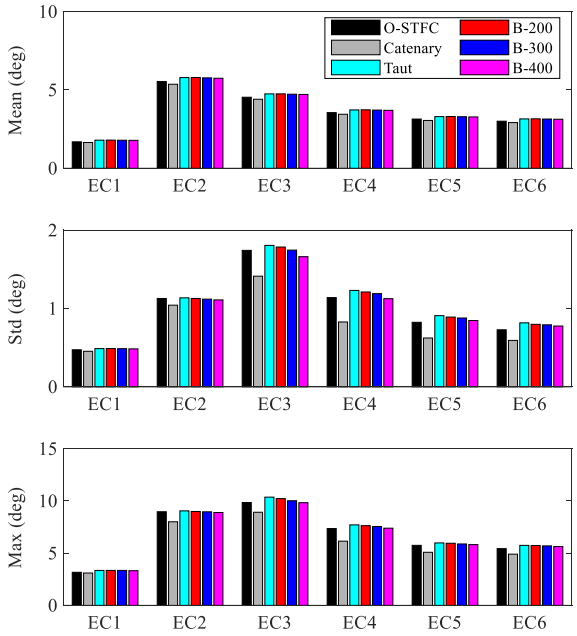

Figure 5.12: Pitch motion responses at 1633 kN pre-tension

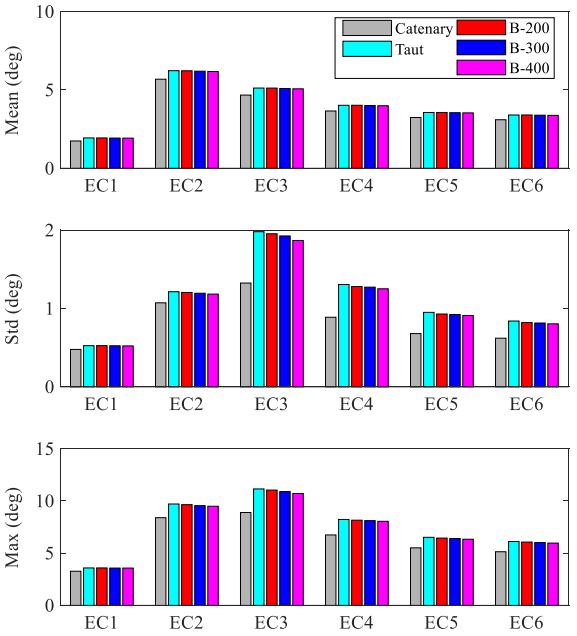

Figure 5.13: Pitch motion responses at 1000 kN pre-tension

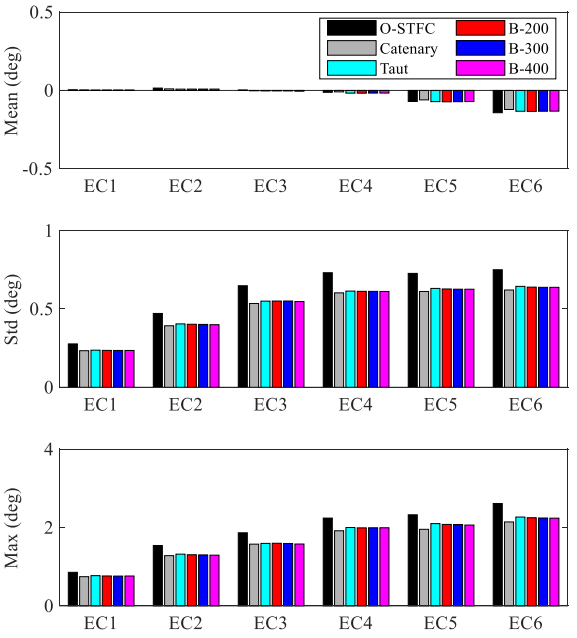

Figure 5.14: Yaw motion responses at 1633 kN pre-tension

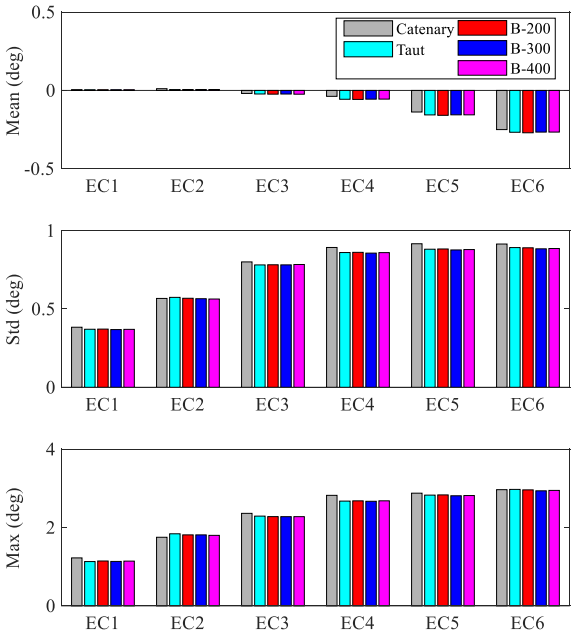

Figure 5.15: Yaw motion responses at 1000 kN pre-tension

Motion spectra for surge, pitch, and yaw in EC3 averaged across 6 simulations for pre-tensions of 1633 kN and 1000 kN are presented in Figures 5.16 to 5.21. It is observed that wave frequency (WF) responses in EC3 are not affecting pitch and yaw motions, whereas a minor WF response is seen for surge motion. The low frequency (LF) wind components are seen to dominate responses in operational conditions. At 200 m water depth, the standard deviation of surge motion is driven by both surge and pitch resonant responses, whereas at 50 m water depth, it is only driven by surge resonant response. The taut mooring system generally has the highest response in pitch, whereas the catenary mooring system has the lowest. The hybrid mooring systems are shown to have a decreasing response in pitch as more chain is used. Results indicate that mooring systems using synthetic fibre ropes as mooring material are more susceptible to pitch motion. The lower weight of synthetic fibre ropes provides a lower opposing moment to the thrust caused by the wind turbine than the heavier chains in catenary mooring systems. The standard deviation of yaw motion increases steadily, driven by yaw resonant responses. Response in yaw is unaffected by the mooring system and only dependent on pre-tension and water depth, as all mooring systems at the same pre-tension and water depth perform similarly.

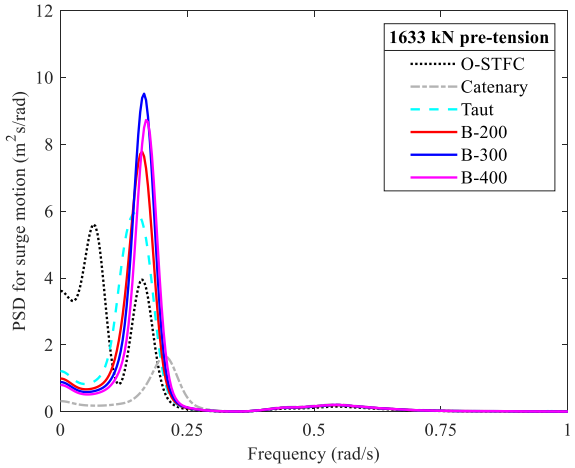

Figure 5.16: PSD for surge motion at 1633 kN pre-tension

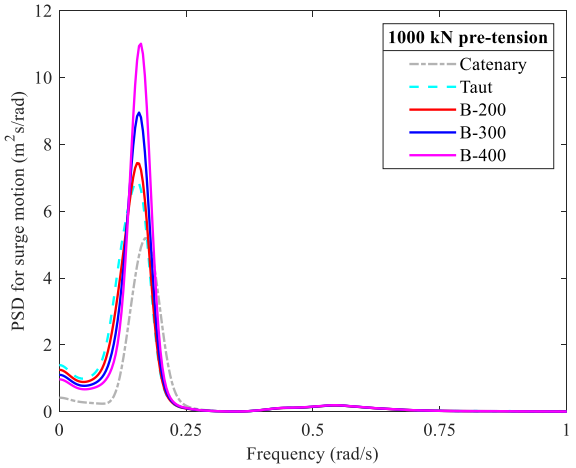

Figure 5.17: PSD for surge motion at 1000 kN pre-tension

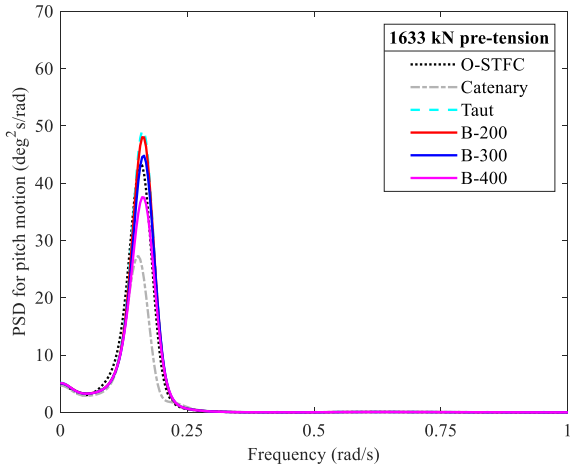

Figure 5.18: PSD for pitch motion at 1633 kN pre-tension

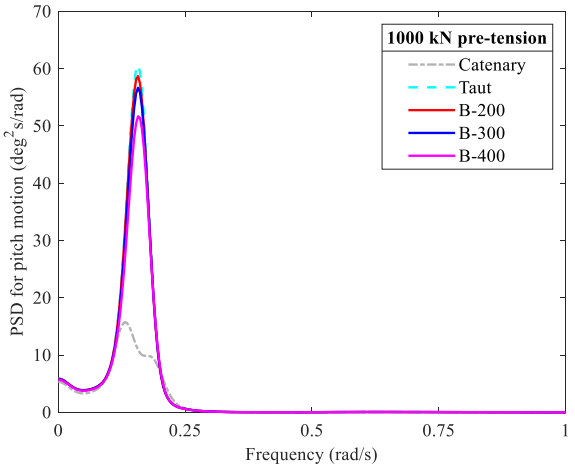

Figure 5.19: PSD for pitch motion at 1000 kN pre-tension

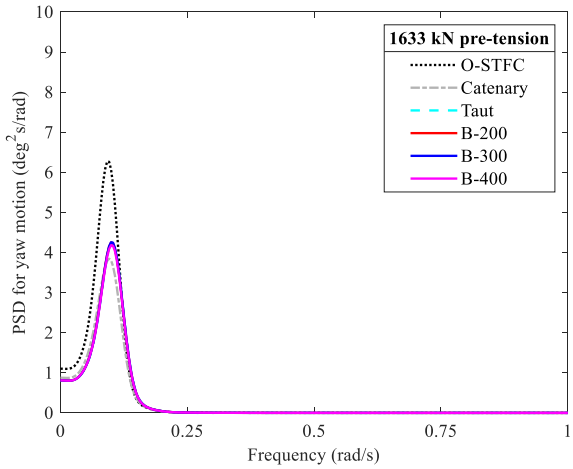

Figure 5.20: PSD for yaw motion at 1633 kN pre-tension

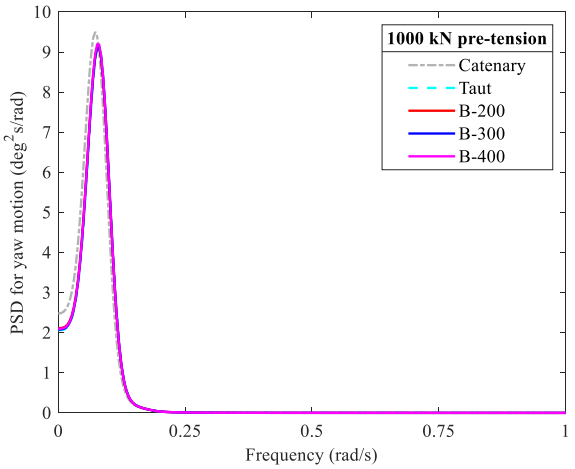

Figure 5.21: PSD for yaw motion at 1000 kN pre-tension

The hybrid mooring systems are assessed regarding chain lift-off and contact between seabed and fibre ropes. The seabed is modelled as flat without friction. Therefore, the results can be considered conservative. The windward mooring line and one of the leeward mooring lines of the hybrid mooring systems are visualised as a snapshot of the catenary plane at the maximum surge offset in EC3. The visualisation includes the initial configuration at pre-tension to illustrate the expected range of motion for the mooring lines. Snapshots are shown in Figure 5.22 and Figure 5.23 for 1633 kN pre-tension, and Figure 5.24 and Figure 5.25 for 1000 kN pre-tension. In all hybrid mooring systems, the windward mooring lines show no signs of lifting

the bottom chain segment. A 5 m clearance between the seabed and the polyester rope is seen in all hybrid mooring systems. There is a greater sag in the leeward lines at 1000 kN pre-tension. However, not an issue as the mooring line is not slack (T > 0), and the polyester rope is clear of the seabed.

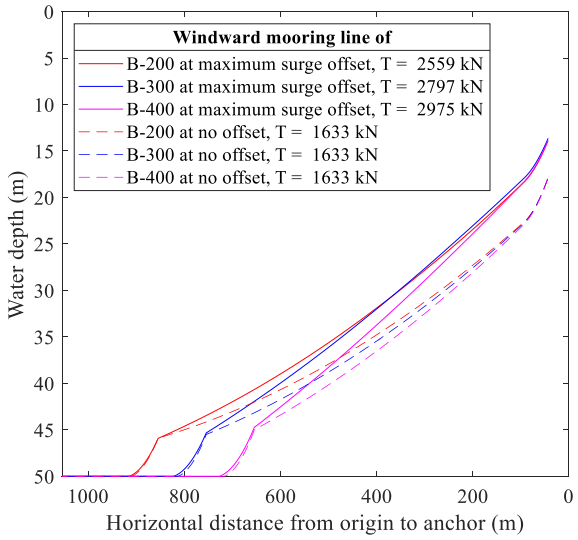

Figure 5.22: EC3 snapshot of the windward mooring line in hybrid mooring systems at 1633 kN pre-tension

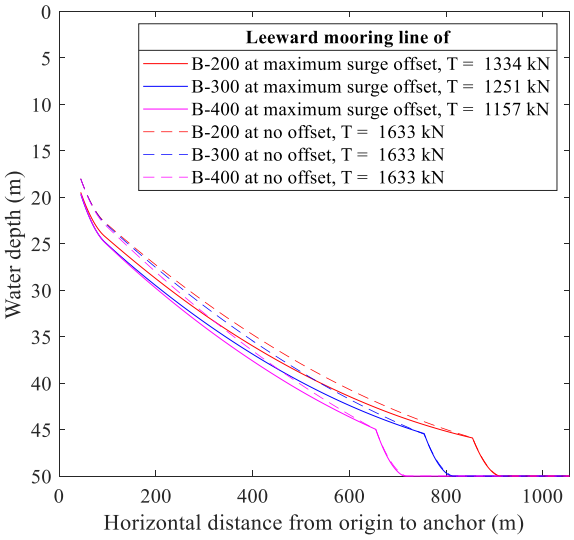

Figure 5.23: EC3 snapshot of a leeward mooring line in hybrid mooring systems at 1633 kN pre-tension

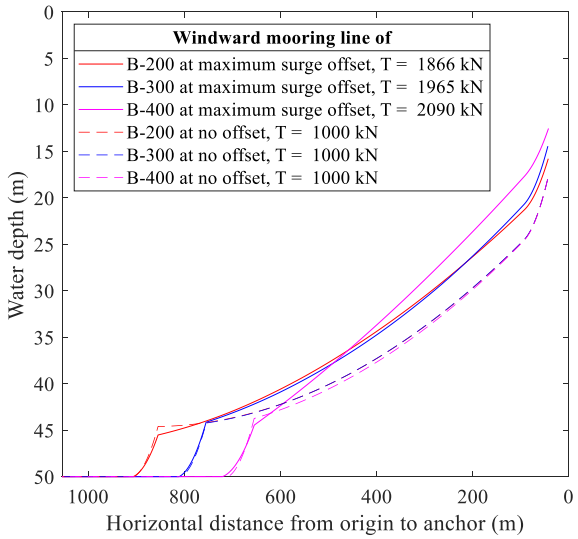

Figure 5.24: EC3 snapshot of the windward mooring line in hybrid mooring systems at 1000 kN pre-tension

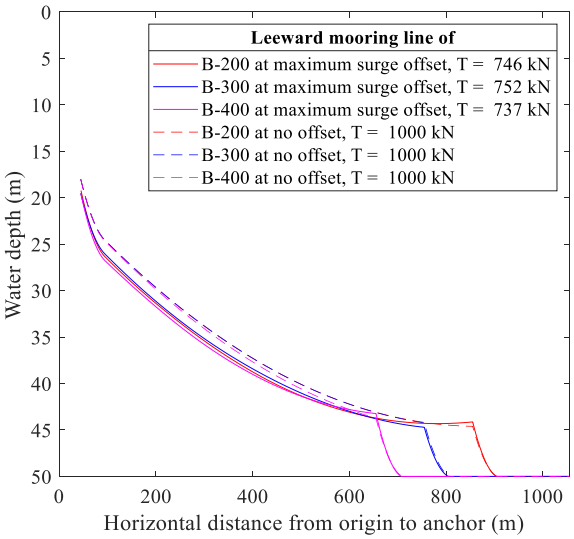

Figure 5.25: EC3 snapshot of a leeward mooring line in hybrid mooring systems at 1000 kN pre-tension

The remaining chain on the seabed is a function of tension induced by motions of STFC. In operational conditions, surge motion is a function of wind speed and the largest contributor to mooring tension. Therefore, the remaining chain on the seabed is assessed considering surge motion only. Samples of the remaining chain at a given surge offset are taken at time steps of 10 seconds for the 1 hr dynamic ECs 1-6. In total, 12960 samples for each windward mooring line. The results are shown in Figure 5.26 and Figure 5.27 for a pre-tension of 1633 kN and 1000 kN, respectively. The relationship between surge offset and the remaining chain can be estimated as linear. Therefore, a linear fit is introduced to extrapolate the required surge offset for complete chain lift-off. In the systems at 1633 kN pre-tension, a greater chain length is lifted than the 1000 kN pre-tension hybrid mooring systems when given the same offset. Results indicate that the remaining chain on the seabed is expected to follow the linear trend as more simulations of STFC in operational conditions are realised.

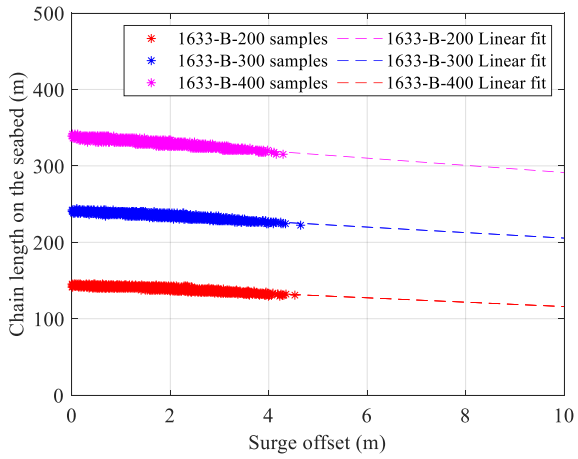

Figure 5.26: Chain length on the seabed vs STFC surge offset at 1633 kN pre-tension

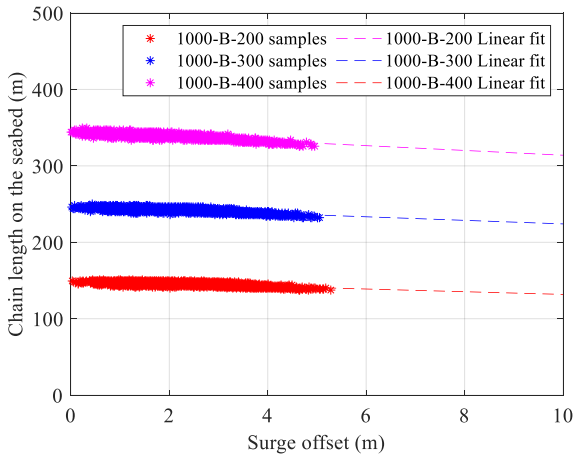

Figure 5.27: Chain length on the seabed vs STFC surge offset at 1000 kN pre-tension

The windward mooring line of the hybrid mooring systems is considered in static and dynamic conditions to evaluate dynamic effects on chain lift-off. The static condition uses mean environmental loads, whereas dynamic conditions are the same as described in the Environmental Conditions Section (Chapter 5.3.3). The least remaining chain is sampled at

peak surge offset. The peak surge offset is the maximum in the 6 seed ECs. Results are shown in Table 5.5 and Table 5.6 for 1633 kN and 1000 kN pre-tension, respectively. The largest percentage decrease in the remaining chain on the seabed is in the B-200 hybrid mooring system. The B-400 hybrid mooring system has the lowest percentage decrease. However, in terms of absolute chain length, more chain is lifted for the B-400 hybrid mooring system. The B-300 hybrid mooring system has characteristics between the B-200 and B-400 hybrid mooring systems.

Table 5.5: The effect of dynamic conditions on chain lift-off in hybrid mooring systems at 1633 kN pre-tension

	The chain on the seabed at			
1633-B-200	No offset (m)	Mean offset (m)	Peak offset (m)	Decrease between mean and peak (%)
EC1	144.1	142.8	138.8	2.88 %
EC2		137.3	129.5	5.99 %
EC3		138.8	128.2	8.30 %
EC4		140.2	132.2	6.04 %
EC5		140.1	133.5	4.98 %
EC6		140.1	133.5	4.97 %
1633-B-300				
EC1	240.2	238.2	234.3	1.70 %
EC2		232.3	224.3	3.55 %
EC3		234.3	222.3	5.37 %
EC4		236.3	226.3	4.40 %
EC5		236.3	228.3	3.49 %
EC6		236.3	228.3	3.48 %
1633-B-400				
EC1	336.3	333.7	331.0	0.81 %
EC2		328.4	317.8	3.34 %
EC3		328.8	309.9	6.12 %
EC4		331.0	317.8	4.17 %
EC5		331.0	320.4	3.30 %
EC6		332.8	317.8	4.72 %

Table 5.6: The effect of dynamic conditions on chain lift-off in hybrid mooring systems at 1000 kN pre-tension

	The chain on the seabed at			
1000-B-200	No offset (m)	Mean offset (m)	Peak offset (m)	Decrease between mean and peak (%)
EC1	149.4	148.1	144.1	2.78 %
EC2		142.8	137.5	3.87 %
EC3		144.1	136.1	5.86 %
EC4		145.4	140.1	3.81 %
EC5		145.4	138.7	4.82 %
EC6		146.8	136.1	7.85 %
1000-B-300				
1EC1	246.1	244.2	240.2	1.66 %
EC2		240.2	232.2	3.43 %
EC3		242.2	230.2	5.19 %
EC4		242.2	234.2	3.39 %
EC5		242.2	236.1	2.55 %
EC6		244.2	234.1	4.28 %
1000-B-400				
EC1	344.2	341.6	338.9	0.79 %
EC2		336.3	325.7	3.25 %
EC3		338.9	323.1	4.92 %
EC4		338.9	328.3	3.22 %
EC5		338.9	330.9	2.42 %
EC6		338.9	328.2	3.26 %

5.4.4 Mooring line tension

Statistics of mooring line tension are presented for the windward and one of the leeward mooring lines. Results are used to evaluate maximum tension against MBL for the windward mooring line and minimum tension against slack criteria (T<0) for the leeward mooring line. The tension mean, standard deviation, minimum and maximum of an EC are averaged across 6 simulations.

Results for the windward mooring line at 1633 kN and 1000 kN pre-tension are shown in Figure 5.28 and Figure 5.29, respectively. Mean tension is seen to be equal for all mooring systems in an EC given the same pre-tension. Tension standard deviation and maximum increase as more chains are used in the hybrid mooring system. The 1633 kN pre-tensioned hybrid mooring systems have a higher standard deviation than 1000 kN pre-tension.

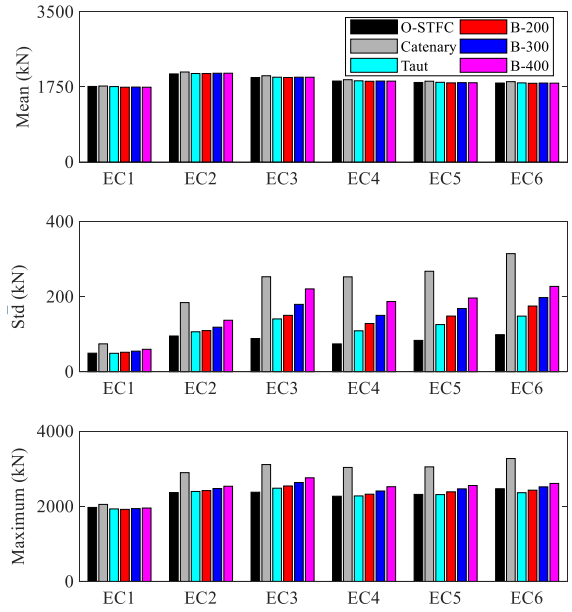

Figure 5.28: Tension responses in the windward mooring line at 1633 kN pre-tension

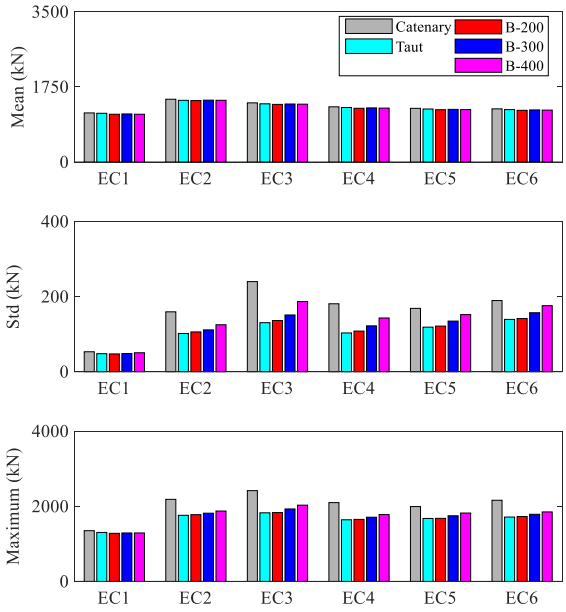

Figure 5.29: Tension responses in the windward mooring line at 1000 kN pre-tension

The recommended utilisation factor for mooring lines is given by DNV ST-0119 (DNV, 2021c). However, in this study, a simplified utilisation factor is presented as the ratio between the maximum tension and MBL

$$u = \frac{T_{max}}{MBL} \tag{5.12}$$

The resulting utilisation factors for all mooring systems are shown in Table 5.7. All mooring systems have maximum tension values well below the governing MBL.

Table 5.7: Maximum utilisation factor for mooring systems of STFC in operational conditions

Pre-tension (kN)	Catenary	Taut	B-200	B-300	B-400
1000	0.205	0.155	0.156	0.164	0.172
1633	0.264	0.211	0.216	0.224	0.234

Tension spectra for the windward mooring line in EC3 averaged across 6 simulations for pre-tension of 1633 kN and 1000 kN are presented in Figure 5.30 and Figure 5.31, respectively. The WF response is negligible at 200 m water depth, whereas there is a small WF response at 50 m water depth for both pre-tension levels. On the other hand, the LF wind components dominate in all mooring systems during operational conditions. At 200 m water depth, the LF tension response coincides with both surge and pitch resonant responses. However, at 50 m water depth, the tension response only coincides with the surge resonant response. Generally, the peak is lower, and the frequency at which the LF peak occurs is lower, given the same system at a lower pre-tension. The response in the B-200 and B-300 mooring systems is less than the taut mooring system, whereas the B-400 has a significant increase in response compared to the two other hybrid mooring systems. Results indicate that the hybrid mooring systems B-200 and B-300 are better suited for LF wind responses than a taut mooring system.

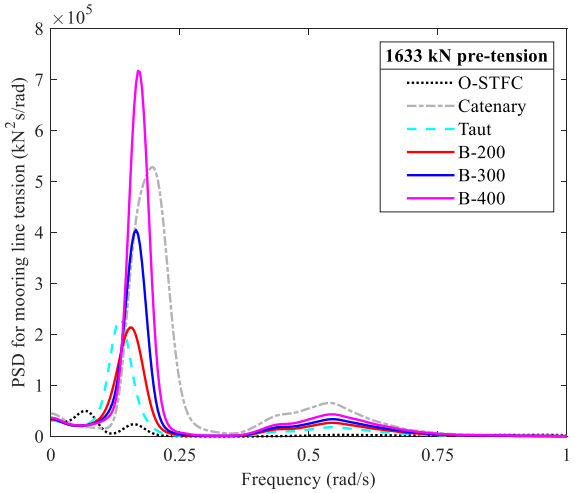

Figure 5.30: PSD for windward mooring line tension at 1633 kN pre-tension

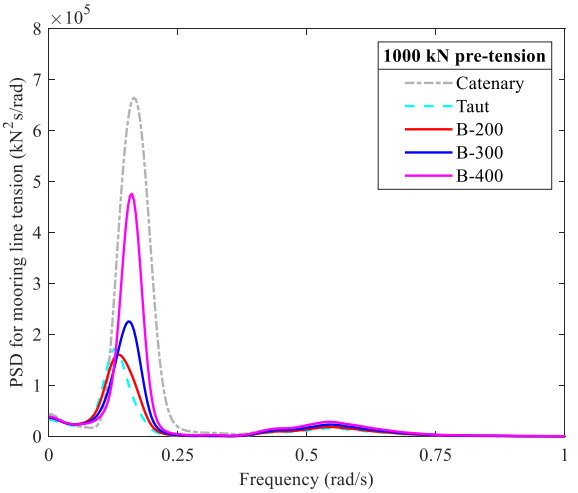

Figure 5.31: PSD for windward mooring line tension at 1000 kN pre-tension

Results for one of the leeward mooring lines at 1633 kN and 1000 kN pre-tension are shown in Figure 5.32 and Figure 5.33, respectively. Mean tension is seen to be equal for all mooring systems in an EC given the same pre-tension. Tension standard deviation increases and minimum decrease as more chains are used in the hybrid mooring system. All mooring systems have a minimum tension above 600 kN, and slack mooring lines are not expected.

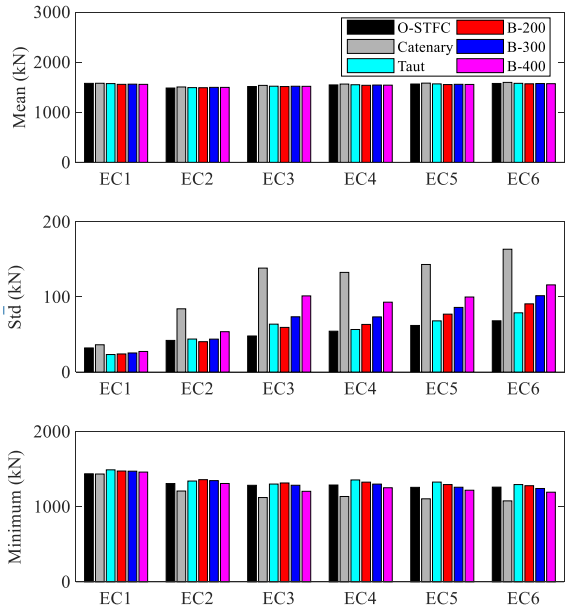

Figure 5.32: Tension responses in a leeward mooring line at 1633 kN pre-tension

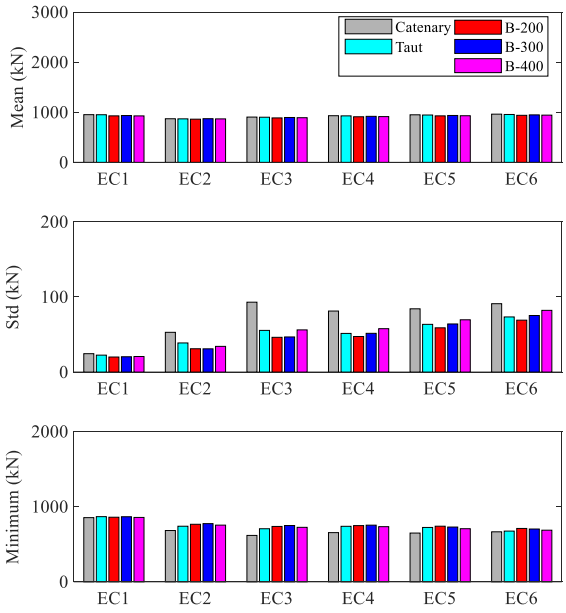

Figure 5.33: Tension responses in a leeward mooring line at 1000 kN pre-tension

5.4.5 Cost estimates

In this section, the mooring systems are evaluated in a cost analysis. There is no easily accessible data on the cost of mooring systems and their components. Therefore, the estimation is based on many assumptions and can only be used to indicate the mooring system cost. The procedure for cost estimation in this paper follows the one by Xu et al. (2021), except that the utilisation factor is not considered. The cost parameters for chain and fibre in €/kg are taken from Xu et al. (2021) and shown in Table 5.8. The buoy cost is estimated as a function of net buoyancy using a value of 2 €/kg (Marines, 2015). The cost of a DEA is 114 k€ with an installation cost of 55 k€, while a suction anchor (SA) has a cost of 512.5 k€ with an installation

cost of 88 k€ (Bjerkseter and Ågotnes, 2013). Due to the increased mooring line complexity, it is assumed that the hybrid mooring systems using DEA have the same installation cost as a SA. Maintenance, repair, and decommissioning costs are assumed equal for all mooring systems and can be omitted from the calculations. Therefore, the estimation considers only manufacturing and installation. The simple equation calculates the mooring line cost

$$cost = (price * length * mass + cost\ of\ components) * number\ of\ lines \quad (5.13)$$

where the price is given in €/kg, length is in m, mass is in kg/m, cost of components in €, and number of lines is the total number of equally designed mooring lines.

Table 5.8: Cost of steel chain and polyester rope

Material	Price (€/kg)
Steel chain	2.4525
Polyester rope	6.8670

A small variation in mooring line length is seen due to different pre-tension. However, the effect on the cost is negligible. Therefore, only cost estimates for the mooring systems with a pre-tension of 1633 kN are shown in Table 5.9. At 50 m water depth, the catenary mooring system is the most expensive. The catenary mooring system uses DEA, but the cost reduction is offset due to the heavy chain. Compared to the catenary, the taut mooring system results in a 29 % cost reduction. The cost reduction is due to replacing chains with polyester ropes. However, there is an increased cost because of using SAs. Compared to the catenary mooring system, the hybrid mooring systems B-200, B-300, and B-400 have a cost reduction of 50 %, 44 %, and 37 %, respectively. Therefore, even if an expensive chain is used, combining polyester ropes and DEA in the hybrid mooring systems significantly reduces costs compared to catenary and taut mooring systems.

Table 5.9: Estimated cost for mooring systems at 1633 kN pre-tension

	Catenary	Taut	B-200	B-300	B-400	Unit
Mooring lines	3	3	3	3	3	(-)
Chain length	1015	0	200	300	400	(m)
Chain mass	370	0	370	370	370	(kg/m)
Polyester rope length	0	1000	755.1	655.9	556.8	(m)
Polyester rope mass	0	26.5	26.5	26.5	26.5	(kg/m)
Buoy	0	0	24	24	24	(k€)
Anchor	114	512	114	114	114	(k€)
Installation	55	88	88	88	88	(k€)
Total cost	3.32	2.36	1.65	1.86	2.10	(M€)

5.4.6 Design recommendation

This section gives a design recommendation for the mooring system of STFC at intermediate water depth. A summary of the performances of the mooring systems is shown in Table 5.10.

In general, pre-tension is seen to be a balance between station-keeping capabilities and tension responses. Therefore, a lower or higher pre-tension can be used, depending on which characteristic is most favourable for the floating structure. In the case of STFC, pitch and yaw motions are unaffected, while an increased surge motion is seen for lower pre-tension. Nevertheless, the increased surge motion is not an issue if the power cable has an appropriate length to avoid high tension responses. Therefore, STFC could benefit from having a lower pre-tension.

The catenary mooring system for STFC is seen to be susceptible to large tensions and could risk chain lift-off causing the anchor to receive vertical loading. Additionally, the catenary mooring system is the most expensive. Therefore, the catenary mooring system is not recommended for further development. The taut mooring system is seen to have low tension responses and can resist vertical loading in the SA. However, the polyester rope is in contact

with the seabed, and the SA is a significant cost driver. Therefore, the taut mooring system is not recommended for further development in its current form. The hybrid mooring systems perform similarly to the taut mooring system. However, the contact issue between the polyester rope and the seabed is mitigated. Additionally, using DEAs reduces the mooring system cost well below the taut mooring system. None of the three hybrid mooring systems is seen to experience chain lift-off. However, this is subject to change in extreme conditions. All three B-200, B-300 and B-400 hybrid mooring systems show room for optimisation and are recommended for further development.

Table 5.10: Performance summary of mooring systems

System name	Pre-tension	$T_{max} > MBL$	$T_{min} < 0$	Polyester rope clear of the seabed	Anchor	Max surge response	Max pitch response	Max yaw response	Recommended for further development
	(N)	(y/n)	(y/n)	(y/n)	(SA/DEA)	(m)	(deg)	(deg)	(y/n)
Catenary	1633	n	n	-	DEA	2.9	8.9	2.1	n
Taut	1633	n	n	y	SA	4.7	10.4	2.3	n
B-200	1633	n	n	n	DEA	4.6	10.2	2.3	n
B-300	1633	n	n	n	DEA	4.5	10.0	2.2	n
B-400	1633	n	n	n	DEA	4.4	9.8	2.2	n
Catenary	1000	n	n	-	DEA	3.6	8.9	3.0	n
Taut	1000	n	n	y	SA	5.4	11.2	3.0	n
B-200	1000	n	n	n	DEA	5.3	11.0	3.0	y
B-300	1000	n	n	n	DEA	5.2	10.9	2.9	y
B-400	1000	n	n	n	DEA	5.0	10.7	3.0	y

5.5 Conclusion

Combined wind and wave energy systems can potentially help meet the world's growing demand for sustainable energy. However, several challenges regarding the design and cost need to be solved. One of these challenges is the mooring system, which affects both the design and cost. In an effort to reduce cost, a hybrid mooring system for the combined wind and wave energy system, STFC, at 50 m water depth is proposed. The hybrid mooring system consists of a top chain segment, an intermediate synthetic fibre rope segment, a buoy and a bottom chain

segment. The anchor radius is 1054.9 m, the top chain segment length is 50 m, and the length of the bottom chain segment is set to 200, 300 and 400 m while adjusting the synthetic fibre rope length to achieve sufficient pre-tension. The hybrid mooring systems are analysed at a pre-tension of 1633 kN and 1000 kN. Fully coupled time simulations are performed for STFC operational conditions. The hybrid mooring systems are studied regarding the system restoring force, system natural period, motion responses, mooring line tension and cost.

The hybrid mooring systems are measured against a catenary and a taut mooring system. The catenary mooring system is shown to be stiff and subject to high mooring line tension responses. The taut mooring system is shown to be compliant with a reduction in tension responses. The hybrid mooring systems are similar to the taut mooring system in system restoring force, system natural periods, motion responses, mooring line tension and cost. The cost analysis shows a significant cost reduction for the hybrid mooring systems compared to the catenary and taut mooring systems. As shown by the chain lift-off assessment, the hybrid mooring systems are very conservative in operational conditions, which indicates room for optimising the design. For example, reducing the anchor radius to reduce the mooring footprint, replacing more chains with synthetic fibre rope to reduce mooring system stiffness or decreasing the chain mass to reduce cost are possible optimisation options for the hybrid mooring systems. No contact between the synthetic fibre rope and the seabed is observed in operational conditions of STFC using the hybrid mooring systems. It is concluded that the proposed hybrid mooring system for STFC shows promising results. The cons of using a catenary or a taut mooring system are mitigated while most pros of those mooring systems are kept.

Future work should include connectors, an improved buoy model, marine growth, parametric studies on chains and synthetic fibre properties, ultimate limit state, accidental limit state and fatigue limit state studies. Finally, a parking solution for the torus WEC should be implemented.

Acknowledgements

The authors gratefully acknowledge the financial support through the Equinor Akademia program at the University of Stavanger.

References

Aderinto, T., & Li, H. (2018). Ocean wave energy converters: Status and challenges. Energies, 11(5), 1250.

Bjerkseter, C., & Ågotnes, A. (2013). Levelised costs of energy for offshore floating wind turbine concepts (Master's thesis, Norwegian University of Life Sciences, Ås).

BRIDON-BEKAERT. (2013). Catalogue: Advanced rope solutions for the offshore oil & gas exploration, construction and production industries.

DNV. (2016). HydroD :: Sesam module HydroD.

DNV. (2021a). DNV-RP-E305: Design, testing and analysis of offshore fibre ropes.

DNV. (2021b). DNV-OS-E301: Position mooring.

DNV. (2021c). DNV-ST-0119: Floating wind turbine structures.

DNV. (2023). Floating wind: Turning ambition into action. https://www.dnv.com/focus-areas/floating-offshore-wind/floating-wind-turning-ambition-into-action.html

Exceedence Ltd. (2022). LCOE Analysis for baseline project scenarios. European Scalable Offshore Renewable Energy Source (EU-Scores).

Falkenberg, E., Åhjem, V., & Yang, L. (2017). Best practice for analysis of Polyester rope mooring systems. Offshore Technology Conference, Houston, Texas, USA.

Faltinsen, O. (1993). Sea loads on ships and offshore structures (Vol. 1). Cambridge University Press.

FlexiFloat. (2021). Flexifloat – Flexible floating system. https://www.uis.no/nb/skaper-nye-losninger-havvind

Floatgen demo. (2018). France's first offshore wind turbine and BW ideol's first unit. https://www.bw-ideol.com/en/floatgen-demonstrator

Francois, M., & Davies, P. (2000). Fibre rope deep water mooring: a practical model for the analysis of polyester mooring systems. Rio Oil and Gas Expo and Conference, Rio de Janeiro, Brazil.

Flory, J. F., Anjem, V., & Banfield, S. J. (2007). A new method of testing for chang-in-length properties of large fiber-rope deepwater mooring. Proceedings of the Offshore Technology Conference, Houston, Texas, U.S.A.

Hasselmann, K., Barnett, T. P., Bouws, E., Carlson, H., Cartwright, D. E., Enke, K., Ewing, J. A., Gienapp, A., Hasselmann, D. E., & Kruseman, P. (1973). Measurements of wind-wave growth and swell decay during the Joint North Sea Wave Project (JONSWAP). Ergaenzungsheft zur Deutschen Hydrographischen Zeitschrift, Reihe A, Nr. 12.

IEA. (2022). Renewables 2022. IEA, Paris. https://www.iea.org/reports/renewables-2022

Johannessen, K., Meling, T. S., & Haver, S. (2002). Joint distribution for wind and waves in the northern North Sea. International Journal of Offshore and Polar Engineering, 12(2).

Jonkman, B. J., & Kilcher, L. (2012). TurbSim user's guide: version 1.06.00.

Jonkman, J., Butterfield, S., Musial, W., & Scott, G. (2009). Definition of a 5-MW reference wind turbine for offshore system development.

Lee, C. F., Tryfonidis, C., & Ong, M. C. (2022). Power performance and response analysis of a semi-submersible wind turbine combined with flap-type and torus wave energy converters. Journal of Offshore Mechanics and Arctic Engineering, 145(4), 042001.

Legaz, M. J., Coronil, D., Mayorga, P., & Fernández, J. (2018). Study of a Hybrid Renewable Energy Platform: W2Power. In Proceedings of the ASME 2018 37th International Conference on Ocean, Offshore and Arctic Engineering. Volume 11A: Honoring Symposium for Professor Carlos Guedes Soares on Marine Technology and Ocean Engineering. Madrid, Spain, V11AT12A040. ASME.

Luan, C., Gao, Z., & Moan, T. (2016). Design and analysis of a braceless steel 5-MW semi-submersible wind turbine. International Conference on Offshore Mechanics and Arctic Engineering, Busan, South Korea.

Marines, F. E. (2015). Deliverable 4.6: Framework for the prediction of the reliability, economic and environmental criteria and assessment methodologies for Moorings and Foundations.

Martinelli, L., Ruol, P., & Cortellazzo, G. (2012). On mooring design of wave energy converters: The Seabreath application. Coastal Engineering Proceedings, 1(33), structures.3.

McTiernan, K. L., & Sharman, K. T. (2020). Review of Hybrid Offshore Wind and Wave Energy Systems. In Journal of Physics: Conference Series (Vol. 1452, No. 1, p. 012016). IOP Publishing.

Morison, J. R., Johnson, J. W., & Schaaf, S. A. (1950). The force exerted by surface waves on piles. Journal of Petroleum Technology, 2(05), 149-154.

Muliawan, M. J., Karimirad, M., Moan, T., & Gao, Z. (2012). STC (Spar-Torus Combination): a combined spar-type floating wind turbine and large point absorber floating wave energy converter—promising and challenging. In International

Conference on Offshore Mechanics and Arctic Engineering (Vol. 44946, pp. 667-676). American Society of Mechanical Engineers.

Orcina. (2023). Orcina :: OrcaFlex documentation. https://www.orcina.com/webhelp/OrcaFlex/Content/html/Chain.html

Ramnäs. (2012). Catalogue: Top quality mooring products for harsh offshore conditions.

Rowley, D. S., & Leite, S. (2011). What if scenario testing of synthetic fibre rope for deepwater mooring systems. Proceedings of the Offshore Technology Conference, Rio de Janeiro, Brazil.

SINTEF Ocean. (2022a). RIFLEX :: SIMA documentation. https://sima.sintef.no/doc/4.4.0/riflex/index.html

SINTEF Ocean. (2022b). SIMO :: SIMA documentation. https://sima.sintef.no/doc/4.4.0/simo/index.html

Stenlund, T. (2018). Mooring system design for a large floating wind turbine in shallow water (Master's thesis). Norwegian University of Science and Technology (NTNU).

Sørum, S. H., Fonseca, N., Kent, M., & Faria, R. P. (2023a). Modelling of Synthetic Fibre Rope Mooring for Floating Offshore Wind Turbines. Journal of Marine Science and Engineering, 11(1), 193.

Sørum, S. H., Fonseca, N., Kent, M., & Faria, R. P. (2023b). Assessment of nylon versus polyester ropes for mooring of floating wind turbines. Ocean Engineering, 278, 114339.

Tomren, M. (2022). Design and Numerical Analysis of Mooring Systems for Floating Wind Turbines – Comparison of Concepts for European Waters (Master's thesis). Norwegian University of Science and Technology (NTNU).

Weber, J., Mouwen, F., Parish, A., & Robertson, D. (2009). Wavebob—research & development network and tools in the context of systems engineering.

Weller, S. D., Johanning, L., Davies, P., & Banfield, S. J. (2015). Synthetic mooring ropes for marine renewable energy applications. Renewable energy, 83, 1268-1278.

Xu, K., Gao, Z., & Moan, T. (2018). Effect of hydrodynamic load modelling on the response of floating wind turbines and its mooring system in small water depths. In Journal of Physics: Conference Series. IOP Publishing, 012006.

Xu, K., Larsen, K., Shao, Y., Zhang, M., Gao, Z., & Moan, T. (2021). Design and comparative analysis of alternative mooring systems for floating wind turbines in shallow water with emphasis on ultimate limit state design. Ocean Engineering, 219, 108377.

Chapter 6 -

Design and analysis of taut mooring systems for a floating offshore wind and wave energy system

Chern Fong Lee[a*], Sindre Fjermedal[a], Muk Chen Ong[a]

[a] Department of Mechanical and Structural Engineering and Materials Science, University of Stavanger, Kjell Arholms gate 41, 4021 Stavanger, Norway

The content of this chapter is under review in Ocean Engineering.

Abstract

Water depth is a crucial consideration when selecting the type of platform for developing an offshore renewable energy farm. The use of bottom-fixed substructures is economically limited to shallow water depths due to the excessive manufacturing costs. This leads to the technological shift to floating substructures as water depth increases. However, at intermediate (50-80 m) water depths, the design of conventional catenary mooring systems can be challenging due to reduced mooring compliance caused by decreased suspended mooring line weight. With an increased risk of being lifted-off the seabed during operation, steel mooring chains or cables would risk experiencing much higher peak loads as compared to mooring lines manufactured from relatively elastic materials. In response to this, the use of elastic materials such as synthetic fibre can be beneficial for mooring applications in intermediate water depths. In the present study, polyester-based taut mooring systems of a floating offshore combined wind and wave energy system designed for a water depth of 50 m are investigated. By maintaining the same system restoring stiffnesses in surge and sway, three mooring configurations with different anchor spacings, mooring line lengths, mooring line diameters and minimum breaking loads are modelled. The Syrope model is used to model the tension-stretch relationship of the polyester line. Coupled dynamic simulations are then carried out under aligned-wind and wave loadings to estimate the global responses of the floating system. The results are compared against an identical system deployed at 200 m water depth anchored by a steel catenary mooring system. Results are presented in terms of the statistics for platform global displacements, mooring line tensions, and the cost of mooring which provide an initial assessment of the performance of the mooring system designs in intermediate water depth.

Keywords: mooring system, synthetic fibre, taut mooring system, combined wind and wave energy system, floating offshore wind turbine, wave energy converter

6.1 Introduction

The United Nations (UN) Sustainable Development Goals (SDGs), particularly SDG 7 – Affordable and clean energy and SDG 13 – Climate action, emphasise the importance of renewable energy sources in achieving a cleaner and more sustainable future. Offshore renewable energy, which includes offshore wind, ocean energy, and solar energy, is set to play a vital role in meeting these goals. Offshore wind refers to energy generated from wind at sea; solar energy refers to photovoltaic activity at sea; ocean energy includes wave energy generated by the motion of ocean waves, tidal energy generated by the rise and fall of tides, and thermal energy generated by the temperature difference between the ocean surface and deep water. Over the past few decades, the offshore wind industry has experienced significant growth, reaching a total installed capacity of 35.3 GW by the end of 2020 (GWEC, 2021). In comparison, wave energy remains a relatively untapped source of offshore renewable energy, despite having the highest power density. For example, in regions with a solar isolation of 0.17 kW/m^2 at a latitude of 15° N, the available wind power intensity is estimated to be 0.58 kW/m^2, which could generate waves with an intensity of up to 8.42 kW/m^2 (McCormick, 1981). The lack of development for wave energy can be attributed to the inefficiency in converting the slow, irregular, and reciprocating motion of ocean waves at approximately 0.1 Hz into useful motion that drives a generator, usually running at 50 Hz. Survivability of offshore wave energy converters (WECs) is another challenge, particularly in areas with severe environmental conditions. As the devices' structures have to endure extreme loadings, it often results in excessive overdesign (Czech and Bauer, 2012).

As waves and wind are statistically correlated, offshore sites with significant wind energy may offer rich wave energy resources. The combined exploitation of wave and offshore wind energies can, therefore, simultaneously tap into both energy resources. Building on the technological maturity of the offshore wind industry, the integration of WECs onto the supporting structures of offshore wind turbines can potentially lead to significant cost reduction. A better utilisation of ocean space can be realised through the sharing of platforms, the sharing of facilities such as mooring systems and the sharing of power cables and substations.

To date, a variety of combined wind and wave energy concepts have been investigated. The EU-funded MARINA Platform project (Sojo and Auer, 2013) selected three combined wind and wave concepts for detailed examination. These concepts were the Spar-Torus-Combination (STC) (Muliawan et al., 2012), the Semi-submersible Flap Combination (SFC) (Luan et al., 2014) and the combination of an oscillating water column (OWC) array with a semi-submersible wind turbine (O'Sullivan, 2014). STC and SFC are among the concepts that have been extensively studied for their dynamic response characteristics under both operational and extreme environmental conditions (Muliawan et al., 2013a, Muliawan et al., 2013b, Michailides et al., 2014, Michailides et al., 2016). Gao et al. (2016) provided a comparison between the SFC and STC concepts and discovered that the contribution from wave energy systems amounts to less than 10% of the total energy production. Ren et al. (2018) proposed a hybrid structure consisting of a monopile type wind turbine and a heave-type WEC. Gkaraklova et al. (2021) studied the hydrodynamic behaviour and power absorption of a circular array with four heaving-type WECs around a hybrid wind–wave monopile in the frequency domain.

For the development of offshore renewable energy farms, the use of bottom-fixed offshore substructures is economically limited to shallow water depths due to the high platform manufacturing costs. While floating substructures are commonly used in deep waters, their adaptability to varying water depths also makes them cost-competitive options for intermediate water depths, typically ranging from 50-80 meters. For example, semi-submersibles are well-established substructures that are suitable for both intermediate- and deep-water deployments due to their characteristic low draft. However, mooring system designs for floating substructures at intermediate water depths can be challenging due to the reduction in water column, which decreases the suspended mooring line weight and results in a reduction of mooring compliance. Several researchers have investigated the design challenges for the mooring of floating renewable energy systems. Brommundt et al. (2012) developed a tool to optimise the catenary mooring systems of a semi-submersible floating offshore wind turbine (FOWT) deployed at two sites with 75 m and 330 m water depths, respectively. The results indicated that a more conservative design with a larger anchor radius is required in shallow water depths to prevent the occurrence of vertical loads on the drag-embedment anchors. Benassai et al. (2014) conducted a series of parametric studies on a moored semi-submersible

FOWT to investigate the effects of depth and allowable offset. With the same offset distance, depth reduction leads to a significant increase in mooring line weight. Qiao et al. (2020) investigated the occurrence of snap load on mooring lines and discovered that snap load can be avoided through increasing pre-tension, increasing Young's modulus, decreasing cross-section diameter and decreasing the length of the mooring line. Xu et al. (2021) investigated several mooring configurations for a semi-submersible FOWT deployed at 50 m water depth. Results indicate that a pure-chain mooring solution will lead to increase mooring line weight and higher tension spikes while a pure-fibre mooring solution has a linear tension increment even at large offsets.

Continued research is needed to understand the cost-benefit relationships of different mooring solutions for floating renewable energy systems deployed in intermediate waters. In the present study, the response characteristics of a taut-moored semi-submersible torus flap combination (STFC) deployed at an intermediate water depth of 50 m are investigated. First, a baseline taut mooring system is developed by adjusting the original wire rope catenary mooring system of STFC for a water depth of 50 m. Next, two alternative taut mooring configurations are developed by modifying mooring parameters such as anchor radius and mooring line properties while maintaining the mooring restoring stiffnesses. Comparing the alternative configurations to the baseline helps analyse the effects of the modified parameters on the dynamic response characteristics of STFC.

6.2 Mooring system design for intermediate water

Mooring system design is an iterative process which strives to limit displacement (primarily translational) of floating structures while maintaining reasonable mooring line tensions. When displaced from the neutral position, a force is created to restore the platform to its neutral position. The mooring system restoring force F and the platform translation is related by mooring restoring stiffness k which consists of geometric stiffness k_G and elastic stiffness k_E.

$$F = k \cdot x \tag{6.1}$$

Geometric stiffness is contributed mainly by the suspended mooring line weight while elastic stiffness is a result of the axial elongation of the mooring line. For chain catenary mooring system, geometric stiffness dominates as the heavy chains contribute to the line pre-tension that restrict the motion of the moored structure. Faltinsen (1993) showed that, assuming inelastic chain, the analytical expression of the horizontal restoring stiffness for a catenary mooring line can be expressed given by,

$$k_G = w\left[\frac{-2}{\left(1+2\frac{T_H}{wh}\right)^{\frac{1}{2}}}+\cosh^{-1}\left(1+\frac{wh}{T_H}\right)\right]^{-1} \tag{6.2}$$

where w is the unit weight of mooring line, T_H is the horizontal mooring line tension and h is the water depth. This presents a challenge. With the same horizontal tension, as water depth decreases, the restoring stiffness increases. An increase in stiffness increases the natural frequencies of translational motions, shifting the resonance closer to wave frequencies. In order to achieve sufficient horizontal pre-tension for catenary mooring in intermediate water depth with a reduced line length, heavy chains have to be used. Another method for achieving the required horizontal pre-tension is by extending the catenary touch-down point. This directly causes an increase in rate of change in catenary shape which leads to a higher risk of chain lift-off. As soon as the full length of chain is lifted-off, the geometric stiffness will transition to elastic stiffness and result in a spike in tension. Therefore, it is common for chain mooring in intermediate water to have exceptionally long anchor radius.

For taut mooring systems, synthetic fibre ropes are used instead of chains. As opposed to a catenary mooring system, the restoring stiffness of a taut mooring system is contributed mainly by the elastic stiffness. For a synthetic fibre mooring line of length l, its contribution to the elastic stiffness is given by,

$$k_E = \frac{EA\cos\theta}{l} \tag{6.3}$$

where E is Young's modulus, A is the cross-sectional area and θ is the angle between the mooring line and the horizontal plane. As shown in Figure 6.1, with the same anchor radius, the mooring line length has to be reduced to maintain the pre-tension as water depth reduces. Additionally, the anchor radius has to be reduced to lower the risk of touching down and dragging of fibre ropes on the seabed. It is easy to see from Equation (6.3) that if the same fibre rope is used, k_E increases as line length reduces. This will increase the mooring line tension and subsequently the natural frequency of the system in the translational degrees of freedom (DOF).

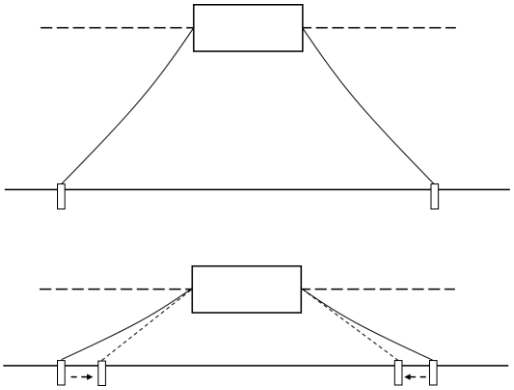

Figure 6.1: Taut mooring configuration for deep and shallow waters

6.3 Description of the concept

6.3.1 Semi-submersible Torus Flap Combination

Figure 6.2 shows the STFC concept proposed by Lee et al. (2022), which combines a floating horizontal axis wind turbine (FHAWT), three flap type WECs and a torus WEC. The supporting platform is a 5 MW CSC braceless semi-submersible hull, designed by Luan et al. (2016) to support a 5 MW NREL reference wind turbine (Jonkman et al, 2009). The platform has a central column that carries the wind turbine and is connected to three side columns via pontoons. Station keeping is achieved through three catenary wire rope mooring lines attached to the side columns.

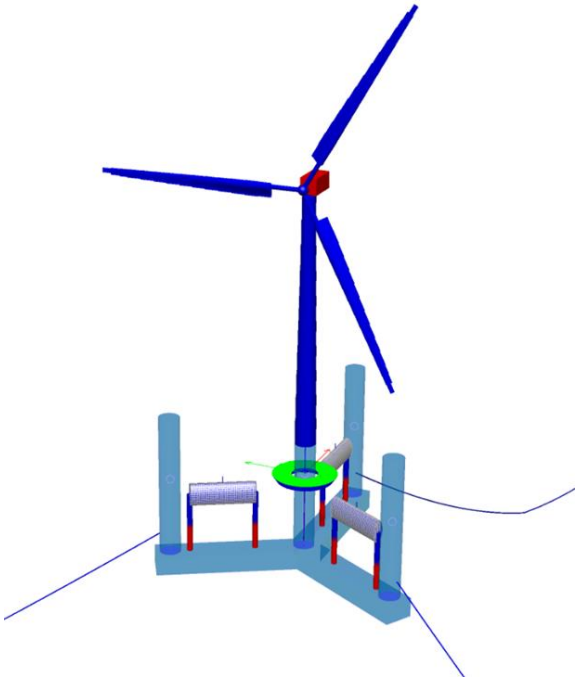

Figure 6.2: Visualisation of the STFC concept

The three flap type WECs are installed on the upper surface of the pontoons, each comprising an elliptic-cylindrical buoy connected by two supporting arms. The mechanism of the flap type WEC is illustrated in Figure 6.3. Hinge connections enable the flap to rotate around the axis parallel to the longitudinal axis of the pontoon. The wave-induced oscillating motion of the buoy about the hinge axes is converted into kinetic energy via shafts connected to the power take-off (PTO) systems.

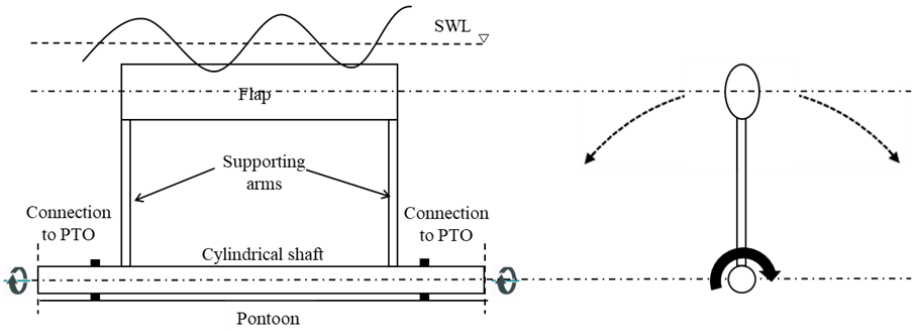

Figure 6.3: Mechanism of the flap type WEC (Lee et al., 2022)

The torus WEC, is a donut-shaped buoy installed through the central column of the hull and is designed to extract wave energy through the relative heave motion between the buoy and the hull. Mechanical end stoppers limit the relative heave motion during extreme environmental conditions. The mechanism of the PTO system of the torus WEC is illustrated in Figure 6.4. The PTO system connecting the torus and the hull consists of hydraulic cylinders, a hydraulic motor, accumulators, and a generator, which generate electricity from the heaving motion of the torus induced by the ocean waves. The properties of STFC are summarised in Table 6.1.

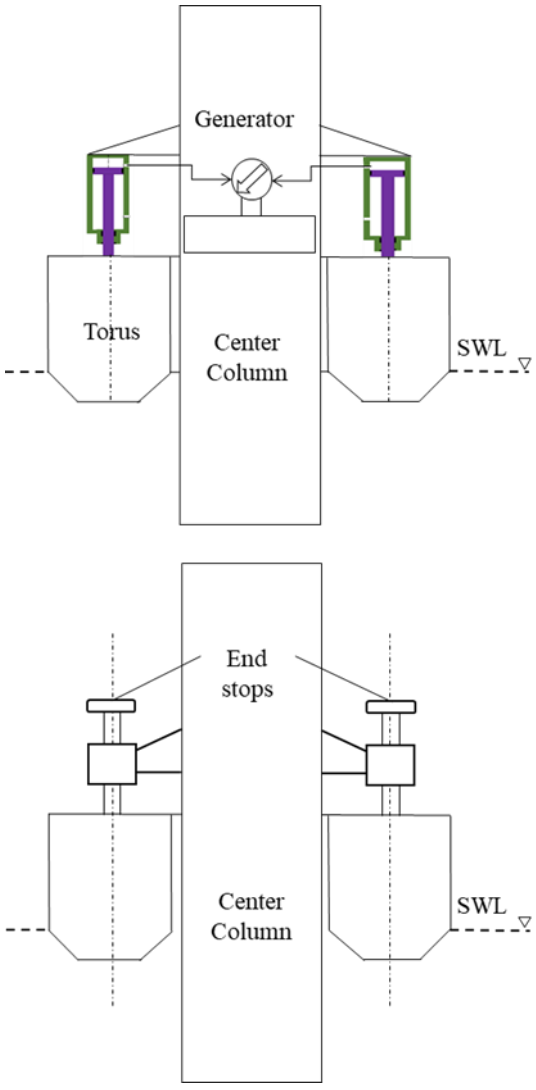

Figure 6.4: Mechanism of the torus WEC (Lee et al., 2022)

Table 6.1: Properties of the STFC concept

Property	Value
CSC semi-submersible	
Draft [m]	30
Displacement [tonnes]	10500
Operational water depth [m]	200
Single mooring line	
Mass per unit length [kg/m]	115
Unstretched mooring line length [m]	1073
Clump weight in water [kg]	15000
Distance of clump weight from fairlead [m]	240
Flap type WEC	
Dimension of elliptic cylinder (length [m] x width [m] x height [m])	20 x 7 x 3.5
Displacement [tonnes]	394
Mass [tonnes]	100
Length of one supporting arm [m]	18.5
Mass of one supporting arm [tonnes]	33.08
Displacement of one supporting arm [tonnes]	33.5
Torus WEC	
Outer diameter of torus [m]	20
Inner diameter of torus [m]	8
Draft [m]	2
Displacement [tonnes]	423.7

6.3.2 Taut mooring system designs

A design flowchart for the taut mooring systems used in the present study is shown in Figure 6.5. First, a baseline mooring system is developed by changing the original mooring system of STFC to a taut mooring system at 50 m water depth while maintaining a similar horizontal mooring line pre-tension. The taut mooring configuration consists of three polyester mooring lines and suction anchors. Due to the low water depth as compared to the anchor radius, Equation (6.3) can be simplified as

$$k_E \approx \frac{EA}{l} \tag{6.4}$$

and the natural period in surge can be estimated by,

$$T_n = 2\pi\sqrt{\frac{M + A_{11}}{k_E}} = 2\pi\sqrt{\frac{(M + A_{11})l}{EA}} \tag{6.5}$$

where M is the mass of the floating platform and A_{11} is the platform's added mass in surge. Equation (6.5) shows T_n will increase with increasing l and anchor radius assuming the same mooring line pre-tension and line stiffness (EA). In the present study, l for the baseline mooring configuration is chosen to be 1000 m such that the value of T_n ($\approx 48\ s$) is not close to the range of first-order wave excitation. Next, two alternative taut mooring configurations are developed by reducing the mooring footprint. The anchor radii for the two alternative taut mooring configurations are reduced to 80% and 60% of the baseline anchor radius, respectively. In order to maintain the same T_n across all taut configurations, the EA and l for the two alternative taut mooring configurations are reduced proportionally. EA ($\propto \text{diameter}^2$) is reduced through the reduction of line diameter. At the same time, it is also assumed that as the line cross-sectional area reduces, the minimum breaking strength (MBS), and unit mass of the synthetic mooring rope will reduce by the same factor. This proves to be a reasonable scaling method according to the line properties listed in the Bridon catalogue for synthetic permanent mooring ropes (Bridon, 2013). Figure 6.6 shows a comparison between all mooring configurations discussed in the present study. The properties for all mooring lines used are summarised in Table 6.2.

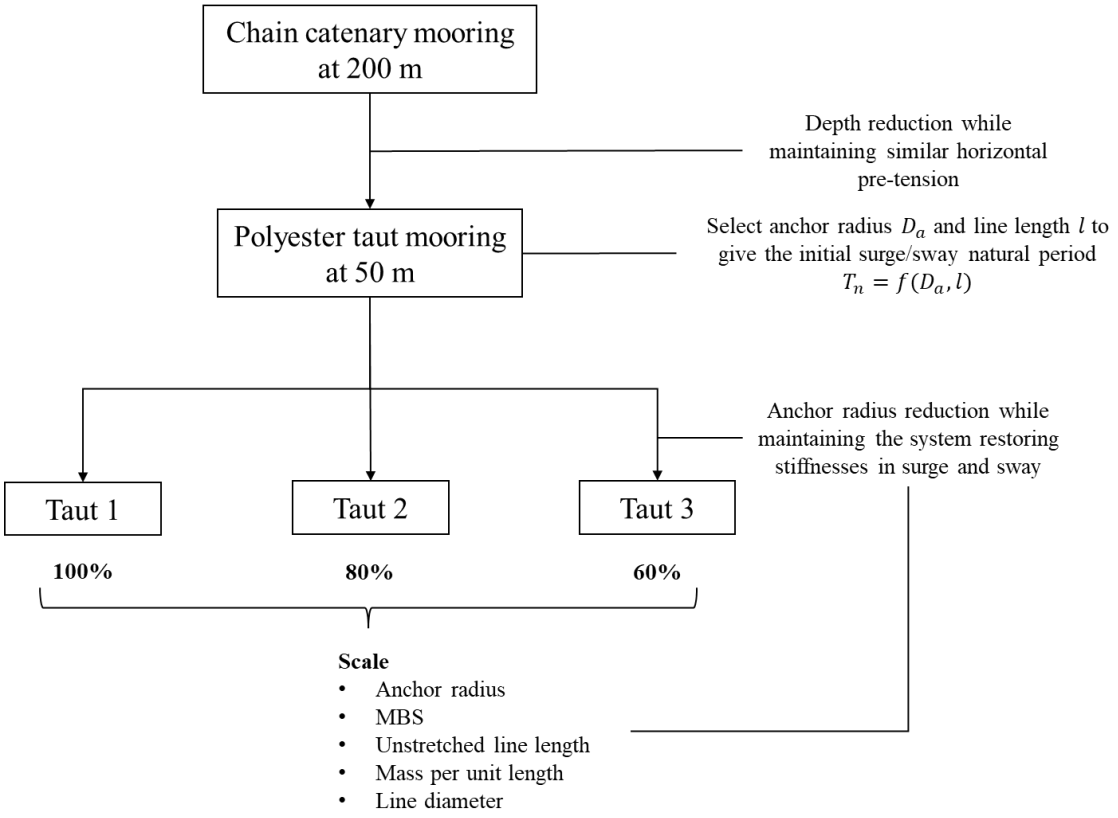

Figure 6.5: Design flow-chart for the design of taut mooring systems

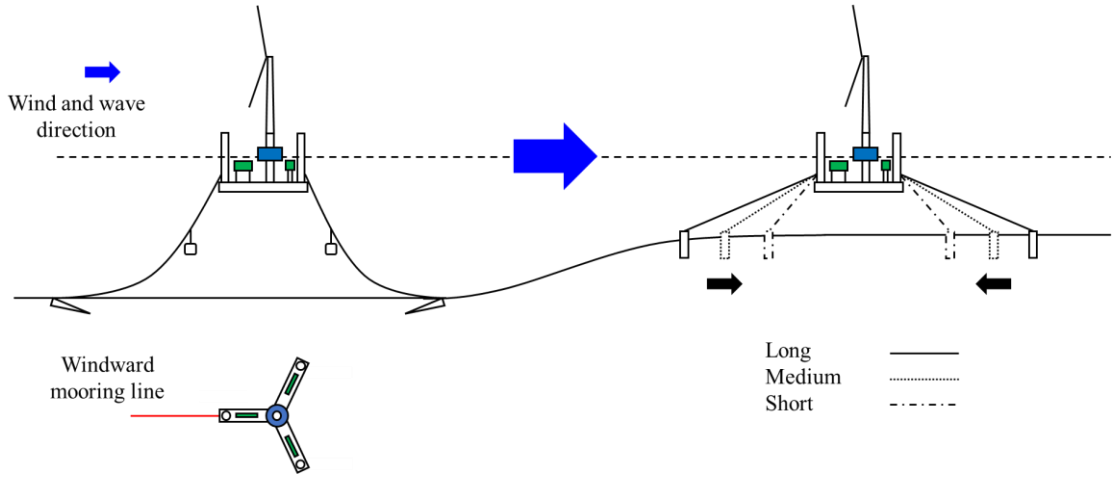

Figure 6.6: Comparison between the catenary mooring system in 200 m water depth and the taut mooring systems in 50 m water depth

Table 6.2: Mooring system properties

Configuration (-)	Anchor radius (m)	MBS (kN)	Unit mass (kg/m)	Unstretched length (m)	Horizontal pre-tension (kN)
Taut 1 (long)	1054	11772	26.5	1000	1500
Taut 2 (medium)	843	9417.6	21.2	791.5	1130
Taut 3 (short)	633	7063.2	15.9	583.4	761

6.4 Numerical model

The numerical models of STFC and different mooring systems are established using SIMA (SINTEF Ocean, 2021a; SINTEF Ocean, 2021b), a dynamic simulation software developed by SINTEF Ocean.

6.4.1 Semi-submersible Torus Flap Combination

The semi-submersible hull, flaps, and torus are modelled as rigid bodies. Frequency-domain hydrodynamic analysis is carried out using HydroD (DNV, 2016) to compute the first-order wave load transfer functions, mean drift load transfer functions and hydrodynamic coefficients considering the effect of hydrodynamic couplings between the rigid bodies. For the semi-submersible hull, slowly varying drift loads are considered through the implementation of full quadratic transfer function (QTF). Viscous loads on wetted bodies are taken into consideration in the form of Morison drag force.

The wind turbine blades, tower, generator shaft, supporting arms for the flap type WECs and mooring lines are modelled as distributed mass flexible elements. The turbine blades are modelled as beam elements with cross sections that have two symmetric planes, capturing blade characteristics in the flapwise and edgewise directions. The tower, generator shaft and supporting arms for the flap type WECs are modelled as beam elements with axisymmetric cross sections. The mooring lines are modelled as bar elements with axial stiffness. For submerged slender elements (WEC supporting arms, mooring lines), the wave loads are calculated using the Morison equation (Morison et al., 1950).

The generator shaft consists of a non-rotating and a rotating part separated by a flexible joint. The generator torque is applied at the flexible joint for speed regulation in accordance with the control strategy described by Jonkman et al. (2009). The PTO damping for the flap type WECs is modelled as linear rotational dampers at the hinge joints. The PTO damping for the torus WEC is modelled as linear spring-dashpot in the direction of relative heave motion between the hull and the torus. As shown in Figure 4, the upper and lower limits, i.e., end stops are fixed to the central column. The schematic representations of the numerical modelling of WECs are shown in Figure 6.7.

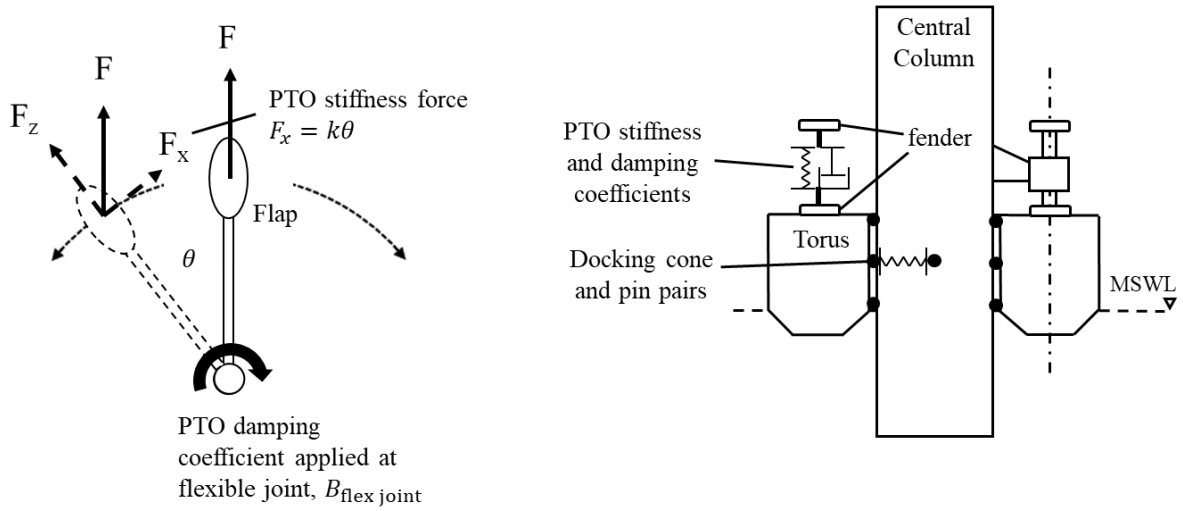

Figure 6.7: Numerical modelling of flap type and torus WECs

Coupled numerical analysis of STFC is carried out in SIMA solving the structural dynamic equilibrium in the time domain (SINTEF Ocean, 2021b),

$$\boldsymbol{R}^I(\boldsymbol{r},\ddot{\boldsymbol{r}},t) + \boldsymbol{R}^D(\boldsymbol{r},\dot{\boldsymbol{r}},t) + \boldsymbol{R}^S(\boldsymbol{r},t) = \boldsymbol{R}^E(\boldsymbol{r},\dot{\boldsymbol{r}},t) \tag{6.6}$$

where t is time, $\boldsymbol{R}^I$ is the inertia force vector, $\boldsymbol{R}^D$ is the damping force vector, $\boldsymbol{R}^S$ is the internal structural reaction force vector, and $\boldsymbol{R}^E$ is the external force vector. $\boldsymbol{r}$, $\dot{\boldsymbol{r}}$, $\ddot{\boldsymbol{r}}$ are structural displacement, velocity, and acceleration vectors, respectively.

6.4.2 Modelling of synthetic fibre rope

The modelling of synthetic fibre mooring is based on the Syrope model (Falkenberg et al., 2017) developed as a result of a Joint Industrial Program (JIP) led by Det Norske Veritas (DNV). The JIP assumes that a synthetic fibre rope can be represented as the spring-dashpot model proposed by Flory et al. (2007). Figure 6.8 shows the spring-dashpot model of a synthetic fibre rope which consists of an elastic component and a plastic (permanent) component. To prevent permanent stretching during use, it is common practice to pre-tension a synthetic fibre rope to the highest expected tension it will experience throughout its service life. As a result, it can be assumed that there will be no further permanent extension after installation (Rowley and Leite, 2011). As compared to the instantaneous elastic stretch, the visco-elastic stretch is a much slower process introduced in the line segments during the installation process. By the time installation is completed, the visco-elastic stretch, construction stretch, and visco-plastic stretch have all been introduced in the line segments. Hence, a synthetic fibre rope during operation can be ultimately modelled as a spring with tension-dependent stiffnesses.

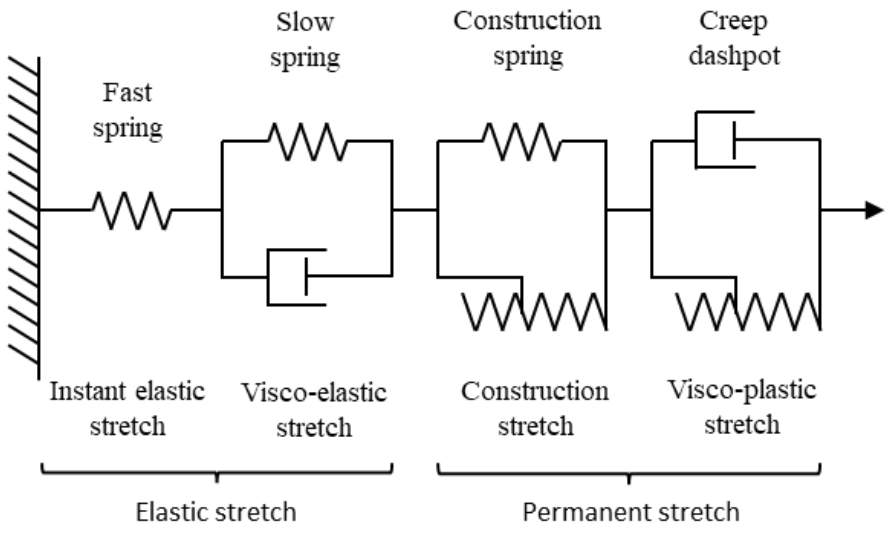

Figure 6.8: Spring-dashpot model of a synthetic fibre rope. Reproduced according to Falkenberg et al. (2017)

The Syrope model of a synthetic fibre rope describes its tension-stretch relationship based on extensive laboratory test data. In Figure 6.9, the four curves representing the characteristics of a synthetic fibre rope according to the Syrope model are shown, which include,

- Original curve
- Original working curve
- Working curve
- Dynamic stiffness

The original curve represents the tension-stretch relationship during the initial quick pre-tensioning of a new rope. After the permanent stretch has been introduced, the original working curve describes the tension-stretch relationship of the working points when the rope is at its historically highest mean tension. A working curve represents the tension-stretch relationship of the working points when the rope has mean tension values lower than the highest preceding mean tension. The dynamic stiffness of a rope is proposed to be linearly dependent on the mean tension level.

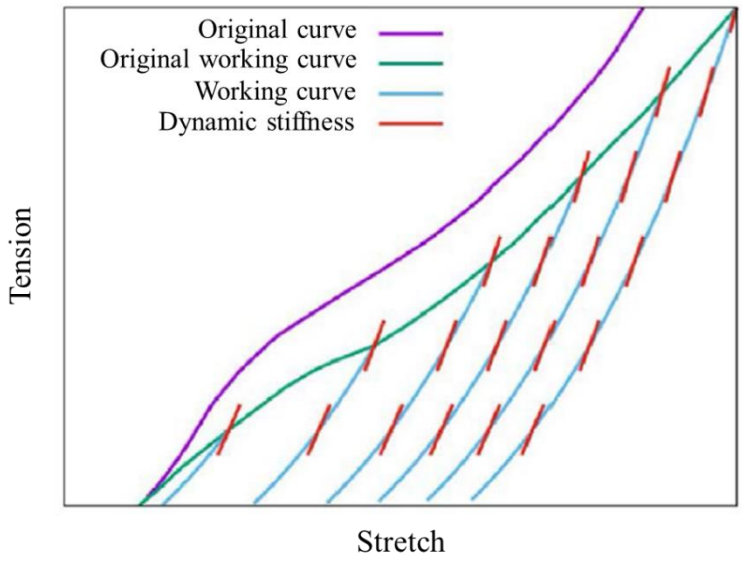

Figure 6.9: The “Syrope” model (Falkenberg et al., 2017)

Depending on the mean environmental load, the historically highest mean tension can be estimated. In practice, once the working curve is confirmed, the slope of the working curve at each working point will be the static stiffness. This implies that the static stiffness is a non-linear function of the mean tension. However, for the purpose of this study, a linearised static stiffness is assumed. The analytical expression of the linearised static stiffness is given by,

$$EA_s = \frac{dT_{\text{mean}}}{d\varepsilon} = a \cdot T_{\text{mean}} + b \cdot \text{MBS} \tag{6.7}$$

where ε is the stretch of the rope, T_{mean} is the mean tension, MBS is the minimum breaking strength while a and b are constants estimated from testing data. Similarly, the dynamic stiffness can be estimated given by,

$$EA_d = \frac{dT_{\text{dyn}}}{d\varepsilon} = c \cdot T_{mean} + d \cdot \text{MBS} \tag{6.8}$$

where c and d are constants obtained from the dynamic testing of ropes. In the present study, the constants a, b, c and d are according to the values used in the master thesis of Stenlund (2018) and Tomren (2022). Figure 6.10 shows the implementation workflow of a taut mooring system analysis in the present study. It is described in detail as follows:

Step 1: Initialise the mooring system with anchor radius, unstretched line length, mean pre-tension $T_{\text{mean,pre}}$, MBS and stiffness constants a, b, c and d. Calculate the static stiffness EA_s for the first iteration using Equation (6.7).

Step 2: For each environmental condition, static analysis is carried out using the corresponding mean environmental loads to determine the mean tension. The mean tension is used to calculate the updated EA_s value according to Equation (6.7). Repeat Step 2 and update EA_s until the T_{mean} value on each mooring line converges.

Step 3: Using T_{mean} from Step 2, calculate EA_d based on Equation (6.8). As shown in Figure 6.11, the stress-free stretch used in the dynamic analysis, ε_0 can be estimated using EA_d given by,

$$\varepsilon_0 = \varepsilon_m - EA_d/T_{\text{mean}} \tag{6.9}$$

where ε_m is the mean stretch obtained in the static analysis (Step 2). Update the unstretched line length by including ε_0.

Step 4: Perform dynamic analysis using EA_d. As a sanity check, the mean tensions calculated from Step 4 and Step 2 should be equal.

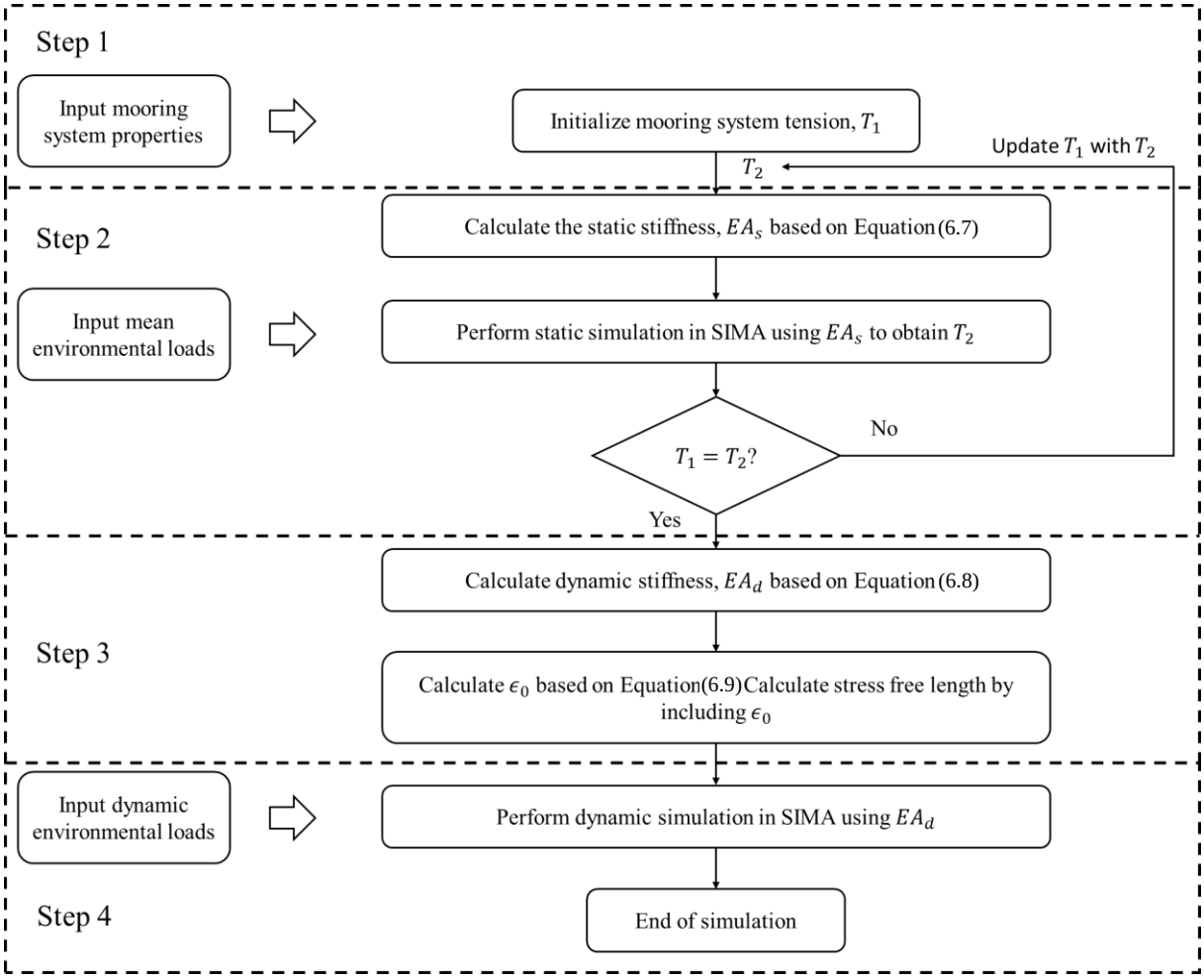

Figure 6.10: Simulation flow-chart for the analysis of a taut mooring system

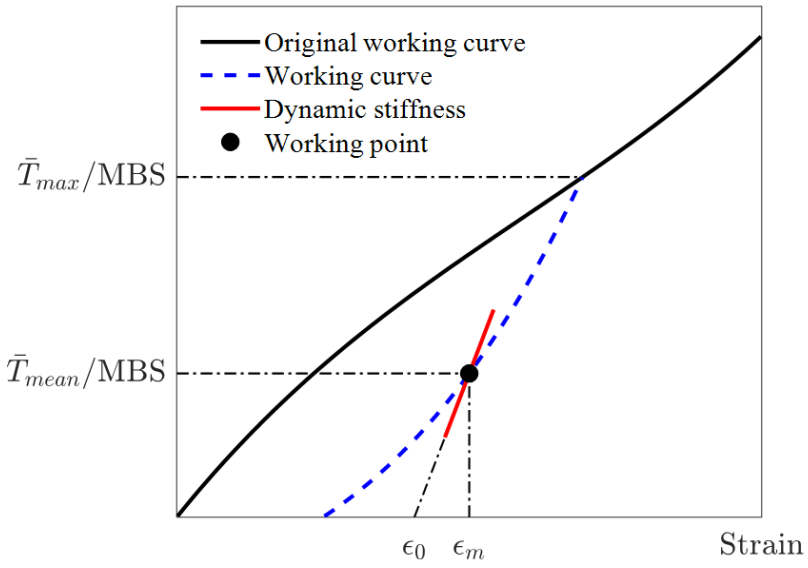

Figure 6.11: Stiffness curve and the linearisation for the calculation of the stress-free length

6.4.3 Environmental conditions

In the present study, the environmental conditions (ECs) for the case study are based on data from an offshore site in the Northern North Sea. The joint distribution of the 1-hour mean wind speed at 10 m elevation, U_{10}, significant wave height, H_s and spectral peak period, T_P at the offshore site are according to the joint probabilistic model proposed by Johannessen et al. (2002). With a selection of six representative wind turbine wind speeds across different operation regions, the corresponding H_s and T_P are selected based on the expected values of their joint distributions. The marginal distribution of U_{10} follows a two-parameter Weibull distribution described by the cumulative distribution function,

$$F(U_{10}) = 1 - \exp\left\{-\left(\frac{U_{10}}{\beta_1}\right)^{\alpha_1}\right\} \tag{6.10}$$

where $\alpha_1 = 1.708$ and $\beta_1 = 8.426$ are the shape and scale parameters. The wind speed at wind turbine hub, U_W can then be calculated using the power law formulation of wind shear,

$$U_W = U(z) = U_{10}\left(\frac{z}{10}\right)^{\alpha} \tag{6.11}$$

where z is the height of the wind turbine hub above mean seawater level (MSWL) which is 90 m and α is the power law exponent which is set to 0.14 in this study according to IEC 61400-3 (IEC, 2009). For turbulent wind conditions, three-dimensional turbulent wind fields with IEC Class C of the Kaimal turbulence model are generated using TurbSim (Jonkman, 2009). The conditional distribution of H_s for a given U_{10} (i.e., $f_{H_s|U_{10}}$) follows a two-parameter Weibull distribution. The expected value of H_s given U_{10} can be calculated using,

$$\mathrm{E}(H_s) = \beta_2 \Gamma\left(\frac{1}{\alpha_2} + 1\right) \tag{6.12}$$

where $\alpha_2 = 2 + 0.135U_{10}$ and $\beta_2 = 1.8 + 0.1U_{10}^{1.322}$ are the shape and scale parameters, respectively. The conditional distribution of T_P for a given set of H_s and U_{10} (i.e., $f_{T_p|U_{10},H_s}$) follows a log-normal distribution. Its expected value can be calculated using,

$$\mathrm{E}(T_p) = (4.883 + 2.68H_s^{0.529})\left[1 - 0.19\left(\frac{U_{10} - (1.764 + 3.426H_s^{0.78})}{1.764 + 3.426H_s^{0.78}}\right)\right] \tag{6.13}$$

The six load cases selected to evaluate the dynamic responses of STFC using different mooring configurations are summarised in Table 6.3.

Table 6.3: Environmental conditions

	U_W [m/s]	T_I [-]	H_S [m]	T_P [s]
EC1	5	0.224	2.10	9.74
EC2	10	0.157	2.88	9.98
EC3	14	0.138	3.62	10.29
EC4	18	0.127	4.44	10.66
EC5	22	0.121	5.32	11.06
EC6	25	0.117	6.02	11.38

6.5 Results and discussion

6.5.1 Mooring pre-tension and restoring stiffness

Sufficient mooring restoring force is required to prevent excessive floater drift under environmental loadings. On the other hand, the restoring stiffness (restoring force/ unit offset distance) has to be designed such that the system natural frequencies in surge, sway and yaw are not close to wave excitation frequencies. In the present study, static simulations are carried out for different mean environmental loads to obtain the corresponding horizontal offsets. In Figure 6.12, the system restoring force for each mooring configuration is plotted against the horizontal offset distance. It can be shown that despite having different anchor radii, the restoring stiffnesses for all taut mooring configurations are close. In Figure 6.13, the tension of the windward mooring line for each mooring configuration is plotted against the horizontal offset distance. As the anchor radius reduces and the mooring line properties being scaled proportionally to maintain the same system restoring stiffness, mooring line pre-tension reduces.

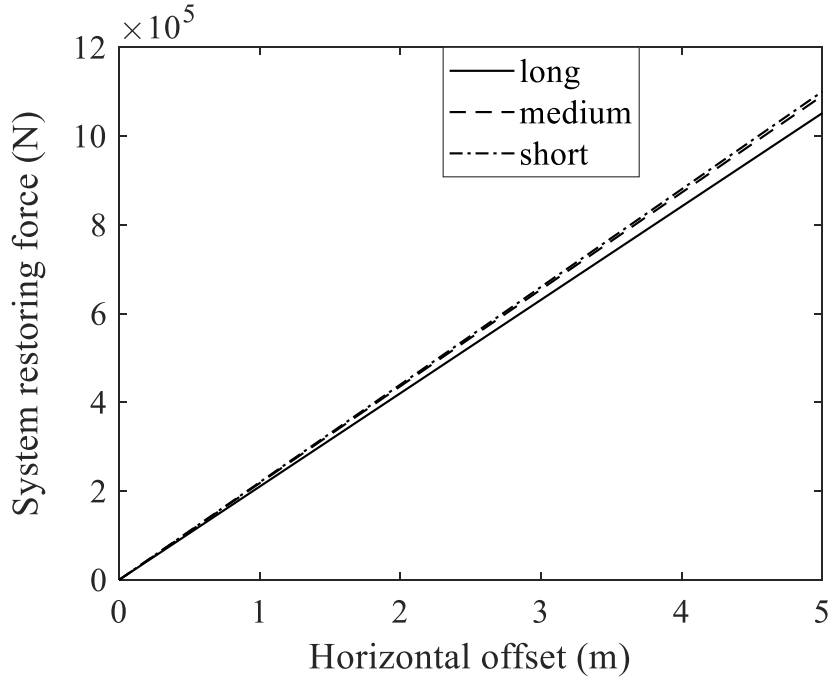

Figure 6.12: System restoring force for the taut mooring configurations

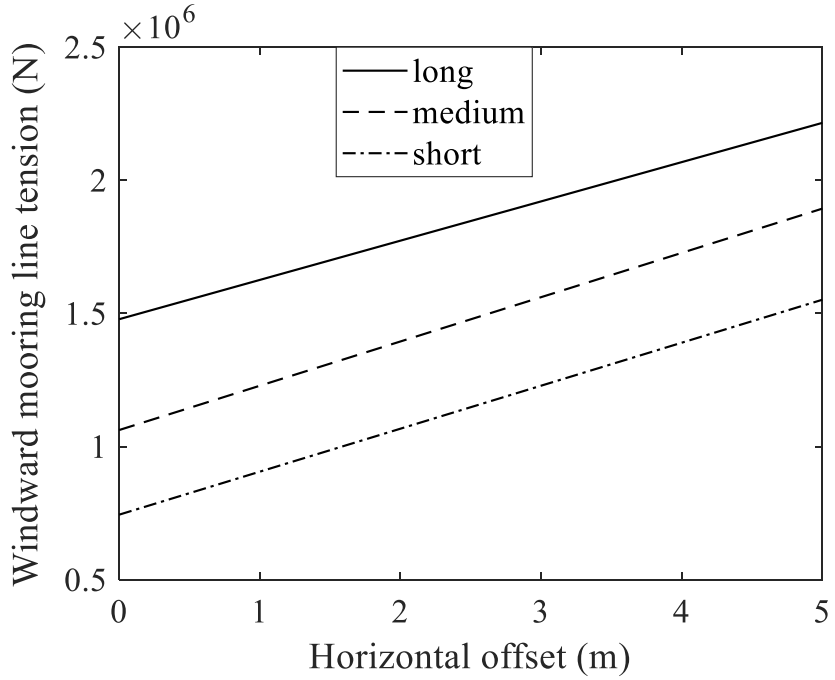

Figure 6.13: Windward mooring tension at fairlead at different offset distance for the taut mooring configurations

6.5.2 Decay test

Decay test simulations are carried out for three different models, and the results are compared against the original STFC model proposed by Lee et al. (2022). During the decay test, the turbine is put in parked condition while all WECs are in operation. Figure 6.14 shows the natural periods for the supporting platform in surge, heave, pitch and yaw DOFs. The natural periods in surge for all taut configurations are shorter than that of the wire catenary configuration. This is mainly caused by the increase in mooring restoring stiffness due to a reduction in water depth. A 50% increase in yaw natural period between the "long" and "short" taut configurations is detected due to the reduction in mooring line pre-tension, as shown in Figure 6.13.

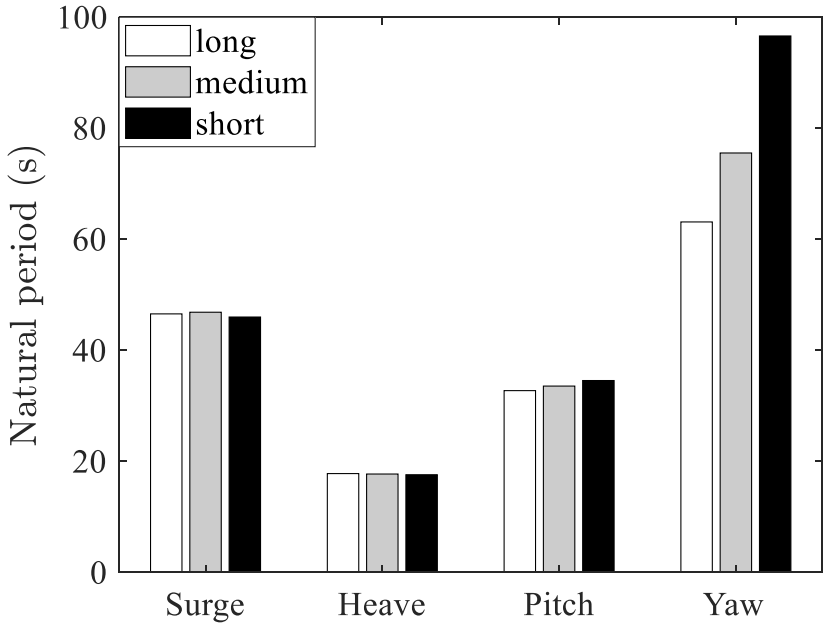

Figure 6.14: Natural period comparison for all mooring configurations

6.5.3 Platform motions

Each simulation is 4600 s in length, with the first 1000 s removed to eliminate transient effects during simulation start-up. To reduce statistical variation, six independent simulations are carried out for each load case. Wind and wave in each environmental load case are assumed to be directionally aligned and are pointing perpendicular to the wind turbine rotor plane. The WECs are assumed to be in operation in all ECs.

The 1-hour average statistics of platform surge, pitch and yaw motions are shown in Figure 6.15, Figure 6.17 and Figure 6.19, respectively. The platform's mean surge, pitch and yaw offsets for all taut mooring configurations are similar due to the same system restoring stiffness. The mean platform surge and pitch offsets increase with wind speed and peak as the wind speed approaches its rated value (11.4 m/s). The maximum mean surge offset is lower than 3 m. In general, the standard deviations for surge, pitch and yaw motions are higher for the short

configuration. This is reflected by the increase in the corresponding resonant responses due to lower mooring line tensions, as shown in Figure 6.16, Figure 6.18 and Figure 6.20. Among the investigated responses, the platform yaw motion response is the most sensitive to the decrease in mooring line pre-tension, with 67 – 90% increase in standard deviations between the "long" and "short" configurations.

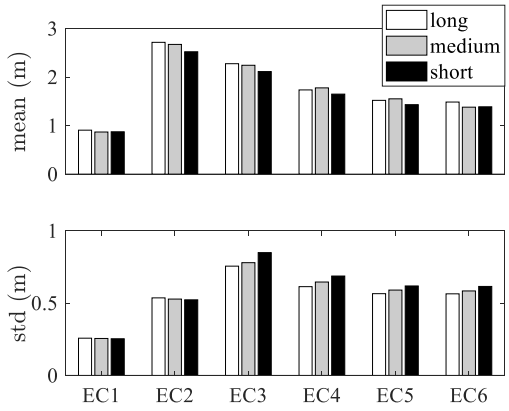

Figure 6.15: Surge motion statistics

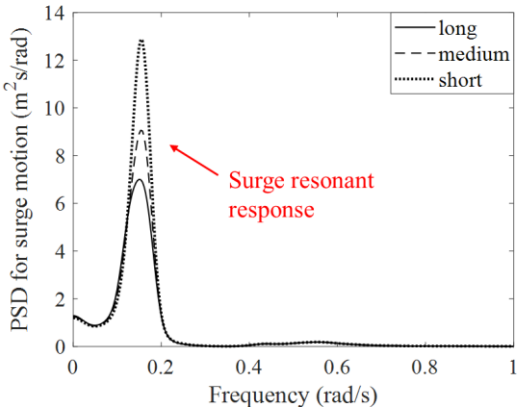

Figure 6.16: Surge spectral

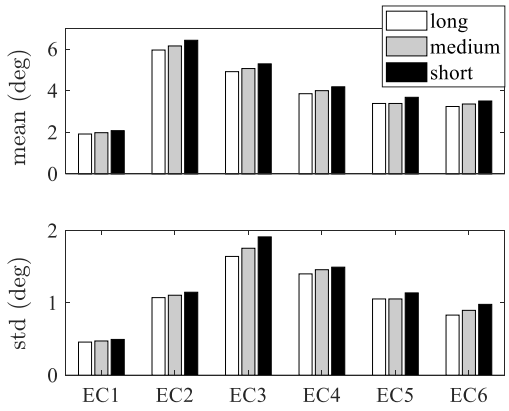

Figure 6.17: Pitch motion statistics

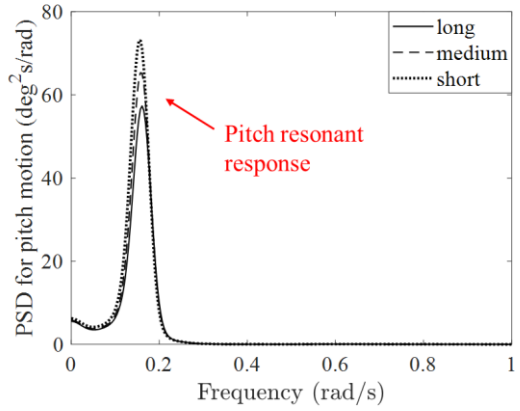

Figure 6.18: Pitch spectral

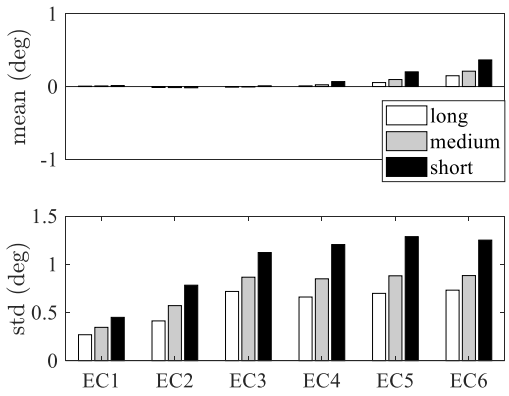

Figure 6.19: Yaw motion statistics

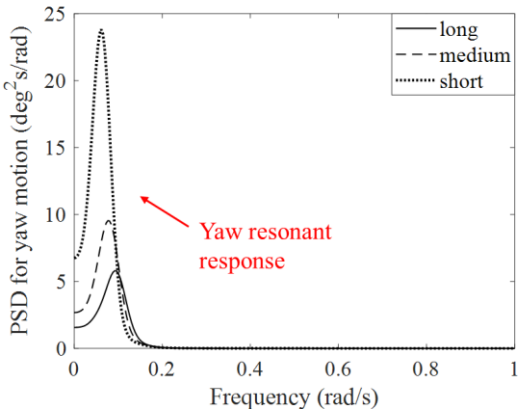

Figure 6.20: Yaw spectral

6.5.4 Mooring line tensions

In order to provide a comparison across different mooring configurations, the mooring line tensions in discussion are represented as mooring line utility factors (MUF) given by,

$$\mathrm{MUF} = \frac{T}{\mathrm{MBS}} \tag{6.14}$$

where T is the instantaneous tensions of the mooring lines.

The 1-hour average statistics of the MUF for the windward mooring line and one of the leeward mooring lines are shown in Figure 6.21. Within operational conditions, the mean MUFs for the windward mooring line are not sensitive to the change in the mooring footprint. The standard deviations of MUF increase with decreasing mooring footprint. This is reflected by the increase in surge resonant response, as shown in Figure 6.22a. For the leeward mooring line, significant reductions in mean MUFs across all ECs can be observed as the anchor radius reduces from "medium" to "short". The standard deviations of MUF for the leeward mooring line increase with decreasing mooring footprint.

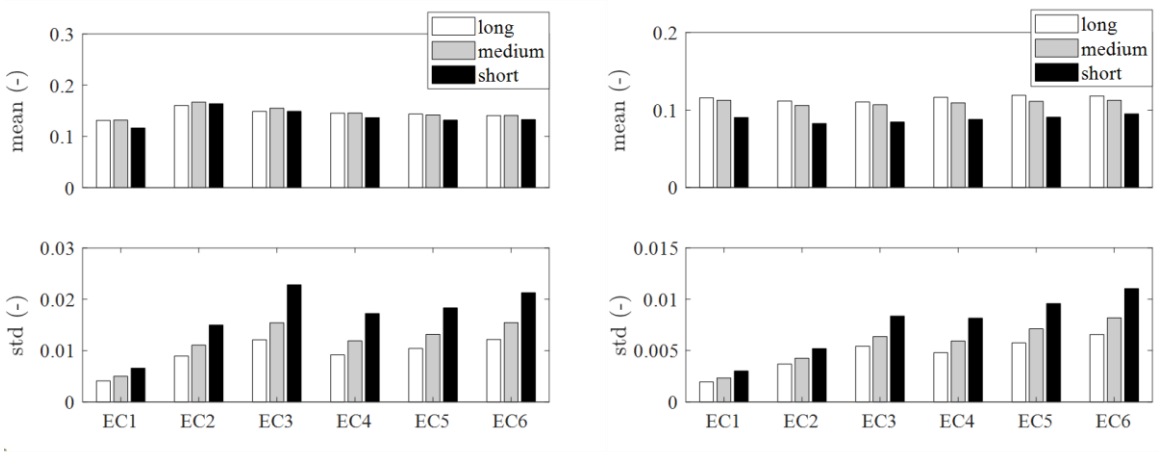

(a) Windward mooring line

(b) Leeward mooring line

Figure 6.21: Mooring line utility factor statistics

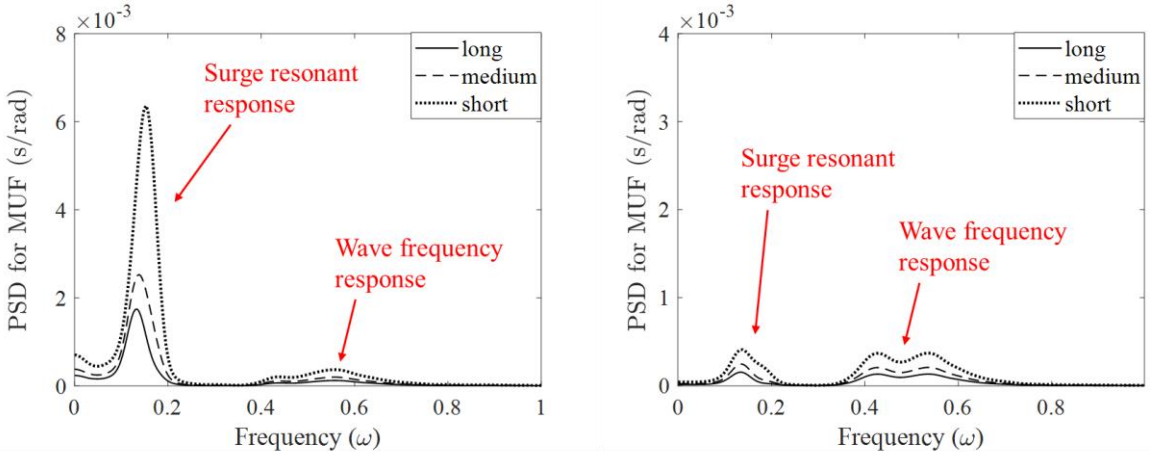

(a) Windward mooring line in EC3
($H_s = 3.62$ m, $T_p = 10.29$ s, $U_w = 14$ m/s)

(b) Leeward mooring line in EC6
($H_s = 3.62$ m, $T_p = 10.29$ s, $U_w = 14$ m/s)

Figure 6.22: PSD for mooring utility factors

In addition to the average statistics, the extreme values of the MUFs are investigated further. The corresponding 1-hour extreme MUF values for the windward mooring line (maximum) and the leeward mooring line (minimum) for each EC are estimated using the global maxima method. The 1-hr extreme value from each of the six time-realizations is extracted. Then, the values are fitted to a Gumbel distribution given by,

$$F_{\mathrm{MUF_{max}(1-hour)}} = \exp\left\{\exp\left[-\frac{(\mathrm{MUF_{max}} - \alpha)}{\beta}\right]\right\} \tag{6.15}$$

where the parameters α and β are the location and scale parameters of a Gumbel distribution, respectively. α and β are obtained through fitting via simple linear regression using six maximum values from each EC. Figure 6.23 shows the comparison of the most probable extreme values across different taut configurations. The values are expressed in terms of the ratio of the most probable extreme values of the "long" configuration. It is observed that a 20% reduction in anchor radius (from "long" to "medium") increases the maximum tension by approximately 10%, and a 40% reduction of anchor radius (from "medium" to "short") increases the maximum tension by approximately 20%. For the leeward mooring line, the minimum tensions are investigated as the risk of slacked line and snapping are of interest. A 20% reduction in anchor radius (from "long" to "medium") decreases the minimum tension by approximately 10%, while a 40% reduction in anchor radius (from "medium" to "short") decreases the minimum tension by approximately 40%. This shows that the minimum tension is reducing at an increasing rate with respect to the decreasing anchor radius, indicating that a minimum anchor radius has been reached while maintaining a constant system restoring stiffness.

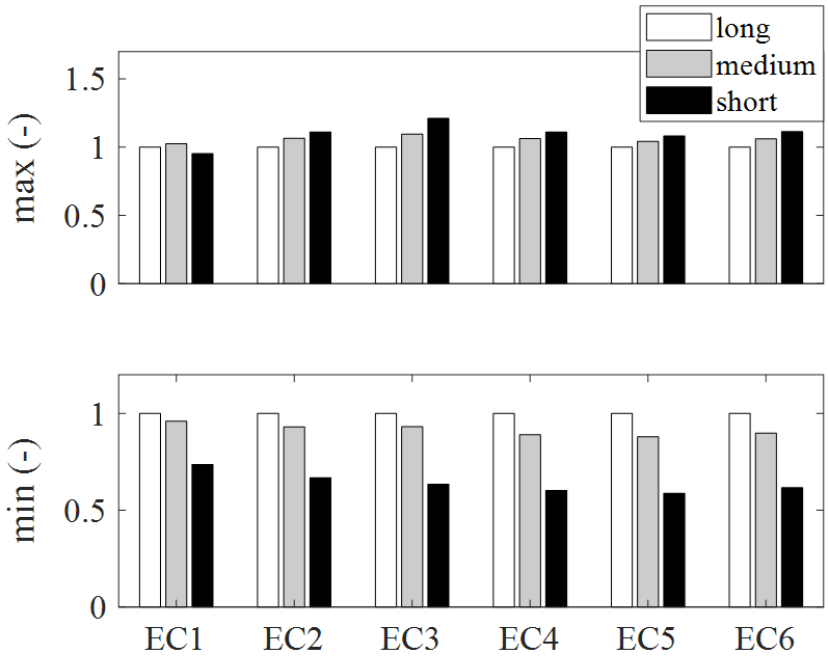

Figure 6.23: Mooring line tension extreme value

6.6 Conclusion

In the present study, taut mooring configurations for a combined wind and wave energy system have been developed, and their performance has been investigated. The design procedures begin with the selection of a baseline design based on a required natural period in surge and sway. Two alternative mooring configurations are then developed by reducing the anchor radius while maintaining similar surge and sway restoring stiffnesses. It is observed that by maintaining similar surge and sway restoring stiffnesses, the mooring line pre-tension reduces with a reducing anchor radius. The reduction in pre-tension reduces the yaw stiffness, which is reflected in a 50 % increase in yaw natural period between the "long" and "short" mooring systems. As compared to the surge and pitch responses, the yaw resonant responses experience a more significant increase across all ECs.

The maximum tension increases as the anchor radius reduces due to an increase in surge resonant response. Despite the reduction in mooring line pre-tension as the anchor radius reduces, slack line event has not been detected. However, the minimum tension is reducing at

an increasing rate with respect to the decreasing anchor radius, indicating that a minimum anchor radius has been reached while maintaining a constant system restoring stiffness.

Acknowledgements

The authors gratefully acknowledge the financial support through the Equinor Akademia program at the University of Stavanger.

References

Benassai, G., Campanile, A., Piscopo, V., & Scamardella, A. (2014). Mooring control of semi-submersible structures for wind turbines. Procedia Engineering, 70, 132-141.

BRIDON. (2013). Oil and Gas – Wire and Fibre Rope Solutions for the World's Most Demanding Applications. Technical Report.

Brommundt, M., Krause, L., Merz, K., & Muskulus, M. (2012). Mooring system optimisation for floating wind turbines using frequency domain analysis. Energy Procedia, 24, 289-296.

Czech, B., & Bauer, P. (2012). Wave energy converter concepts: design challenges and classification. Industrial Electronics Magazine, IEEE, 6, 4-6.

DNV. (2016). HydroD User Manual.

Falkenberg, E., Åhjem, V., & Yang, L. (2017). Best practice for analysis of Polyester rope mooring systems. Offshore Technology Conference, Houston, Texas, USA.

Faltinsen, O. M. (1993). Sea Loads on Ships and Offshore Structures. Cambridge University Press.

Flory, J. F., Åhjem, V., & Banfield, S. J. (2007). A new method of testing for change-in-length properties of large fiber-rope deepwater mooring lines. In Proceedings of the Offshore Technology Conference, Houston, Texas, U.S.A..

Gao, Z., Moan, T., Wan, Ling., & Michailides, C. (2016). Comparative numerical and experimental study of two combined wind and wave energy concepts. Journal of Ocean Engineering and Science, 1(1), 36-51.

Gkaraklova, S., Chotzoglou, P., & Loukogeorgaki, E. (2020). Frequency-based performance analysis of an array of wave energy converters around a hybrid wind–wave monopile support structure. Journal of Marine Science and Engineering, 9(1), 2.

GWEC. (2021). World installs 6.1GW of Offshore Wind in 2020, led by China. https://gwec.net/world-installs-6-1gw-of-offshore-wind-in-2020-led-by-china/

IEC. (2009). International standard 61400-3, Wind turbines, part 3: Design requirements for offshore wind turbines. International Electrotechnical Commission, Geneva, Switzerland.

Johannessen, K., Meling, T. S., & Haver, S. (2002). Joint distribution for wind and waves in the northern North Sea. International Journal of Offshore and Polar Engineering, 12(2).

Jonkman, J., Butterfield, S., Musial, W., & Scott, G. (2009). Definition of a 5-MW Reference Wind Turbine for Offshore System Development (NREL/TP-500-38060). NREL.

Lee, C. F., Tryfonidis, C., & Ong, M. C. (2022). Power performance and response analysis of a semi-submersible wind turbine combined with flap-type and torus wave energy converters. Journal of Offshore Mechanics and Arctic Engineering, 145(4), 042001.

Luan, C., Gao, Z., & Moan, T. (2016). Design and analysis of a braceless steel 5-MW semi-submersible wind turbine. In Proceedings of the ASME 35th International Conference on Ocean, Offshore and Arctic Engineering, Busan, South Korea.

Luan, C., Michailides, C., Gao, Z., & Moan, T. (2014). Effect of flap-type wave energy converters on the response of a semi-submersible wind turbine in operational conditions. In Proceedings of the ASME 33rd International Conference on Ocean, Offshore and Arctic Engineering, San Francisco, California, USA.

McCormick, M. (1981). Ocean Wave Energy Conversion. Wiley, New York.

Michailides, C., Gao, Z., & Moan, T. (2016). Experimental and numerical study of the response of the offshore combined wind/wave energy concept SFC in extreme environmental conditions. Marine Structures, 50, 35-54.

Michailides, C., Luan, C., Gao, Z., & Moan, T. (2014). Effect of flap-type wave energy converters on the response of a semi-submersible wind turbine in operational conditions. In Proceedings of the ASME 33rd International Conference on Ocean, Offshore and Arctic Engineering, San Francisco, California, USA.

Morison, J. R., Johnson, J. W., & Schaaf, S. A. (1950). The force exerted by surface waves on piles. Journal of Petroleum Technology, 2(5), 149-154.

Muliawan, M. J., Karimirad, M., & Moan, T. (2013a). Dynamic response and power performance of a combined Spar-type floating wind turbine and coaxial floating wave energy converter. Renewable Energy, 50, 47-57.

Muliawan, M. J., Karimirad, M., Moan, T., & Gao, Z. (2012). STC (Spar-Torus Combination): a combined spar-type floating wind turbine and large point absorber floating wave energy converter – promising and challenging. In Proceedings of the ASME 31st International Conference on Ocean, Offshore and Arctic Engineering, Rio de Janeiro, Brazil.

Muliawan, M. J., Karimirad, M., Gao, Z., & Moan, T. (2013b). Extreme responses of a combined Spar-type floating wind turbine and floating wave energy converter (STC) system with survival modes. Ocean Engineering, 65, 71-82.

O'Sullivan, K. P. (2014). Feasibility of Combined Wind-wave Energy Platforms (Ph.D. thesis). National University of Ireland. https://cora.ucc.ie/bitstream/handle/10468/1897/OSullivanK_PhD2014.pdf?sequence=2

Qiao, D., Yan, J., Liang, H., Ning, D., Li, B., & Ou, J. (2020). Analysis on snap load characteristics of mooring line in slack-taut process. Ocean Engineering, 196, 106807.

Ren, N., Ma, Z., Fan, T., Zhai, G., & Ou, J. (2018). Experimental and numerical study of hydrodynamic responses of a new combined monopile wind turbine and a heave-type wave energy converter under typical operational conditions. Ocean Engineering, 159, 1-8.

Rowley, D. S., & Leite, S. (2011). What if scenario testing of synthetic fibre rope for deepwater mooring systems. In Proceedings of the Offshore Technology Conference, Rio de Janeiro, Brazil.

SINTEF Ocean. (2021a). SIMO 4.20.3 User Guide.

SINTEF Ocean. (2021b). RIFLEX 4.20.3 User Guide.

Sojo, M., & Auer, G. (2014). Deliverable D1.12 Final Summary Report, Marine Renewable Integrated Application (MARINA) Platform.

Stenlund, T. (2018). Mooring system design for a large floating wind turbine in shallow water (Master's thesis). Norwegian University of Science and Technology (NTNU).

Tomren, M. (2022). Design and Numerical Analysis of Mooring Systems for Floating Wind Turbines – Comparison of Concepts for European Waters (Master's thesis). Norwegian University of Science and Technology (NTNU).

Xu, K., Larsen, K., Shao, Y., Zhang, M., Gao, Z., & Moan, T. (2021). Design and comparative analysis of alternative mooring systems for floating wind turbines in shallow water with emphasis on ultimate limit state design. Ocean Engineering, 219, 108377.

Chapter 7 - Thesis conclusion

In these studies, the mooring systems of STFC are modelled using coupled SIMO-RIFLEX software in SIMA at a water depth of 50 m. Operational conditions of STFC are simulated using fully coupled time domain simulations. The first study focuses on a hybrid mooring system evaluated at two different pre-tensions. The evaluated hybrid mooring system consists of chains, polyester ropes, a buoy and DEA. As a comparison, a taut and catenary system is evaluated in the same conditions. The second study focuses on a taut mooring system that proportionally scales the mooring line length, stiffness, anchor radius, and cross-sectional area. The taut system is evaluated at 100%, 80% and 60% scaling. The main conclusions which can be drawn from the studies performed are:

- A model of STFC with polyester ropes as mooring lines was successfully implemented and analysed using fully coupled time simulations at intermediate water depths
- Polyester can be used as mooring material for STFC in intermediate water and is shown to reduce non-linear tension responses
- The mooring system is still considered stiff when compared to STFC at 200 m water depth. This is seen in the short surge and sway natural periods for all mooring systems at 50 m water depth
- Hybrid mooring systems using a combination of chains, buoys, and polyester rope show a significant cost reduction compared to both catenary and taut mooring systems. The cost reduction is two-fold, one is due to the low cost of polyester, second is due anchor cost using DEA over SA

Recommendations for future work are based on learnings from the studies and can be summarised in the following list:

- The current model of STFC is built using several softwares (GENiE, WADAM, TurbSim, SIMO, RIFLEX). This solution is impractical as making changes is a tedious process. Additionally, with such a large number of softwares, it is difficult to have a complete overview of the model. Therefore, it should be looked into if other modelling softwares can produce the same results

- In the current model, neither marine growth nor current effects are accounted for. Marine growth will increase mooring line weight and effective diameter, which alters tension responses. The current effect is known to increase mean structure offset and hence tensions responses
- The current model is limited to the operational conditions of STFC. Future work should include limit state studies (accidental, fatigue, ultimate). As it stands now, accident and fatigue limit state studies can be performed. However, ultimate limit state studies can not be performed as it would require a control strategy for the torus WEC during extreme weather conditions. The torus WEC should be parked during extreme weather conditions to reduce induced responses
- The Syrope model, implemented in these studies is time-consuming due to its iterative nature. It should be investigated how Syrope can be implemented in SIMA using test data from sub-rope testing. Therefore, it is necessary to acquire such data, either from vendors or by testing
- Hybrid mooring systems show significant room for optimisation. Shorter anchor radius, lighter chains, adding clump weights or using compliant synthetic material such as nylon are options that could be implemented